Adaptive Optics for Free-Space Communication with Entangled Orbital Angular Momentum Photons

Dissertation

zur Erlangung des akademischen Grades
doctor rerum naturalium (Dr. rer. nat.)

vorgelegt dem Rat der Physikalisch-Astronomischen Fakultät
der Friedrich-Schiller-Universität Jena

von Dipl. Phys. Nina Leonhard,
geboren am 05.05.1988 in Frankfurt am Main

Contents

Abstract

With the advent of quantum computers, quantum key distribution is a promising candidate to ensure secure communication also in the future. Its security is based on fundamental quantum mechanical principles and can be verified by measurements. A multitude of experiments have demonstrated its applicability in various scenarios, as e.g. recently between two ground stations which received photons from a satellite. Higher-dimensional state spaces as provided by the orbital angular momentum of photons (OAM) could further improve the security and robustness to noise. Photons with special phase profiles consisting of intertwined helices can carry such an orbital angular momentum. When transmitted through free-space, these photons experience atmospheric turbulence which introduces distortions of the phase carrying the information. To counter-act turbulence distortions,adaptive optics has been developed in astronomy. While its application has been considered in the context of classical OAM communication, this thesis presents the first results of adaptive optics for OAM-based quantum key distribution.

For this thesis, a simulation routine was developed to describe the action of atmospheric turbulence on OAM photons as well as the subsequent correction by an adaptive optics system. The existing theoretical description of atmospheric turbulence on OAM photons was extended to also describe the action of adaptive optics. As the application scenario, the transmission of one photon from an entangled two-qubit state was considered with the adaptive optics system located at the receiver. The main result of this thesis is that the losses of the quantum mechanical properties of OAM photons in atmospheric can be mitigated by adaptive optics. Both the entanglement and the trace of the final state's density matrix can be significantly improved. Furthermore, the security of the quantum key distribution protocol can be ensured for two to three times stronger turbulence as measured by the Fried parameter. Here, the quantum bit error rate and the violation of a Bell inequality were evaluated as figures of merit. The

auxiliary laser beacon that is used to determine the phase distortions introduced by turbulence also has an influence on the compensation of the OAM photons. Because of the different beam geometry of the Gaussian beacon and the OAM photons, the beam waist of the beacon was optimized. The optimum value depends on the OAM of the photons as well as the type of adaptive optics compensation. Furthermore, the figures of merit for quantum key distribution are more sensitive to the beacon beam waist than the quantities associated with classical communication.

The presented results demonstrate the great potential of adaptive optics for OAM communication. By reducing the crosstalk between OAM modes, adaptive optics could allow for new experiments which profit even more from the high dimensionality of OAM photons. The presented theoretical results will thus have a great impact on the future realization of free-space experiments with OAM and adaptive optics.

Chapter 1

Introduction

Over many centuries, people have developed methods to protect their private messages from eavesdroppers. Starting from simple substitution ciphers, these methods have developed into an own mathematical discipline called cryptography. Unfortunately, the only encryption method proven to be unbreakable is a one-time pad which uses a key of the same length as the message for encryption. Clearly, such a method is inconvenient because a new key has to be used for each transmission. Many other encryption protocols are secure simply because breaking them takes too much computation time. With the advent of quantum computers, new algorithms may become available that can perform certain calculations much faster than classical computers. While quantum technologies may thus be used to break current encryption, they may also provide new encryption methods. An example is quantum key distribution which can be used to generate secure keys for data transmission. The clear advantage of this method is that its security is based on fundamental physical principles, in contrast to many classical methods. Impressive quantum key distribution experiments have been performed with polarization-encoded photons in a horizontal link over 143 km [1] and, more recently, for satellite-to-ground transmission [2].

Apart from the two-dimensional states provided by polarization, higher-dimensional state spaces could provide new interesting physics. Furthermore, the security and robustness to noise could be improved by using d-dimensional states, so-called qudits, instead of qubits [3–6]. Alternatively, a higher-dimensional state space could be used to create several parallel channels. Orbital angular momentum of light (OAM) is an example of a high-dimensional system, in principle denumerably infinite, and provides a new degree of freedom to encode (quantum) information. Several experiments have shown
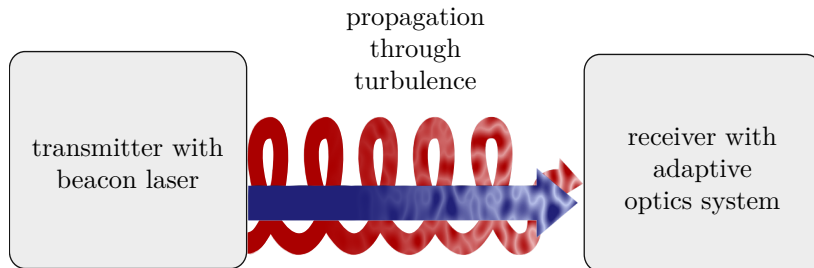
Figure 1.1: Adaptive optics setup to correct for turbulence distortions on OAM-encoded light (red spiral arrow). In order to separate the turbulence distortion from the information encoded in the phase, a so-called beacon with a known phase profile propagates simultaneously through the same atmosphere (blue straight arrow). Based on measurements on the beacon, the adaptive optics system reverts the turbulence distortion of the OAM light.

the applicability of OAM in classical and quantum communication [7–9]. However, its free-space transmission is hindered by atmospheric turbulence which introduces phase distortions. Since OAM results from the complex phase structure of the involved light, atmospheric turbulence introduces crosstalk between OAM states and thus disturbs the communication protocol.

The aim of this thesis is to investigate the ability of adaptive optics to counteract the effect of atmospheric turbulence in an OAM-based quantum key distribution scenario. Adaptive optics is a technology mostly known from astronomy where atmospheric turbulence severely limits the resolution of Earth-based telescopes [10]. Nowadays, all large telescopes above 1 m diameter feature an adaptive optics system. Laboratory experiments have shown that adaptive optics can partially reverse turbulence distortions in *classical* OAM-based communication systems and by that reduce, e.g., the bit error rate [11, 12]. However, free-space experiments with adaptive optics in both classical and quantum communication with OAM, have not been reported, to the best of the author's knowledge. In the context of quantum key distribution, this work is the first to investigate the effect of adaptive optics for OAM-encoded photons.

To this end, a simulation routine was developed to model the propagation through atmospheric turbulence as well as the action of the adaptive optics system. When applying adaptive optics to OAM communication, it is crucial to separate the phase distortion caused by turbulence from the encoded information. An auxiliary laser beam, the so-called beacon, is simultaneously sent along the same path as the signal to measure the turbulence-induced distortions as can be seen in Fig. 1.1. Typically, the beacon has a Gaussian beam profile and, thus, does not carry an orbital angular

momentum. To model the propagation through atmospheric turbulence, a split-step propagation with random phase screens was used. Three different models of adaptive optics were implemented – an idealized phase-correcting system with infinite resolution and a tip-tilt system as well as a realistic system which is based on measurements performed in an existing adaptive optics setup [13]. The formal description of OAM photons in atmospheric turbulence [14, 15] is extended to include the adaptive optics system. Based on that, the efficiency of adaptive optics for OAM-encoded photons was evaluated in terms of the entanglement, quantum bit error rate and violation of Bell inequalities.

The thesis is structured as follows. In Chapter 2, the foundations for OAM-based quantum key distribution are laid. First, the OAM of light is introduced. After some basic concepts of quantum mechanics, the most famous quantum key distribution protocols are explained and it is shown how they can be used with OAM photons. Chapter 3 discusses the main limitation of light propagating through free space – atmospheric turbulence. In particular, the routine used in this thesis to simulate the propagation of OAM light and the Gaussian beacon is presented. Chapter 4 is dedicated to adaptive optics – both the general working principle and the adaptive optics correction models used in this thesis. The results of this thesis are presented in the fifth and sixth chapter. Chapter 5 presents the aforementioned extension of the framework on OAM distortion by turbulence to adaptive-optics correction. Furthermore, the efficiency of adaptive optics correction on OAM-based quantum key distribution is evaluated. In particular, the entanglement of OAM photons, the trace of their density matrix, the quantum bit error rate of the protocol and the violation of a Bell inequality are considered. Chapter 6 extends this proof of principle to a more detailed investigation of the parameters. In particular, the geometry of the beacon is optimized to achieve an even better AO correction. The last chapter 7 presents a conclusion of this thesis and an outlook to future work.

Chapter 2

Orbital angular momentum and quantum key distribution

The goal of this chapter is to introduce the concept of orbital angular momentum of light (OAM) and its applicability in quantum key distribution. To this end, the concept of OAM is derived in Sec. 2.1 from the linear momentum of light and one example of OAM-carrying light beams, the Laguerre-Gauss modes, are discussed. Next, some basic concepts and notations of quantum mechanics are recapitulated in Sec. 2.2. A connection between the OAM degree of freedom and quantum mechanics is made by quantizing the classical OAM modes and by that introducing the concept of an OAM photon. Based on that, quantum cryptography, in particular quantum key distribution, is discussed in Sec. 2.3. Two very popular communication protocols, the Bennet Brassard 1984 (BB84) and Ekert 1991 (E91) scheme and their application in OAM quantum cryptography are presented. Finally, the literature on classical and quantum communication based on OAM-encoding is summarized in Sec. 2.4.

2.1 Orbital angular momentum of light

The angular momentum of light was first investigated in the context of polarization. In accordance with the predictions of Poynting [16], Beth experimentally verified the angular momentum carried by circularly polarized light [17]. To this end, he built an apparatus sensitive enough to measure the torque of a half wave plate which reverses the sense of rotation of a circularly polarized light beam. Specifically, the transformation from left- to right-hand circular polarization implies a change of angular momentum

from $+\hbar$ to $-\hbar$. Because the total angular momentum is conserved, the half wave plate experiences a torque in the opposite direction. The angular momentum resulting from the polarization of light is now called spin angular momentum. Only much later in the 1990s was it realized that, similar to atomic angular momentum, there exists an orbital component to the optical angular momentum which can be any integer multiple of $\hbar$ [18]. To understand how light can carry an orbital angular momentum, a short motivation is given in the following. Please consult Refs. [19–21] for a more detailed and rigorous derivation.

It is known that the *linear* momentum of light is defined by an integral over the linear momentum density defined by the cross product of the electric and magnetic field vector, $\mathbf{E}$ and $\mathbf{B}$, respectively [22]

$$\mathbf{P} = \epsilon_0 \int_V \mathbf{E}(\mathbf{r}, t) \times \mathbf{B}(\mathbf{r}, t) \mathrm{d}^3 r \,. \tag{2.1}$$

In analogy to mechanics, the *angular* momentum is an integral over the angular momentum density given by the cross product of the position vector $\mathbf{r}$ and the linear momentum density:

$$\mathbf{J} = \epsilon_0 \int_V \mathbf{r} \times [\mathbf{E}(\mathbf{r}, t) \times \mathbf{B}(\mathbf{r}, t)] \mathrm{d}^3 r \,. \tag{2.2}$$

One can rewrite this formula by using the definition of the magnetic field in terms of the vector potential, $\mathbf{B} = \boldsymbol{\nabla} \times \mathbf{A}$, and separate it into two terms:

$$\mathbf{J} = \mathbf{S} + \mathbf{L} \,, \tag{2.3}$$

$$\mathbf{S} = \epsilon_0 \int_V \mathbf{E}(\mathbf{r}, t) \times \mathbf{A}(\mathbf{r}, t) \mathrm{d}^3 r \,, \tag{2.4}$$

$$\mathbf{L} = \epsilon_0 \sum_{j=(x,y,z)} \int_V E_j(\mathbf{r}, t)[(\mathbf{r} - \mathbf{r_0}) \times \boldsymbol{\nabla}] A_j(\mathbf{r}, t) \mathrm{d}^3 r \,. \tag{2.5}$$

The first term $\mathbf{S}$ is often referred to as the intrinsic or spin angular momentum since it is independent of the position of the origin. On the contrary, $\mathbf{L}$ depends on the choice of origin and is thus called the *orbital angular momentum*. One can show that circular polarization produces a spin angular momentum of $\pm\hbar$ per photon.

In contrast, the orbital angular momentum depends on the transverse profile of a light beam. For linearly polarized light propagating in z-direction, one can find a simplified expression for the z-component of $\mathbf{L}$ [19, Complement 4B]:

$$L_z = \epsilon_0 \int_V E(\mathbf{r}, t) \tfrac{\partial}{\partial \theta} A(\mathbf{r}, t) \mathrm{d}^3 r \,, \tag{2.6}$$

given in polar coordinates r, θ, and z. Plane waves cannot carry an orbital angular momentum as defined above since the derivative with respect to the azimuthal angle θ vanishes. Hence, beams with a dependence on θ will be studied in the following.

One example are the Laguerre-Gauss modes which are solutions of the paraxial equation of a monochromatic wave in vacuum [23]

$$\nabla_T^2 u + 2ik\frac{\partial u}{\partial z} = 0 \,, \tag{2.7}$$

where ∇_T^2 is the transverse Laplacian in polar coordinates. More details on the propagation of light through vacuum and turbulent media will be given in Ch. 3. In the equation above, the complex exponential terms associated with propagation and the temporal evolution have already been separated from the mode function. The Laguerre-Gauss mode functions satisfy Eq. (2.7) and are given by [23]:

$$u_{p,l}(r, \theta, z) = N_{p,l} \left(\frac{\sqrt{2}r}{w(z)}\right)^{|l|} L_p^{|l|}\left(\frac{2r^2}{w^2(z)}\right) e^{-\frac{r^2}{w(z)^2}} e^{-\frac{ikr^2z}{2(z^2+z_R^2)}} e^{i(2p+|l|+1)\Phi(z)} e^{il\theta} \,. \tag{2.8}$$

Two mode numbers are required to describe their behavior, the radial number p and the azimuthal number l where p can take positive integer values and l can take any integer value. Here, L_p^l denotes the associated Laguerre polynomials. The factor $N_{p,l}$ has been included for normalization. One can see that the mode function consists of a polynomial multiplied by a Gaussian which both depend only on the radius. A complex phase factor adds a spherical phase as the beam propagates along z. The Gouy phase factor $\exp[i(2p+|l|+1)\Phi(z)]$ adds another propagation-induced phase. Of particular interest for this thesis is the complex phase factor $\exp(il\theta)$ which depends on the azimuthal index. The beam waist $w(z)$, Gouy phase $\Phi(z)$ and Rayleigh range z_R have the same definition as in the case of Gaussian beams

$$z_R = \frac{\pi w_0^2}{\lambda} \,, \tag{2.9}$$

$$w(z) = w_0\sqrt{1 + (z/z_R)^2} \,, \tag{2.10}$$

$$\Phi(z) = \arctan(z/z_R) \,, \tag{2.11}$$

where w_0 is the initial beam waist. If the radial and azimuthal indices are set to 0 in Eq. (2.8), one obtains the mode function of a Gaussian beam.

Figure 2.1 visualizes Eq. (2.8) with exemplary intensity and phase profiles in the transverse plane at $z = 0$. Apart from the fundamental Gaussian mode with $p = 0$, $l = 0$, the intensity profiles (upper row of Fig. 2.1) exhibit a ring-like shape. Although
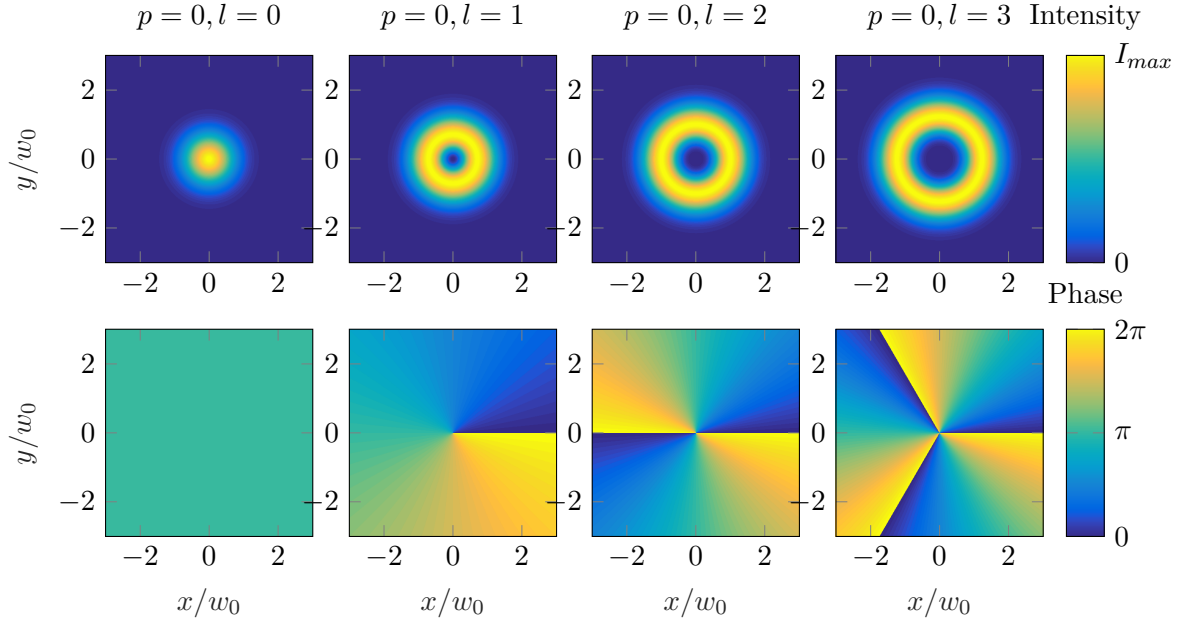
Figure 2.1: Transverse profiles of Laguerre-Gauss modes with different mode indices. (Top row) Intensity profiles show a ring-like maximum. (Bottom row) Phase profiles show l transitions from 0 to 2π
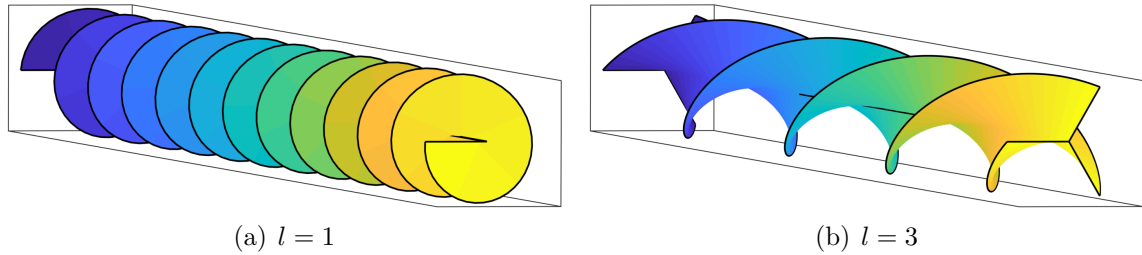
Figure 2.2: Surfaces of equal phase plotted against the propagation direction z. The surfaces consist of l intertwined helices: (a) $l = 1$ and (b) $l = 3$.

not shown in the figure, there can be several concentric rings separated by circles of vanishing intensity for $p > 0$. A very interesting feature of these modes is the phase profile shown in the lower row of Fig. 2.1. It consists of l transitions from 0 to 2π caused by the $\exp(il\theta)$ term in Eq. (2.8). An immediate consequence of this term is the so-called vortex which is a discontinuity of the phase at the origin where the intensity vanishes. The surfaces of constant phase along the propagation direction z, as depicted in Fig. 2.2, consist of l intertwined helices revolving around the optical axis. This rotating structure also makes it quite plausible that these beams carry an angular momentum.

Formally, this can be verified by inserting the mode functions from Eq. (2.8) into the formula for the orbital angular momentum, Eq. (2.6). The derivative of the $\exp(il\theta)$ dependence with respect to θ leads to an orbital angular momentum proportional to the mode number l. A more detailed analysis shows that it has a value of $\hbar l$ per photon [18]. Because l can take any integer value, there are infinitely many possible values of the orbital angular momentum. With this, one finds an interesting distinction from the spin angular momentum of light which can only take two values, namely $+\hbar$ and $-\hbar$.

2.2 Quantum states and entanglement

Before motivating the transition from the classical mode functions given in the previous section to OAM *photons*, some of the basic concepts of quantum mechanics are recapitulated. First, the notation used throughout this thesis is introduced. Next, the entanglement of a bipartite system (e.g. two photons) is discussed as well as methods for quantifying it. Then, the quantization of OAM-carrying light beams is discussed.

To highlight the differences between classical physics and quantum mechanics, let us take a short detour to the Stern-Gerlach experiment. This approach closely follows the first chapter of Ref. [24].

In the Stern-Gerlach experiment, a beam of hot silver atoms is passed through an inhomogeneous magnetic field and detected by a glass plate as illustrated in Fig 2.3. Since silver atoms are electrically neutral and have one electron in their outer electronic shell, one can approximate their magnetic dipole moment by that of a single electron. In this configuration, the force caused by the inhomogeneous field is proportional to the gradient of the magnetic field, here chosen to be in z-direction, multiplied by the z-component of the magnetic dipole moment μ called μ_z

$$F_z = \mu_z \frac{\partial B}{\partial z} \qquad \text{inhomogeneous field in } z\text{-direction} \,. \tag{2.12}$$

Behind the field, glass plates record the arriving silver atoms showing two separated peaks with no atoms arriving at the center. Assuming that μ_z can only take two values $+\mu$ and $-\mu$, the atoms can only be deflected in two directions.

Next, more subsequent inhomogeneous fields are introduced to the setup, but the paths containing atoms with negative magnetic dipole moment are blocked. The second field is oriented in x- and the third in z-direction. Now, one observes an effect that cannot be explained with classical theory. Although the first inhomogeneous field selects
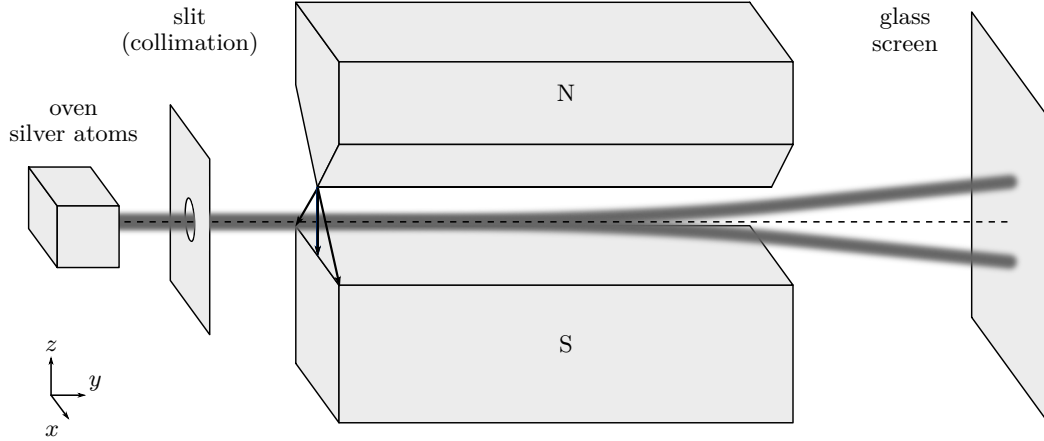
Figure 2.3: Schematic of the Stern-Gerlach experiment. An oven produces silver atoms with random magnet dipole moment in z-direction. The inhomogeneous magnetic field (black arrows) leads to a splitting into two beams (those with positive and those atoms with negative μ_z). A glass plate is used to detect the atoms. Inspired by Ref. [25].

the atoms with positive dipole moment with respect to the z-axis, the final z-direction measurement again shows two peaks for both positive and negative dipole moment. Without the field in x-direction one observes just one peak. Thus, the measurement in x-direction must change also the magnetic dipole moment in z-direction.

To explain this effect, an analogy can be drawn between μ_z and the polarization of (classical) light. The magnetic dipole moment with $+\mu$ and $-\mu$ in z-direction is analogous to vertical and horizontal polarization of light ($0°$ and $90°$ rotations of a linear polarizer). The measurements of $+\mu$ and $-\mu$ in x-direction, however, correspond to $+45°$ or $-45°$ polarization. A linear light polarizer can thus be used to explain the behavior of an inhomogeneous magnetic field with subsequent selection of only one of the two beams. It is known that after a first vertical ($0°$) polarizer, a subsequent horizontal polarizer ($90°$) does not transmit any light. However, after adding a $45°$ polarizer in between the $0°$ and $90°$ polarizers, one observes a non-vanishing intensity after the last polarizer. This analogy shows that, similar to linearly polarized (classical) light, the silver atoms' magnetic dipole moment in z-direction needs to be described by a two-dimensional vector rather than a scalar.

Based on the intuition developed for the Stern-Gerlach experiment, a more formal description of a quantum system is introduced. Similar to the z-component of the magnetic dipole moment of the individual silver atoms, the state of any quantum mechanical system is described by a vector, from now on denoted by $|\alpha\rangle$. The states of

the system are part of a so-called Hilbert space denoted by $\mathcal{H}$ which contains all complex linear combinations of states $|\alpha\rangle$. There exists also a dual space closely connected to the vector space. Its vectors are represented by $\langle\beta|$. The inner product of two vectors is denoted by

$$\langle\beta|\alpha\rangle = (\langle\beta|)(|\alpha\rangle) \in \mathbb{C}\,. \tag{2.13}$$

This quantity is very similar to the scalar product of two vectors in real vector space. However, it is a complex number, meaning that not only its absolute value but also its complex phase is important. As in real vector space, two states are orthogonal if their inner product vanishes and one can define the norm of a state by

$$||\alpha|| = \sqrt{\langle\alpha|\alpha\rangle}\,. \tag{2.14}$$

An observable of the system is represented by a Hermitian operator A, i.e. $A = A^\dagger \equiv (A^*)^T$. As a consequence, the eigenvectors $\{|a\rangle\}$ of the operator A form a basis of $\mathcal{H}$ and the corresponding eigenvalues λ_a are real numbers. A state $|\alpha\rangle$ can be expanded in terms of the eigenvectors of A

$$|\alpha\rangle = \sum_{a'} c_{a'}|a'\rangle\,, \tag{2.15}$$

with the weights $c_{a'} = \langle a'|\alpha\rangle$. When a measurement of the observable A is performed, the state $|\alpha\rangle$ will be transformed into one of the states $|a\rangle$ similar to the projection a linear polarizer performs on classical light. The probability for each of the states is given by

$$P(a) = |\langle a|\alpha\rangle|^2\,, \tag{2.16}$$

when the state $|\alpha\rangle$ is normalized. It should be noted that for a single measurement, one can observe but one of the possible outcomes. The probabilities defined by Eq. (2.16) can be obtained by preparing the same initial state and averaging over repeated measurements of the system.

The vectorial nature of the above description also implies that – for a finite-dimensional Hilbert space – one can express states and operators by vectors and matrices, respectively. In addition, the change of the representation of a state from one orthonormal basis $\{|a\rangle\}$ to another $\{|b\rangle\}$ can be performed by a transformation U which is unitary, i.e. $U^\dagger U = \mathbb{1}$.

In a next step, consider the case of two quantum systems which can be described both by the formalism introduced above. Mathematically, the two individual Hilbert

spaces $\mathcal{H}_{1/2}$ are combined into a composite space by a tensor product leading to new states

$$|\Psi\rangle = |\alpha\rangle_1 \otimes |\beta\rangle_2 \,. \tag{2.17}$$

For the sake of clarity, lower case Greek letters are from now on used for single quantum systems and upper case Greek letters for bipartite systems. Since also superpositions of these states are valid quantum states, there exist states that do not take the product form of Eq. (2.17). Let us consider the example of two two-level quantum systems. They both have a basis $\{|0\rangle, |1\rangle\}$ by which the single system states can be described. Two examples of such states are the one with both systems in the 0 state $|0\rangle_1 \otimes |0\rangle_2$ or both in the 1 state $|1\rangle_1 \otimes |1\rangle_2$. Since these states are part of the composite Hilbert space, so is the following linear combination of these states

$$|\Psi\rangle = \frac{1}{\sqrt{2}} \left(|0\rangle_1 \otimes |0\rangle_2 - |1\rangle_1 \otimes |1\rangle_2 \right) \,, \tag{2.18}$$

$$= \frac{1}{\sqrt{2}} \left(|0,0\rangle - |1,1\rangle \right) \,, \tag{2.19}$$

with the short-hand notation for bipartite states $|\alpha\rangle_1 \otimes |\beta\rangle_2 = |\alpha, \beta\rangle$. Such a state cannot be factorized into a form like Eq. (2.17). As a consequence, the two systems need to be characterized together rather than individually and are called *entangled*. By performing a measurement on one of the systems, one immediately changes the state of the other system. In fact, this peculiar behavior of entangled states can be exploited in quantum key distribution as will be discussed in Sec. 2.3. It should be noted that it is not possible to instantaneously transmit information (and thus faster than the speed of light) without linking the two systems by another communication channel which was one of the main concerns of this theory.

It may actually happen that a physical system is not in a state of the above form of a vector which is called a pure state. In fact, the state of a quantum mechanical system can be distributed statistically, as e.g. the μ_z value of the silver atoms coming from the oven in the Stern-Gerlach experiment where 50% have positive and the remaining 50% have negative magnetic dipole moment. Such a mixture of states needs an extension of the formalism described above. Instead of the vector description for pure states, a mixed state needs to be described by a density matrix [26, p. 127 f.]

$$\rho = \sum_i p_i |\Psi_i\rangle\langle\Psi_i| \,, \tag{2.20}$$

composed of the pure state matrices $|\Psi_i\rangle\langle\Psi_i|$ which appear with the classical probabilities p_i. Hence, the probabilities p_i are positive real numbers and sum up to 1 for a normalized state ρ. Practically, this matrix is obtained by a matrix multiplication of the column vector $|\Psi_i\rangle$ and the row vector $\langle\Psi_i|$. For a mixed state, Eq. (2.20) is always composed of more than one state. A simple check to determine whether a state is pure or mixed is given by the trace of the squared density matrix which returns $\mathrm{tr}(\rho^2) = 1$ for pure states and $\mathrm{tr}(\rho^2) < 1$ for mixed states [26]. Later in this thesis, in Ch. 5, mixed states will result from the averaging over the stochastic atmospheric medium such that a density matrix description is required. Recall that a pure state is called entangled, if it cannot be rewritten as a product state. Similarly, a mixed state is called entangled, if one cannot find a decomposition as in Eq. (2.20) for which all $|\Psi_i\rangle$ are product states.

Now that the concept of entanglement has been introduced, the question arises how to determine that a state is entangled and how to quantify it. The definition above is, in fact, inconvenient in terms of a fast computation. An entire research field is dedicated to finding functions that quantify entanglement, so-called entanglement measures. Such a function should vanish for separable states and increase with increasing entanglement of a state. In this thesis, the calculations are restricted to a two-qubit system which is the simplest physical system that can exhibit entanglement. The general description of entanglement measures in higher-dimensional systems or in multi-partite systems with more than two constituents is much more involved and beyond the scope of this thesis.

For bipartite two-qubit states, a function called concurrence represents an entanglement measure [27]. To calculate it, one needs to define the flipping operator acting on a *single* qubit $|\psi\rangle$ which interchanges the two possible qubit states $|0\rangle$ and $|1\rangle$:

$$|\widetilde{\psi}\rangle = \sigma_y|\psi^*\rangle\,, \tag{2.21}$$

where $|\psi^*\rangle$ is the complex conjugate of $|\psi\rangle$ and σ_y is the second Pauli matrix

$$\sigma_y = \begin{pmatrix} 0 & -i \\ i & 0 \end{pmatrix}. \tag{2.22}$$

A two-qubit state is flipped by applying this operation to both subsystems individually. To determine the entanglement of a pure state, the concurrence can be simply calculated by

$$C(\Psi) = |\langle\Psi|\widetilde{\Psi}\rangle|\,, \tag{2.23}$$

meaning that the concurrence is the overlap between the state and its flipped version. One can easily show that a product state of form

$$|\Psi_{prod}\rangle = |\psi_1\rangle \otimes |\psi_2\rangle \tag{2.24}$$

has vanishing concurrence, since $|\widetilde{\Psi}_{prod}\rangle = |\widetilde{\psi}_1\rangle \otimes |\widetilde{\psi}_2\rangle$ and the single qubit overlap with the initial and flipped state $\langle\psi_{1/2}|\widetilde{\psi}_{1/2}\rangle = 0$, [1]

$$C(\Psi_{prod}) = |\langle\psi_1|\widetilde{\psi}_1\rangle \times \langle\psi_2|\widetilde{\psi}_2\rangle| = 0 \,. \tag{2.25}$$

In contrast, the maximally entangled state

$$|\Psi_{Bell}\rangle = \frac{1}{\sqrt{2}}(|0,1\rangle - |1,0\rangle) \tag{2.26}$$

is equal to its flipped version $|\widetilde{\Psi}_{Bell}\rangle = |\Psi_{Bell}\rangle$ returning a concurrence of 1.

For mixed states, one defines the flip operation to the two-photon density matrix ρ by

$$\widetilde{\rho} = (\sigma_y \otimes \sigma_y)\rho^*(\sigma_y \otimes \sigma_y) \,. \tag{2.27}$$

The concurrence can then be calculated from the eigenvalues λ_i (sorted in descending order) of the matrix

$$\mathcal{R} = \rho\widetilde{\rho} \,, \tag{2.28}$$

according to [27]

$$C(\rho) = \max(0, \sqrt{\lambda_1} - \sqrt{\lambda_2} - \sqrt{\lambda_3} - \sqrt{\lambda_4}) \,. \tag{2.29}$$

Later in this thesis, the concurrence is used to quantify the entanglement of turbulence-distorted states. Since the turbulent medium behaves stochastically, the concurrence depends on each realization of turbulence. To estimate the fluctuations of the concurrence, an error propagation was performed for the non-Hermitian matrix $\mathcal{R}$ which are described in App. B of Ref. [28]. The formula for the error of the concurrence as well as its Matlab implementation were obtained by Giacomo Sorelli at the University of Freiburg.

Until now, the details of the quantum system itself have not been discussed. This thesis is restricted to the study of photons, in particular photons that carry orbital

---

[1]For a general single qubit state defined by $|\psi_1\rangle = a|0\rangle + b|1\rangle$, the flipped version is $|\widetilde{\psi}_1\rangle = -ib^*|0\rangle + ia^*|1\rangle$. The overlap $\langle\psi_1|\widetilde{\psi}_1\rangle = -ia^*b^* + ib^*a^* = 0$ vanishes.

angular momentum. The quantization of the electromagnetic field is treated in many textbooks, e.g. Refs. [19, 20]. Here, the main approach and its results are outlined. A correspondence between classical and quantum physics is made by first finding a set of canonical variables and the Hamiltonian of the classical system. When quantizing the electromagnetic field, this calculation is based on Maxwell's equations which yields canonical variables for each plane wave with wave vector $\mathbf{k}$ and polarization s. According to the correspondence principle, the (classical) canonical variables are replaced by quantum mechanical observables which have to satisfy the commutation relation

$$[\hat{q}_{\mathbf{k},s}, \hat{p}_{\mathbf{k}',s'}] \equiv \hat{q}_{\mathbf{k},s}\hat{p}_{\mathbf{k}',s'} - \hat{p}_{\mathbf{k}',s'}\hat{q}_{\mathbf{k},s} = i\hbar\delta_{\mathbf{k},\mathbf{k}'}\delta_{ss'}\,. \tag{2.30}$$

The Hamiltonian of this system has the form of a harmonic oscillator for each of the modes. Instead of the Hermitian operators $\hat{q}$ and $\hat{p}$, one can use the non-Hermitian annihilation and creation operators $\hat{a}$ and $\hat{a}^\dagger$

$$\hat{a}_{\mathbf{k},s} = \frac{1}{\sqrt{2\hbar\omega}}[\omega\,\hat{q}_{\mathbf{k},s} + i\,\hat{p}_{\mathbf{k},s}]\,, \tag{2.31}$$

$$\hat{a}^\dagger_{\mathbf{k},s} = \frac{1}{\sqrt{2\hbar\omega}}[\omega\,\hat{q}_{\mathbf{k},s} - i\,\hat{p}_{\mathbf{k},s}]\,, \tag{2.32}$$

$$[\hat{a}_{\mathbf{k},s}, \hat{a}^\dagger_{\mathbf{k}',s'}] = \mathbb{1}\delta_{\mathbf{k},\mathbf{k}'}\delta_{ss'}\,. \tag{2.33}$$

They satisfy the commutation relation given above and destroy or create excitations of the system. The excitations of the electromagnetic field are known as photons.

As in many physical systems, there are different ways of choosing the most appropriate basis. Above, a description in terms of planes waves was chosen. However, there are many equally suited sets of bases, e.g. wave packets, standing waves or, most interesting for this thesis, Laguerre-Gauss modes. As discussed in Ref. [19, Complement 4C] one can perform the transition between two sets of basis by a unitary transform. For the following calculation, it is assumed that the light propagates only in z-direction and the indices $\mathbf{k}$ and s are omitted. Since the Laguerre-Gauss modes represent a complete orthonormal basis of the field in the transverse plane, there exists a set of creation and annihilation operators $\hat{a}_{p,l}$ distinguishable by their radial and azimuthal indices p and l, respectively. These operators create and annihilate photons in the Laguerre Gauss mode which are the eigenstates of the quantum mechanical OAM operator [19]

$$\hat{\mathbf{L}} = \hbar \sum_{\mathbf{k},s,p,l} l\,\hat{a}^\dagger_{p,l}\hat{a}_{p,l}\mathbf{e}_z\,, \tag{2.34}$$

where $\mathbf{e}_z$ is the unit vector in z-direction.

2.3 Quantum key distribution

Based on the principles of quantum mechanics described above, one can develop new communication schemes. An overview of this topic can be found in Ref. [29] and a more detailed review is given in Ref. [30]. The following section is based on these two references.

Current classical encryption methods are based on the fact that it is computationally too expensive to break them. However, new algorithms both better classical algorithms as well as the development of quantum computers threaten their security. While classical algorithms may just raise the bar for encryption, quantum algorithms as for example the Shor algorithm may render them entirely insecure. A solution to this problem is the use of one-time pads, an encryption key that is used for only one message. To achieve complete security of the protocol, this key needs to be as long as the message to be encoded [31]. The main obstacle of this method is the secure transmission of the key between the two parties. A way to solve this problem is the so-called quantum key distribution which achieves its security from fundamental physical principles. Two parties, henceforth called Alice and Bob, create a one-time encryption key by quantum key distribution. The message to be exchanged is then encrypted with this key and could be transmitted by any communication channel. While there may be many different quantum systems to transmit information, photons are by far the most popular ones.

To this end, many quantum communication schemes have been developed; here, the BB84 (proposed by Bennett and Brassard in 1984 [32]) and the E91 (proposed by Ekert in 1991 [33]) protocol will be described in more detail. Both protocols can be used with qubit systems, a single qubit in the BB84 and two entangled qubits for the E91 protocol. Later in this thesis, the orbital angular momentum of light introduced in Sec. 2.1 is used to encode qubits. For better visualization, it is for now assumed that the qubits are encoded in the polarization degree of freedom. Both protocols draw their security from the fact that one cannot copy an arbitrary quantum state [34]. It is important to note that the quantum state needs to be arbitrary. If Alice were to use only two of the possible qubit states $|\uparrow\rangle$ and $|\rightarrow\rangle$, an eavesdropper could simply intercept Bob's photon and resend another photon based on the measurement result. A quantum key distribution protocol thus needs to make use of more than two states.

First, the BB84 protocol is described which is shown schematically in Fig. 2.4. In this protocol, Alice can prepare a single photon qubit in two different basis sets,

e.g. vertical and horizontal polarization $\{|\uparrow\rangle, |\rightarrow\rangle\}$, and diagonal and anti-diagonal polarization $\{|\nearrow\rangle, |\searrow\rangle\}$. Alice randomly chooses the basis in which the qubits are encoded and which of the two states to encode. An important condition for the choice of the basis sets is that they are mutually unbiased. This means that any two states of different basis sets have to have an overlap of 0.5 (in the qubit case). Hence, every state in one basis set has uniform probability for all states in the other basis set. An eavesdropper therefore has a 50% chance of choosing the wrong basis to measure in. Next, the photon is sent to Bob who randomly picks one of the two measurement basis sets. To obtain the key, Alice and Bob communicate, e.g. by a classical channel, which basis set they chose but not which value was encoded or measured. It is clear that their values are not correlated if they chose different (mutually unbiased) basis sets. If they chose the same basis, however, Bob's measurement result should be perfectly correlated with Alice's prepared value. An eavesdropper, typically called Eve, trying to intercept the photons sent to Bob has the problem that they have to properly guess the basis that Alice and Bob used. In any other case, Eve's measurement is in the wrong basis meaning that she sends a wrong photon to Bob with 50% probability. Hence, there will be some errors introduced by Eve's interception. To detect an eavesdropper, Alice and Bob need to determine the errors caused by Eve by calculating the so-called quantum bit error rate. They choose a fraction of their data and compare not only the basis but also the result of the measurement. With a detailed analysis, one can show that the BB84 protocol is secure, meaning that an eavesdropper cannot reconstruct the transmitted key, for a quantum bit error rate below 11% [35]. Clearly, the measurements used to determine the quantum bit error rate cannot be used to generate the key and thus reduce the key rate. However, it is a necessary step to determine whether the communication was secure.

A scheme based on entangled photons is the E91 protocol [33], visualized in Fig. 2.5. Instead of preparing a single-photon state, Alice has an entangled photon source. It produces a state as in Eq. (2.26)

$$|\Psi\rangle = \frac{1}{\sqrt{2}} \left(|\uparrow, \rightarrow\rangle - |\rightarrow, \uparrow\rangle \right) , \tag{2.35}$$

which has the special property that measurements on the two photons performed in the same basis are always anti-correlated. One of the photons is kept in Alice's laboratory and the other is sent to Bob via the quantum channel. Instead of the two basis sets from the BB84 protocol, three basis sets are used: for Alice $\{|\uparrow\rangle, |\rightarrow\rangle\}$, $\{|\nearrow\rangle, |\searrow\rangle\}$, $\{|\nearrow\rangle, |\searrow\rangle\}$, called a_1, a_2 and a_3, and for Bob $\{|\nearrow\rangle, |\searrow\rangle\}$, $\{|\nearrow\rangle, |\searrow\rangle\}$, $\{|\rightarrow\rangle, |\downarrow\rangle\}$, or
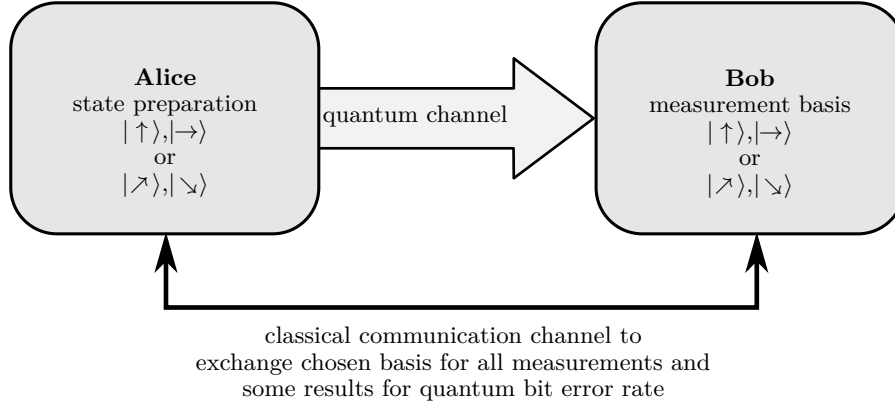
Figure 2.4: Schematic of the BB84 protocol. Alice creates a single-photon state either in the horizontal/vertical basis or in the diagonal/anti-diagonal basis. The photon is transmitted to Bob, who performs measurements in a randomly chosen basis set. Via a (classical) communication channel, Alice and Bob transmit their choices of basis for each photon.

b_1, b_2 and b_3. Alice and Bob perform measurements on their photons, independently choosing the measurement basis. Again, Alice and Bob use a classical communication line to compare in which basis they performed their measurements. As mentioned earlier, the outcome of measurements performed on the two photons is perfectly anti-correlated, if performed in the same basis. This happens for two of the nine possible combinations of basis sets (a_2, b_1) and (a_3, b_2). These measurements are used to generate the key. Furthermore, four of the other combinations are used to evaluate a Bell inequality, for example the Clauser-Horne-Shimony-Holt (CHSH) inequality [36], in particular,

$$B = E(a_1, b_1) - E(a_1, b_3) + E(a_3, b_1) + E(a_3, b_3). \qquad (2.36)$$

Here, $E(a_i, b_j)$ is the correlation coefficient between the measurements performed in basis a_i and b_j. In a classical measurement, the Bell parameter B can only take values between -2 and 2. For entangled states, however, B can take values between $-2\sqrt{2}$ and $2\sqrt{2}$. A violation of the inequality, i.e. $|B| > 2$, proves quantum mechanical correlations and thus serves as a test of a secure key exchange. Measurements performed by Alice and Bob in the remaining three of nine basis combinations are discarded.

The Bell parameter B can be calculated from a state's density matrix by performing the trace over the matrix product of ρ and the operator $\hat{B}$,

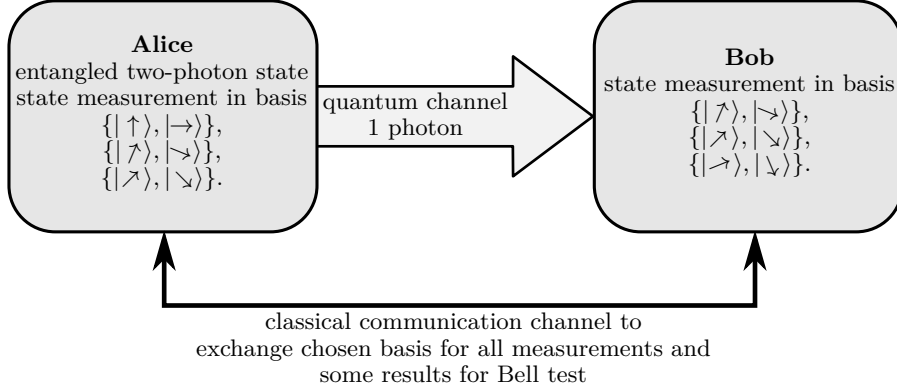$$B = \text{tr}(\hat{\rho}\hat{B}), \qquad (2.37)$$

Figure 2.5: Schematic of the E91 protocol. Alice has an entangled photon source. The first photon is sent to Bob and on the second Alice performs measurements in a random basis. Bob randomly chooses his basis sets. The chosen basis is communicated by an additional channel.

with

$$\hat{B} = 2\sqrt{2}\left(|\uparrow, \rightarrow\rangle\langle\rightarrow, \uparrow | + | \rightarrow, \uparrow\rangle\langle\uparrow, \rightarrow |\right) . \tag{2.38}$$

A derivation of this formula is given e.g. in the supplemental material of Ref. [37]; since the chosen initial state is different, one has to swap the matrix elements leading to the above equation. For example, the initial entangled state given by Eq. (2.26), achieves a maximum violation of this inequality with $-2\sqrt{2}$.

While for simplicity, the polarization basis was chosen to explain the quantum key distribution protocols described above, one can use any other suitable quantum mechanical property e.g. the orbital angular momentum degree of freedom which was introduced in Sec. 2.1. For the BB84 protocol, one could for example choose the following basis to encode qubits: $\{|-l\rangle, |+l\rangle\}$ and $\{|-l\rangle+|+l\rangle, |-l\rangle-|+l\rangle\}$. For the Ekert91 protocol, a photon source creating an OAM-entangled state like $|-l, l\rangle+|l, -l\rangle$ could be used. It should be stressed that OAM provides an, in principle, denumerably infinite-dimensional Hilbert space enabling also higher-dimensional encoding. However, the work presented in this thesis is restricted to OAM qubit transmission.

2.4 State of the art of communication with orbital angular momentum

In the following, a short summary of the literature on OAM communication is given. A more detailed review is given in Ref. [38] which discusses the advances in the field in the context of classical communication. Reference [39] summarizes the efforts in turbulence correction, including adaptive optics, for classical OAM communication. A review on the application of OAM in quantum physics can be found in Ref. [40].

The first proof-of-principle of classical communication with OAM encoding was given in 2004 [41]. It also showed that eavesdropping on OAM-encoded communication is difficult since one needs to intercept the beam at its optical axis without displacement. In addition, intercepting only a part of the beam's aperture leads to errors in the OAM measurement because of an uncertainty relation that exists between OAM and the angle in polar coordinates [42]. Since then, OAM has been combined with state-of-the-art communication systems to achieve data rates up to 1 Tbit/s [7] and even 100 Tbit/s [43], however, only for distances of a few meters. Over a distance of 120 m, OAM-multiplexing has been demonstrated with four modes [44]. In that case, turbulence was weak and did not limit the link performance. Another experimental study evaluated the phase profile of OAM beams after propagation through a 1.6 km long free-space channel in Erlangen [45]. Because of the limited aperture, a decrease of the total OAM was measured by a mode sorter. In an even longer link of 3 km across Vienna, OAM modes were used to transmit an image [46]. In particular, the information was encoded in the intensity profile of OAM mode superpositions with $+l$ and $-l$ which feature an l-fold petal structure. At the receiver, a neural network was used to determine the initial OAM since the beam was too distorted to couple into a telescope. The transmission over a record distance of 143 km was achieved between the Canary islands of La Palma and Tenerife [47]. Here, an observatory on Mount Teide, Tenerife, served as a giant screen to recognize the intensity pattern of OAM mode superpositions by a neural network similar to Ref. [46].

Already in the first experimental demonstration of OAM encoding, the effect of atmospheric turbulence was mentioned as a limiting factor [41]. Many studies have been devoted to determining the effect of turbulence on OAM modes. In weak turbulence that can be described by a single phase screen, analytical formulas can be found for the OAM mode crosstalk [14, 48]. For stronger turbulence, the channel crosstalk of a classical communication system was investigated numerically in Ref. [49] for a

large number of OAM states. In general, the crosstalk increases with the turbulence strength [14, 48, 49]. The weak turbulence predictions have been verified in laboratory experiments with spatial light modulators to introduce turbulence by a single phase screen [50, 51].

Clearly, atmospheric turbulence has a detrimental effect on OAM-based communication. Thus, the application of turbulence correction, e.g. by means of adaptive optics is feasible. Two experiments should be highlighted in this context, Ref. [11] and Refs. [12, 52]. Both experiments implement a static laboratory system which features a Gaussian beacon and a Shack-Hartmann wavefront sensor to measure turbulence-induced distortions. Reference [11] emulates thick atmospheric turbulence by a proper placement of two phase screens. The bits per photon achieved by OAM-encoding was strongly improved as compared to the uncorrected case. In Refs. [12, 52], a single phase screen emulates turbulence distortions and the classical bit error rate is measured for an OAM-multiplexed communication signal. While the bit error rates were very high without correction, adaptive optics could reduce it below the forward-error-correction limit which is required for further post-processing of the communication signal. Furthermore, Ref. [12] applied either a post-compensation at the receiver but also a pre-compensation at the transmitter. Similar approaches have been published with phase correction with a wavefront sensor [53], by phase retrieval with the Gerchberg-Saxton algorithm [54] or with learning algorithms [55]. A recent publication, proposes to correct for beam displacement without a beacon [56]. When a Gaussian beacon is applied in the experiments, its beam is expanded to increase the overlap with the OAM modes. A detailed investigation of the beacon's beam waist on the correction efficiency, in particular for quantum cryptography, is part of this thesis, see Ch. 6.

In addition to the applications in classical communication, OAM is also of great interest for quantum communication. In 2001, it was shown that photons can be entangled in the OAM degree of freedom [57]. Nowadays, OAM-entangled photons can be produced with mode numbers of several hundred [58]. In the laboratory, quantum key distribution with qutrits (three-dimensional quantum systems) was performed with a quantum bit error rate below 10% [59]. The influence of atmospheric turbulence on single photons was first investigated theoretically by Paterson [14]. A theoretical investigation of the entanglement decay of two OAM qubits suggested a better stability of higher-order OAM modes [15], which is however restricted to the regime of weak turbulence. This effect could be explained by introducing the so-called phase correlation length [60]. In the weak turbulence regime, only one parameter is needed to describe

this behavior – the ratio of the beam waist w_0 and the Fried parameter r_0 to describe atmospheric turbulence. However, in strong turbulence, a second parameter is needed and the stability of higher-order OAM modes is reduced [61]. In the laboratory, the entanglement decay has been studied with a single phase screen for two qubits [62] or for high-dimensional entanglement with a turbulence cell [63]. An experiment performed inside a hall with a 210 m free-space propagation demonstrated quantum key distribution with rotation-invariant states which employ both OAM and polarization [64]. In Ottawa, four-dimensional states were transmitted through a free-space link of 300 m. Again, a combination of OAM and polarization was used which reduced the impact of turbulence [9]. Over a 3 km free-space link in Vienna, OAM entanglement could be transmitted and verified for $l = 1$ and $l = 2$ [8]. Because of the strong turbulence distortions, the beams were identified with masks by their intensity profile [8] rather than coupling the light directly into a telescope.

While there have been impressive quantum experiments with OAM, they are always limited by atmospheric turbulence as soon as propagation distances are above several hundred meters. In this thesis, the possibility of applying adaptive optics to quantum cryptography is investigated. To the best of the author's knowledge, Ref. [28], which is part of this thesis, is the first publication to consider adaptive optics in this context. Details of the results will be given in Chs. 5 and 6. Before that, the required background knowledge and the used simulation methods are introduced both for the propagation through atmospheric turbulence, Ch. 3, and the adaptive optics system, Ch. 4.

Chapter 3

Atmospheric turbulence

When looking at the night sky, one can observe that the light of the stars twinkles. The cause of this effect is a variation of air pressure and temperature called atmospheric turbulence which distorts the light as if it were passing through many, very weak lenses. Atmospheric turbulence does not only limit astronomical observations but also free-space optical communication. Turbulence is particularly detrimental to OAM-encoded communication schemes because it distorts the phase into which information is encoded.

The first section of this chapter, Sec. 3.1, gives a general introduction to atmospheric turbulence and its effects on light propagation. In particular, the Kolmogorov theory of turbulence which is used throughout this thesis is introduced and the important parameters for optical turbulence resulting from it, the Fried parameter and the Rytov variance, are given. Afterwards, the split-step propagation method is described in Sec. 3.2 which is used in this thesis to numerically model the propagation through atmospheric turbulence. Finally, the choice of the simulation geometry and parameters is motivated in Sec. 3.3.

3.1 Light propagation through atmospheric turbulence

In this section, a short introduction to atmospheric turbulence is given and the turbulence parameters used in this thesis are defined. The presented material is based on Ref. [65], in particular Chs. 3, 5 and 7, as well as Ref. [23], Secs. 8.10-8.13. Earth's atmosphere consists of air and is subject to many external factors. The sunshine e.g. introduces energy to the system. While large wind flows distribute this energy in a

laminar fashion, on a smaller scale this energy is more efficiently transported by a turbulent flow. In a laminar flow, all particles move in the same direction and different layers cannot mix. Therefore, it is suitable for transportation of energy along larger distances. In contrast, the turbulent flow allows for mixing of air masses and, by that, for a faster distribution of energy and equalization of temperature on a smaller length scale. At even smaller length scales, the friction between the molecules in the air suffices to transport energy through dissipation. One can hence distinguish three regimes: the laminar flow at large length scales on the order of the so-called outer scale L_0, the turbulent flow, and the dissipation range for length scales on the order of the inner scale l_0. The range of turbulent flows $l_0 \ll l \ll L_0$ is called the inertial range.

At a certain position $\mathbf{r}$, the refractive index can be described by [65]

$$n(\mathbf{r}) = 1 + 77.6 \times 10^{-6}[1 + 7.52 \times 10^{-3}(\lambda/1\ \mu\text{m})^{-2}]\frac{P(\mathbf{r})/1\ \text{mbar}}{T(\mathbf{r})/1\ \text{K}}\,, \qquad (3.1)$$

in dependence of the local pressure P, temperature T and wavelength λ. The average value of the refractive index is 1 and the fluctuations $\delta_n(\mathbf{r})$ about the mean value are on the order of 10^{-6} [10]

$$n(\mathbf{r}) = 1 + \delta n(\mathbf{r})\,. \qquad (3.2)$$

Although these fluctuations are very small, they can have a strong impact on a light beam when it propagates longer distances from several hundred meters to several kilometers. At first, the beam only experiences phase distortions caused by the position-dependent refractive index variations. After longer propagation distances, the phase-distorted light interferes with itself and exhibits intensity distortions also known as scintillation. In strong turbulence, random speckle patterns develop. Moreover, light beams wander in the receiver plane which may lead to them missing the receiver aperture while in addition the angle-of-arrival fluctuates. Another effect of turbulence is the broadening of light beams. All these effects lower the transmission quality of light through atmospheric turbulence and thereby reduce, e.g., the data rate and reliability of free-space optical communication systems.

Therefore, it is important to understand the refractive index fluctuations and their influence on light. The mathematical description of the flows leading to the refractive index distortions is provided by the Navier-Stokes equation, a general solution of which has not been found or even proven to exist. In addition, the behavior of the turbulent flow is highly dependent on the boundary conditions, i.e. the initial state of the medium, which is hardly measurable. It is therefore more convenient to choose

a stochastic description of the turbulent atmosphere and by Eq. (3.1) of its refractive index.

The first approach to statistically describe a position-dependent quantity is often to find a dependence on said position. One can e.g. calculate the covariance function

$$B_n(\mathbf{r}_1, \mathbf{r}_2) = \left\langle \delta n(\mathbf{r}_1)\delta n(\mathbf{r}_2) \right\rangle, \tag{3.3}$$

which states how the refractive index variations at two positions are correlated. Here, $\left\langle \cdots \right\rangle$ denotes the ensemble average. Another approach is choosing a description in reciprocal space – the power spectrum – which gives the information how strongly certain spatial frequencies contribute to the quantity. In fact, the covariance and the power spectrum represent a Fourier transform pair according to the Wiener-Khinchin theorem [65]. The most famous power spectrum of refractive index fluctuations was derived by Kolmogorov based on scale arguments:

$$\Phi_n(\kappa) = 0.033\, C_n^2\, \kappa^{-11/3}, \qquad 1/L_0 \ll \kappa \ll 1/l_0\,, \tag{3.4}$$

where κ is the wavenumber in reciprocal space and C_n^2 is the refractive index structure constant. The underlying assumptions of this spectrum are stochastic homogeneity and isotropy. Homogeneity implies that the statistical properties of the fluctuations are independent of the position while isotropy makes them also independent of the direction. The refractive index structure constant C_n^2 has typical values between 10^{-17} m$^{-2/3}$ for weak turbulence and 10^{-13} m$^{-2/3}$ for strong turbulence. The power-law dependence also leads to the fact that turbulence has a fractal or self-similar appearance. The advantage of the Kolmogorov model is the simplicity of its form which makes it possible to evaluate many statistical quantities analytically. However, care must be taken outside of the inertial range, in particular for small wavenumbers where the spectrum diverges. There exist more specialized spectra such as the Tatarskii spectrum, the von Karman spectrum or the modified von Karman spectrum, which include the effects of the inner and outer scale, and even models with a different power law exponent. However, the use of such specialized spectra requires the precise knowledge of the associated turbulence parameters which strongly depend on the location of the experiment. Therefore, the calculations in this thesis are restricted to the Kolmogorov spectrum of turbulence.

The propagation of light, or more precisely of its electric field vector **E**, through an inhomogeneous medium[1], such as optical turbulence, can be described by the following

---

[1]It should be stressed that statistical homogeneity and the homogeneity of a medium refer to two different concepts. A homogeneous medium has a constant refractive index while statistical homogeneity implies that statistical quantities only depend on position differences but not the position itself.

wave equation [65]

$$\nabla^2 \mathbf{E}(\mathbf{r}) + k^2 n^2(\mathbf{r})\mathbf{E}(\mathbf{r}) = \mathbf{0}\,, \tag{3.5}$$

where it is assumed that there is no back-scattering or depolarization in the medium and $k = 2\pi/\lambda$ is the wavenumber. For a monochromatic wave propagating e.g. in z-direction, Eq. (3.5) can be replaced by a scalar equation valid for each of its components U

$$\nabla^2 U(\mathbf{r}) + k^2 n^2(\mathbf{r})U(\mathbf{r}) = 0\,. \tag{3.6}$$

It becomes clear from Eq. (3.1) that the refractive index fluctuation is small compared to the average value 1 such that the following approximation is justified:

$$n^2(\mathbf{r}) \approx 1 + 2\delta n(\mathbf{r})\,. \tag{3.7}$$

By separating the spatial profile from the propagation part $U = u\exp(ikz)$, the differential equation for propagation through turbulence is found:

$$\nabla^2 u + 2ik\partial_z u + 2\delta n(\mathbf{r})k^2 u = 0\,. \tag{3.8}$$

In free-space optical communication, one wants to send a confined light beam from one party to the other along a distance that is much larger than the beam's transverse extent. It is thus justified to use the paraxial approximation which states that

$$\left|\frac{\partial^2 u}{\partial z^2}\right| \ll \left|2k\frac{\partial u}{\partial z}\right|\,. \tag{3.9}$$

In consequence, the second derivative with respect to the propagation direction in the Laplacian can be neglected

$$\nabla_T^2 u + 2ik\partial_z u + 2\delta n(\mathbf{r})k^2 u = 0\,, \tag{3.10}$$

where ∇_T is the Laplacian restricted to the transverse coordinates.

   Optical turbulence is usually divided into two regimes – weak and strong scintillation. The Rytov variance given by

$$\sigma_R^2 = 1.23 C_n^2 k^{7/6} L^{11/6} \tag{3.11}$$

is the most common criterion to distinguish between weak ($\sigma_R^2 \lesssim 1$) and strong ($\sigma_R^2 > 1$) turbulence where L is the propagation distance. In weak turbulence, the Rytov variance is proportional to the irradiance fluctuations of a plane wave.

The first-order Rytov method represents a perturbational approach to solve Eq. (3.10) in the case of weak turbulence where optical turbulence consists mostly of phase distortions. The field at a distance z is given by the vacuum solution – here denoted by the index 0 – multiplied by a complex phase perturbation

$$u(\mathbf{r}, z) = u_0(\mathbf{r}, z) \exp[i\phi(\mathbf{r}, z)] \,, \tag{3.12}$$

with a slight deviation from the notation of Ref. [65]. The complex phase perturbation $\phi(\mathbf{r}, z)$ can be expanded in several orders of the perturbational approach. The real part of ϕ describes phase perturbations while the imaginary part is associated with intensity distortions. In the first order of perturbation, the phase is given by the accumulated refractive index fluctuations along a propagation distance [66]

$$\phi(\mathbf{r}, z) = k \int_0^z \delta n(\mathbf{r}, z') \mathrm{d}z' \,. \tag{3.13}$$

Please note that this approximation is only valid in the weak turbulence regime. This approach is also implemented numerically in the single and multiple phase screen method discussed in Sec. 3.2.

One important statistical quantity of the aforementioned phase distortions is the structure function D_ϕ which describes the difference of the phase distortions between two points $\mathbf{r}$ and $\mathbf{r}'$

$$D_\phi(\mathbf{r}, \mathbf{r}') = \left\langle [\phi(\mathbf{r}) - \phi(\mathbf{r}')]^2 \right\rangle. \tag{3.14}$$

In the case of the Kolmogorov spectrum, this is given by

$$D_\phi(\mathbf{r}, \mathbf{r}') = 6.88 \left(\frac{|\mathbf{r} - \mathbf{r}'|}{r_0} \right)^{5/3} . \qquad \text{Kolmogorov spectrum} \tag{3.15}$$

A detailed derivation of the phase structure function for different power spectral densities can be found in Ref. [66]. The newly introduced variable r_0 is the so-called Fried parameter. It was first derived by Fried in the context of optimizing the signal-to-noise ratio of a telescope [67] and takes values on the order of a few centimeters up to several tens of centimeters at exceptional observation sites in the visible range [23]. For a plane wave and a horizontal propagation path, it is given by

$$r_0 = \left(0.423 C_n^2 k^2 z \right)^{-3/5} . \tag{3.16}$$

It can be interpreted as the maximum distance of two points that experience similar turbulence. Accordingly, a large Fried parameter is associated with weak turbulence.

In large astronomical telescopes, the Fried parameter marks the transition between diffraction-limited and turbulence-limited resolution. Increasing the telescope aperture beyond the Fried parameter cannot increase its resolution, unless, turbulence correction e.g. by adaptive optics is applied.

For strong turbulence, intensity fluctuations become increasingly important, in addition to the phase distortions. Then, another parameter is required to properly describe the statistics of atmospheric turbulence. Commonly, the Rytov variance given in Eq. (3.11) is used in addition to the Fried parameter.

3.2   Split-step propagation

The phase screen model is a common method, also used in this thesis, to numerically model the propagation through optical turbulence. As mentioned in the previous section, the effect of turbulence consists mostly of phase distortions as long as it is weak enough. Then, it can be shown that a single infinitesimally thin phase screen, properly placed between the plane of the initial beam and the final plane, models turbulence distortions [65]. The phase screen, as the name suggests, introduces only phase distortions to the beam. Anywhere apart from the location of the phase screen, the light propagates as if it were in vacuum with $\delta n = 0$.

As soon as turbulence becomes stronger, this model starts to deviate from the statistical properties of three-dimensional turbulence. However, it is possible to divide the propagation distance into several shorter distances that all correspond to weak turbulence. As a result, the single phase screen model is replaced by a multiple phase screen model as depicted in Fig. 3.1. The phase screens need to be properly placed and their strength scaled such that the strong-turbulence characteristics can be recovered. In horizontal turbulence, one often assumes that C_n^2 is constant along the propagation distance. Then, equally spaced phase screens with almost equal turbulence strength can be employed. For slant and vertical paths, the phase screen positions and strengths need to be adjusted to the profile of C_n^2 along the propagation path. The phase screens need to be generated in accordance with the turbulence spectrum, as e.g. the Kolmogorov spectrum in our case. This section describes the split-step propagation implemented to simulate the propagation through atmospheric turbulence – first, the numerical propagation through vacuum and, second, the generation of the turbulent phase screens.

In order to propagate the light between the phase screens, a numerical beam prop-
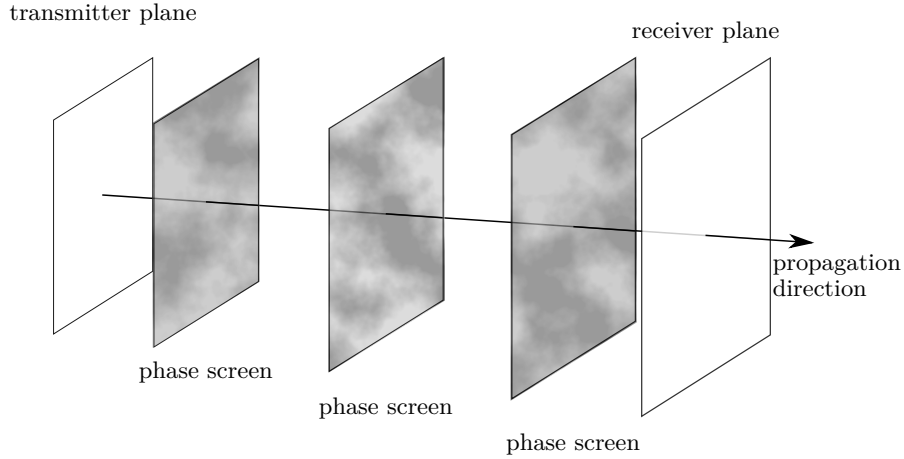
Figure 3.1: Schematic of the multiple phase screen or split-step model for 3 phase screens. The three-dimensional medium is replaced by a finite number of infinitesimally thin phase screens which introduce a random phase distortion as indicated by the false color profile of the screens. Between the steps, a vacuum propagation is performed.

agation needs to be implemented. Earlier, the scalar wave equation was used to derive the Laguerre Gauss modes, see Sec. 2.1. Instead of solving this differential equation, one can, based on a Green's function approach, calculate the Fresnel integral [68, p.67]

$$u(\mathbf{r}_2, z) = \frac{1}{i\lambda z} \iint u(\mathbf{r}_1, 0) \exp\left(\frac{ik}{2z}|\mathbf{r}_1 - \mathbf{r}_2|^2\right) \mathrm{d}\mathbf{r}_1 \,. \tag{3.17}$$

To find the field in the transverse plane $\mathbf{r}_2$ at a position z, one needs to know the input field in the transverse plane defined by $\mathbf{r}_1$ at a position $z = 0$. In the presented calculations, this would be the field distribution at the transmitter. The integral in the above equation can also be interpreted as a convolution of the function $u(\mathbf{r}, 0)$ and the complex phase factor $\exp(\frac{ik|\mathbf{r}|^2}{2z})$. This can be more efficiently solved by applying the convolution theorem. It states that a convolution in coordinate space is equivalent to a simple multiplication in Fourier space. Hence, one first calculates the Fourier transforms of the functions, multiplies them and then applies an inverse Fourier transform to obtain the convolution

$$u(\mathbf{r}_2, z) = \frac{1}{i\lambda z} \mathcal{F}^{-1}\left[\mathcal{F}\left[u(\mathbf{r}, \mathbf{0})\right] \mathcal{F}\left[\exp\left(\frac{ik|\mathbf{r}|^2}{2z}\right)\right]\right] \,. \tag{3.18}$$

This method can be implemented numerically by two Fast-Fourier-Transforms acting on a discretely sampled version of the input field. However, with this approach the grid spacing of the output plane equals that of the input plane.

By applying some algebra, one can reformulate Eq. (3.18) to allow for a scaling between the input and output plane sampling $\alpha = \delta_{out}/\delta_{in}$ where $\delta_{in/out}$ is the sampling in the input and output plane, respectively. The detailed calculation can be found in Ref. [69, p. 98] which leads to the expression

$$u(\mathbf{r_2}, z) = \frac{\exp(-\frac{ik}{2z}\frac{1-\alpha}{\alpha}r_2^2)}{i\lambda z} \iint U(\mathbf{r_1}) \exp\left(\frac{ik}{2z}(1-\alpha)r_1^2\right) \exp\left(\frac{ikm}{2z}\left|\mathbf{r_2}/\alpha-\mathbf{r_1}\right|^2\right)\mathrm{d}\mathbf{r_1}\,. \quad (3.19)$$

One can see that the output plane coordinate $\mathbf{r_2}$ is now scaled by α as compared to Eq. (3.17). In this thesis, the code provided in Ref. [69] was used to perform the beam propagations, i.e. to evaluate Eq. (3.19). The sampling requirements as well as the overall propagation geometry are discussed later in Sec. 3.3. Next, the second building block of the split-step simulation, the random phase screens, are discussed.

To most accurately model the atmosphere, the spatial characteristics of the phase screen should match those of the atmosphere. In the following, the phase screen generation and verification is discussed. For the phase screen generation, the code from Ref. [69] was used which implements the method by Lane et $al.$ [70]. Throughout this thesis, turbulence is assumed to follow the Kolmogorov spectrum introduced in Sec. 3.1.

The simplest and fastest generation method is based on Fast-Fourier-Transforms [71]. First, one generates Gaussian random numbers $b(\kappa)$ in the frequency domain with a mean value of 0 and variance of 1. To match the turbulence spectrum, these random numbers are multiplied by the square root of $\Phi(\kappa)$. Finally, to obtain a phase screen in coordinate space, one has to perform an inverse Fourier transform

$$\varphi(\mathbf{r}) = \iint b(\boldsymbol{\kappa})\sqrt{\Phi(\boldsymbol{\kappa})}e^{-2\pi i \boldsymbol{\kappa}\cdot\mathbf{r}}\mathrm{d}\boldsymbol{\kappa}\,. \quad (3.20)$$

For a numerical evaluation, Eq. (3.20) is discretized in a rectangular, linearly spaced grid with $N \times N$ samples

$$\varphi(m\,\delta x, n\,\delta y) = \sqrt{\delta\kappa_x\,\delta\kappa_y} \sum_{p,q} b_{p,q}\sqrt{\Phi(p\,\delta\kappa_x, q\,\delta\kappa_y)}e^{-2\pi i(pm\delta x\delta\kappa_x + qn\delta y\delta\kappa_y)}\,, \quad (3.21)$$

where all indices m, n, p, q run from $-N/2$ to $N/2 - 1$. This can be evaluated with a Fast-Fourier-Transform if the spacing in reciprocal and coordinate space obey the following relation

$$\delta\kappa_x = \frac{1}{N\delta x} \qquad \text{and} \qquad \delta\kappa_y = \frac{1}{N\delta y}\,. \quad (3.22)$$
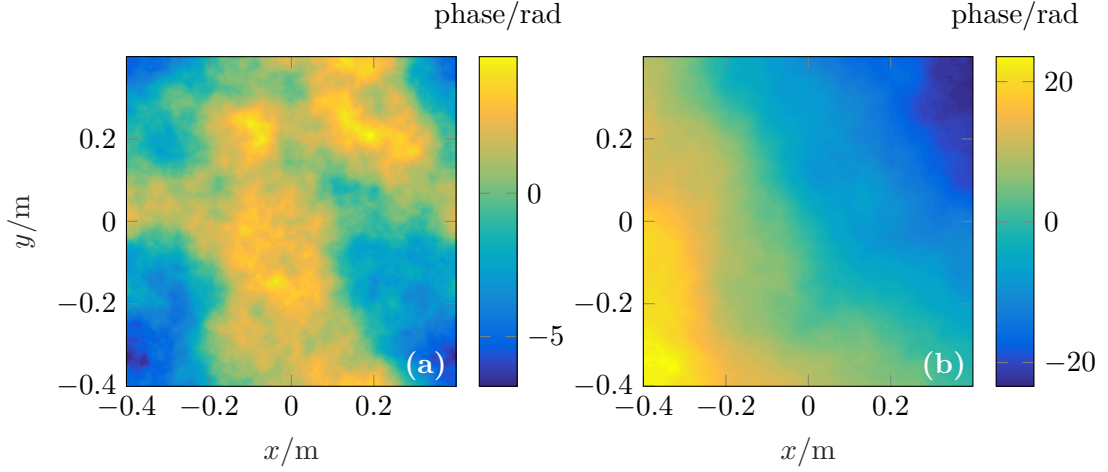
Figure 3.2: Random phase screens generated (a) with Fast-Fourier-Transform method and (b) with an additional subharmonic grid. The Fast-Fourier-Transform phase screen is periodic at its boundaries leading to reduced low-frequency content. In contrast, the screen with an additional subharmonic grid (7 subharmonic orders), has a large tip-tilt over the screen area. Both screens have a side length of 0.8 m and a Fried parameter of 0.1 m.

The final phase screen is given by

$$\varphi_{FFT}(m\,\delta x, n\,\delta y) = \sqrt{\delta\kappa_x\,\delta\kappa_y}\,\mathrm{FFT}\left[b_{p,q}\sqrt{\Phi(p\,\delta\kappa_x, q\,\delta\kappa_y)}\right]\,, \tag{3.23}$$

where FFT is short-hand for Fast-Fourier-Transform. This method is quite fast, even for large phase screens. Unfortunately, the generated screens are periodic, as can be seen in Fig. 3.2 (a). Hence, they do not contain tip and tilt which, however, have the highest contribution to the wavefront error [72]. In particular, tip and tilt induce beam wander which would not be properly modeled.

One way to add more low-frequency content to the aforementioned phase screens is by using an additional subharmonic (SH) grid as described by Lane *et al.* [70]. Here, the Cartesian grid from the Fast-Fourier-Transform method is divided near the origin into logarithmically spaced subgrids of 3×3 grid points each. The square at the origin is iteratively divided into more 3×3 grids. Because of the logarithmic sampling, one cannot use a Fast-Fourier-Transform for the subharmonic grid, but rather has to evaluate the sum directly

$$\varphi_{SH}(m\,\delta x, n\,\delta y) = \sum_{s=1}^{s_{max}}\sum_{p=-1}^{1}\sum_{q=-1}^{1}\frac{1}{3^s}\sqrt{\delta\kappa_x\,\delta\kappa_y}\,c_{s,p,q}\sqrt{\Phi(\kappa_p, \kappa_q)}e^{2\pi i(\kappa_p m\delta x + \kappa_q n\delta y)}\,, \tag{3.24}$$

$$\text{with} \quad \kappa_p = \frac{\delta\kappa_x p}{3^p}, \qquad \kappa_q = \frac{\delta\kappa_y q}{3^q}\,. \tag{3.25}$$

The matrix $c_{s,p,q}$ consists of s_{max} $3{\times}3$ Gaussian random number matrices with vanishing mean and variance equal to 1; $\delta\kappa_x$ and $\delta\kappa_y$ are equal to the frequency sampling of the Fast-Fourier-Transform phase screen defined in Eq. (3.22). The scaling factor $1/3^s$ in Eq. (3.24) accounts for the area that the subharmonic grid points occupy. In addition, the spectrum is set to zero at the origin ($p = 0, q = 0$) because the Kolmogorov spectrum diverges for vanishing frequencies. Finally, the low-frequency subharmonic phase screen is added to a high-frequency phase screen generated with the Fast-Fourier-Transform method

$$\varphi(m\,\delta x, n\,\delta y) = \varphi_{FFT}(m\,\delta x, n\,\delta y) + \varphi_{SH}(m\,\delta x, n\,\delta y)\,. \tag{3.26}$$

An example of the resulting phase screens is shown in Fig. 3.2 (b). One can see that the screen now exhibits a tip-tilt component as compared to the screen using only the Fast-Fourier-Transform approach from Fig. 3.2 (a).

To verify the generated screens and choose the appropriate number of subharmonics s_{max}, one can consider the phase structure function D_ϕ. It can be conveniently calculated by a Fast-Fourier-Transform [69] from zero-padded versions of the generated phase screens. This calculation needs to be repeated for a large number of realizations. The resulting two-dimensional ensemble-averaged structure function matrix is then averaged over the angle to obtain only the radial dependency. Figure 3.3 compares the structure function for different numbers of subharmonic grids for a specific example of screen size and Fried parameter. It demonstrates the improvement that can be achieved by increasing the number of subgrids. In Ref. [69], the low-order phase screen is composed of three subgrids whereas Lane *et al.* [70] suggest using at least five subgrids. The phase screens in this thesis were generated with 7 subharmonic orders.

3.3 Propagation scenario and simulation parameters

In the following, the propagation geometry and the simulation scenario are detailed. These parameters will be used in Chs. 5 and 6 to calculate the propagation of orbital angular momentum photons through the atmosphere. The choice of the right simulation parameters is crucial both in terms of defining a sensible application scenario and to avoid numerical issues in the calculation, e.g. due to bad sampling. Further, the number of phase screens required to accurately model the statistics of three-dimensional turbulence is determined. Finally, the sampling of the simulation routine is considered to avoid aliasing and wrap-around effects. The resulting parameters of the simulation
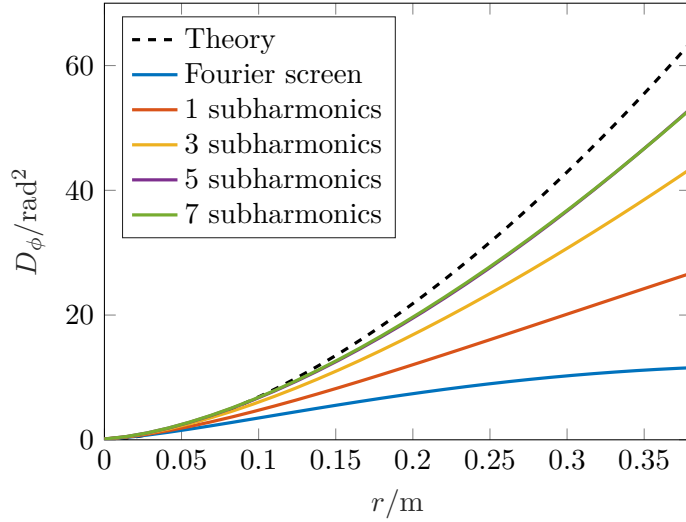
Figure 3.3: The structure function $D_\phi(r)$ for different numbers of subharmonic grids. As the number of subharmonics increases, the closer do the curves follow the theoretical structure function (black dashed line) for the Kolmogorov spectrum given in Eq. (3.15). The lines for 5 and 7 subharmonic orders almost coincide. The calculation was performed for a Fried parameter of 0.1 m and an aperture of 0.8 m and is averaged over 1000 realizations.

routine are summarized in Tab. 3.1. The following parameters are determined: the propagation distance, wavelength, transmitter and receiver aperture, and the initial beam waist. As turbulence parameter the ratio w_0/r_0 is chosen from which all other parameters (e.g. C_n^2 or σ_R^2) can be calculated. Finally, the parameters of the simulation such as the number of phase screens, input and output plane sampling and the number of sampling points are determined.

The propagation distance z was chosen to be 1000 m. In an earlier publication by the author [28], a shorter propagation of only 500 m distance was simulated. For this thesis, a longer distance was chosen for two reasons. First, an experiment without adaptive optics demonstrating OAM quantum communication with hybrid OAM and polarization-encoded photons was demonstrated in Ottawa, Canada, over an approximate distance of 500 m [9]. Hence, 500 m may be too short a distance to fully determine the potential of AO. Second, experiments with a distance of 3000 m in Vienna demonstrated that the OAM modes were severely distorted [46, 73]. In one case, the intensity distribution was analyzed by means of a machine learning algorithm [46]. In the other case, it was possible to couple into a telescope, but again only the intensity profile could be analyzed by masks and not the phase [73]. Experiments in Erlangen over 1600 m indicated a strong distortion of OAM beams [45]. Hence, a distance of

Parameter	Value
Distance z	1000 m
Wavelength λ	1064 nm
Transmitter aperture D	200 mm
Initial beam waist w_0	26 mm
Beacon beam waist w_b	$2.45 w_0$ *
Receiver aperture	300 mm
Maximum value of C_n^2	$1.02 \times 10^{-13} \text{m}^{-2/3}$
Number of phase screens N_{PS}	12
Position of ith phase screen	$\frac{i-1/2}{N_{PS}} z$
Number of sampling points N	1024
Sampling in transmitter plane δ_{in}	0.845 mm
Sampling in receiver plane δ_{out}	1.17 mm

Table 3.1: Summary of the simulation parameters used throughout this thesis. The beacon beam waist (marked by $*$) was fixed in Ch. 5 and iterated over in Ch. 6.

1000 m represents an intermediate value in between these two extremes. Additionally, it represents a plausible distance for an OAM quantum link e.g. within a city.

For the wavelength, a value of 1064 nm was chosen. There exist some entangled photon sources with such a wavelength [74]. Other common wavelengths for such sources are 810 nm [75] as well as 1550 nm [76]. Because the adaptive optics system, upon which the realistic adaptive optics calculations are based, operates at 1064 nm, see Sec. 4.4, this wavelength choice allows a direct comparison with measured data of the AO system. Finally, it should be stressed that one can rescale results obtained with a certain set of parameters to another. This is possible because only two parameters are required to describe the action of OAM photons in turbulence – the ratio between the Fried parameter and the beam waist w_0/r_0 and the normalized propagation distance $t = z/z_R$ [61]. Both the Fried parameter (see Sec. 3.1) and the Rayleigh range (see Sec. 2.1) depend on the wavelength. After a careful rescaling of said parameters, one can obtain results on light with another wavelength.

Now that the propagation distance and wavelength have been fixed, only one free parameter remains for the turbulence conditions, e.g. the Fried parameter. It has been observed that the concurrence drops dramatically when the transition between weak and strong scintillation occurs at $\sigma_R^2 = 1$ [77] which with the chosen parameters corresponds to $w_0/r_0 = 1.05$. To properly observe this transition, the maximum value of w_0/r_0 is chosen to be twice as high, i.e. 2.1. This would be equivalent to a refractive index structure constant as high as $C_n^2 = 1.02 \times 10^{-13} \text{m}^{-2/3}$ or a Rytov variance of $\sigma_R^2 = 3.17$.

Another important quantity of the propagation geometry are the transmitter and receiver apertures. To determine their optimum size, the beam broadening caused by both diffraction and atmospheric turbulence was calculated as a function of the initial beam waist. As an upper limit for the transmitting aperture, a value of 200 mm was chosen for which lenses are commercially available. Mirror telescopes can be built with much larger apertures but typically have a central obscuration. For OAM modes, this may be problematic since their defining feature, the vortex at the axis of the beam, could be affected by such an obscuration. Depending on the required power transmission, here chosen to be 99%, one can determine the maximum beam waist for the aperture. For a Gaussian beam, this is fulfilled if $D \geq \pi w_0$. Since Laguerre-Gauss modes have a larger beam radius by a factor of $\sqrt{l+1}$ (for vanishing radial index), this leads to

$$D \geq \pi w_0 \sqrt{l_{max} + 1} \, . \tag{3.27}$$

With OAM values up to 5, the maximum initial beam waist w_0 is 26 mm for a 200 mm aperture. As a lower bound for the beam waist, a value of 1 mm was chosen which is still achievable with conventional fiber collimators.

When choosing the beam waist at the transmitter, the associated beam radius at the receiver should be reasonably small such that it can be coupled into the receiving telescope aperture. While there is a vast literature on the turbulence-induced beam broadening of Gaussian beams, see e.g. Ref. [65], only one publication with an analytical formula for the Laguerre-Gauss beam radius in turbulence was found [78]. Their analytical calculations suggest that Laguerre-Gauss modes, while having a larger initial beam radius, experience less beam broadening in turbulence than Gaussian modes. A similar conclusion was drawn in Ref. [79] from a numerical split-step simulation. Please note that, in contrast to the beam waist parameters w_0 and $w(z)$ which are equal for all OAM modes because of the chosen parameters, the quantity of interest here is the root-mean-square radius of the beam. For a Gaussian beam, Ref. [78] finds the same results as commonly found in the literature [65] in the strong scintillation regime[2]

$$w_{LT} = w\sqrt{1 + 1.63(\sigma_R^2)^{6/5}\frac{2z}{kw^2}} \qquad \text{with} \qquad w = w_0\sqrt{1 + z^2/z_R^2} \, , \tag{3.28}$$

where w_{LT} denotes the long-term beam radius in turbulence and w corresponds to the diffraction-limited beam waist. For the average beam radius of Laguerre-Gauss modes

---

[2]The Fried parameter has to be larger than the inner scale of turbulence, i.e. $r_0 \gg l_0$.
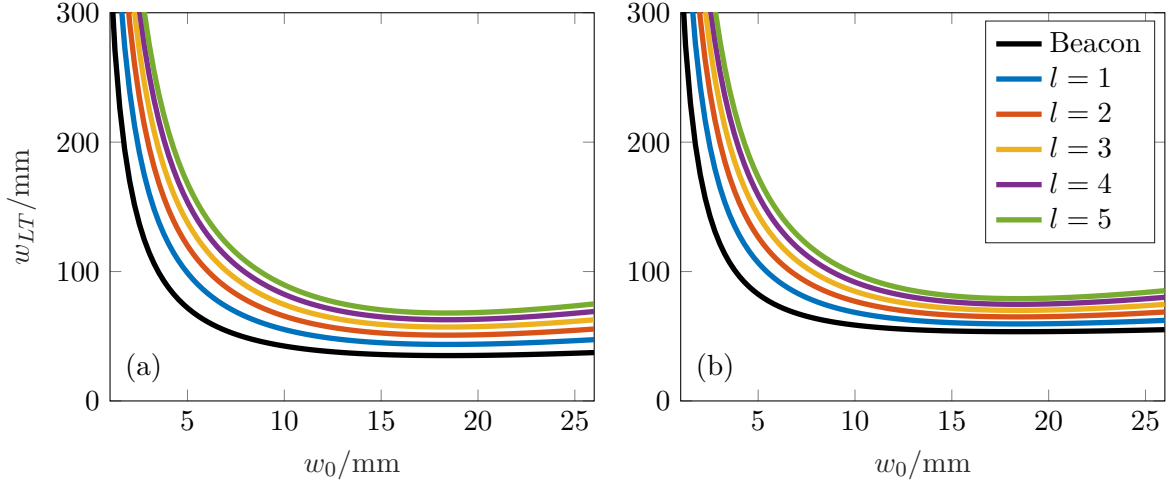
Figure 3.4: Beam radius in 1000 m distance, (a) for $\sigma_R^2 = 1$, (b) for $\sigma_R^2 = 3.17$, calculated from Eq. (3.29). For small initial beam waists, the beam radius at the receiver increases strongly. In contrast, for larger beam diameters, the differences are not very pronounced.

with azimuthal index l and radial index $p = 0$, the following formula can be found [78]:

$$w_{LT,0,l} = w_{LT}\sqrt{1 + l\frac{w^2}{w_{LT}^2}} \,. \qquad (3.29)$$

Figure 3.4 shows the long-term beam radius according to Eq. (3.29) at the receiver in 1000 m distance for two turbulence conditions, (a) $\sigma_R^2 = 1$ and (b) $\sigma_R^2 = 3.17$ calculated from Eq. (3.29). It can be seen that a small initial beam waist below 5 mm, would require large collecting telescopes on the order of 1 m. Above 10 mm initial beam waist, the dependence on w_0 becomes relatively flat. Comparing the two turbulence conditions in (a) and (b), one sees that for stronger turbulence the received beam waist becomes larger. However, the differences between the different OAM modes become smaller as previously noted in Ref. [78].

Based on these considerations, an initial beam diameter of 26 mm was chosen for the Laguerre-Gauss modes which is the largest diameter achievable with the provided transmitter telescope aperture of 200 mm. Table 3.2 lists the calculated beam radius at the receiver for the different modes. The largest beam waist at the receiver has a value of 85 mm. As discussed earlier, the aperture needs to be at least a factor of π larger than the beam waist in order to collect more than 99% of the incoming light's power. A receiving aperture of 300 mm thus comfortably fits the received modes and has been previously used for measurements with the realistic AO system developed at Fraunhofer IOF [80], see also Sec. 4.4.

	Beam radius in mm		
l	vacuum	$\sigma_R^2 = 1$	$\sigma_R^2 = 3.17$
0	29	35	54
1	41	47	62
2	50	56	69
3	58	63	75
4	65	69	80
5	71	75	85

Table 3.2: Average beam radius at the receiver for different values of l and turbulence strength in 1000 m distance for $w_0 = 26$ mm.

The number of phase screens is an important parameter for a split-step propagation because it influences the reliability of the simulation, in particular, how well it approximates the three-dimensional turbulent medium. In this section, the approach presented in Ref. [69, Ch. 9] as well as Ref. [65, Chs. 5-6] is followed and adapted to the chosen propagation scenario described above. The first assumption of this calculation is that the turbulence distortions are homogeneous along the propagation path, meaning that the refractive index structure constant C_n^2 is constant. For such a scenario, it is convenient to choose equidistantly spaced phase screens. The propagation distance is divided into N_{PS} shorter distances. For each of these steps, the three-dimensional medium is replaced by a phase screen at the center of the step and vacuum propagations between the screens.

With the split-step method, the Fried parameter and Rytov variance for propagation through extended turbulence, need to be reproduced, see Eqs. (3.11, 3.16). Please note that Ref. [69] uses the scintillation index to derive the number of phase screens, while here for consistency the Rytov variance is considered. In the weak turbulence regime, the Rytov variance is proportional to the scintillation index $\sigma_R^2 = 4\sigma_\chi^2$. The formulas given in Ref. [69] have thus been multiplied by a factor of 4. In the strong scintillation regime, σ_χ^2 saturates while σ_R^2 continually grows, unlike the scintillation experienced by light. The contribution of the individual screens to the overall scintillation depends both on their Fried parameters $r_{0,i}$ and on their positions z_i

$$r_0 = \left(\sum_{i=1}^{N_{PS}} r_{0,i}^{-5/3} \right)^{-3/5}, \tag{3.30}$$

$$\sigma_R^2 = 5.32 k^{-5/6} z^{5/6} \sum_{i=1}^{N_{PS}} r_{0,i}^{-5/3} \left(1 - \frac{z_i}{z} \right)^{5/6}, \tag{3.31}$$

given here for a plane wave. This procedure is described in more detail in Ref. [69,

p. 164 ff.]. In the chosen propagation scenario, the positions and propagation distances of the ith phase screen are given by

$$\Delta z_i = \frac{z}{N_{PS}}, \qquad \text{and} \qquad z_i = \frac{i - 1/2}{N_{PS}} z \,. \tag{3.32}$$

For equally spaced phase screens with constant C_n^2, the Fried parameters of the individual screens all have approximately the same value $r_{0,PS}$

$$r_0 = N_{PS}^{-3/5} r_{0,PS} \,. \tag{3.33}$$

With the help of Eqs. (3.32) and (3.33), the formula for the Rytov variance can be further simplified

$$\sigma_R^2 = 5.32 k^{-5/6} z^{5/6} r_0^{-5/3} \frac{1}{N_{PS}} \sum_{i=1}^{N_{PS}} \left(1 - \frac{i - 1/2}{N_{PS}}\right)^{5/6} \,. \tag{3.34}$$

In the split-step propagation, each phase screen should only introduce weak scintillation. It is known that phase screens at a large distance from the receiver contribute most to intensity variations. Hence, it suffices to ensure weak scintillation for the first phase screen in order to meet the condition for all screens. Formally, this behavior can be seen in Eq. (3.34) where the first element of the sum has the highest value $\sigma_{R,1}^2$

$$\sigma_{R,1}^2 = 5.32 k^{-5/6} z^{5/6} r_0^{-5/3} \frac{1}{N_{PS}} \left(1 - \frac{1}{2 N_{PS}}\right)^{5/6} \,. \tag{3.35}$$

For the Rytov variance, weak scintillation occurs up to $\sigma_R^2 \sim 1$. Since this is only a vague criterion and to avoid entering the transition regime from weak to medium turbulence, it is required in the following calculation that the Rytov variance of each phase screen should be smaller than 0.5, thus adding a safety factor of 2. Unfortunately, Eq. (3.35) is hard to solve for N_{PS}. One possibility is to iterate over N_{PS} and choose the first value that fulfills the requirement. A simpler solution can be found by approximating Eq. (3.35). For large values of N_{PS}, the factor $(1 - \frac{1}{2N_{PS}})^{5/6}$ becomes small and can be neglected. For example, the introduced error is less than 5% if N_{PS} is larger than 10. Rewriting the condition $\sigma_{R,1}^2 < 0.5$ thus yields

$$N_{PS} > 10.64 k^{-5/6} z^{5/6} r_0^{-5/3} \qquad \text{for } N_{PS} \gtrsim 10 \,. \tag{3.36}$$

With the chosen parameters from above, the minimum number of phase screens is determined to be 12 for the strongest simulated turbulence with $w_0/r_0 = 2.1$. This number has been used for the simulations. The Fried parameters of the individual

screens are found by a linear fit of Eqs. (3.30, 3.31) to the values for extended turbulence in Eqs. (3.16, 3.11); for details see Ref. [69].

For the numerical calculations, one needs to sample the involved functions on a discrete grid. To avoid numerical artifacts, the following parameters need to be chosen carefully: input and output plane grid spacing, δ_{in} and δ_{out}, and the number of samples in each direction N. It is assumed that the sampling is uniform in x- and y-direction. For these considerations, the simulated areas of interest in the initial plane D_1 and the final plane D_2 are important. In this case, they are given by the transmitter and receiver aperture sizes. Please note that the computation grid in both planes is chosen larger than these areas of interest. First, the input sampling δ_{in} is derived for the Laguerre-Gauss modes based on the Nyquist criterion. Afterwards, the remaining parameters are derived by the sampling criteria presented in Ref. [69].

The Nyquist criterion states that, for a band-limited input signal, the spacing needs to allow at least 2 data points within one period of an oscillating wave [81], i.e.

$$\delta_{in} \leq \frac{1}{2 f_{max}} \, . \tag{3.37}$$

First, the easiest case of a Laguerre-Gauss mode, namely the Gaussian beam ($p = 0, l = 0$), in particular its spatial frequency spectrum, is considered. The Fourier transform of a Gaussian mode function has again Gaussian shape with a waist of $2/w_0$ in Fourier space. Technically, the Gaussian beam spreads infinitely in transverse space and is, in fact, not a band-limited function. However, choosing the simulated area large enough can ensure that a large percentage of the optical power is indeed considered in the simulation. To obtain more than 99% of the power in Fourier space, as in the derivation of the transmitter apertures in coordinate space, one has to consider an area with a diameter of π times its waist (in Fourier space), see also Eq. (3.27),

$$f_{max,Gauss} = \frac{2\pi}{w_0} \, . \tag{3.38}$$

In the next step, the Fourier space diameter of the Laguerre-Gauss modes with $p = 0$ and $l \neq 0$ needs to be calculated. First, the Fourier transform of the Laguerre-Gauss modes with $p = 0$ and azimuthal index l is calculated. The result has the form of the Laguerre-Gauss modes ($p = 0$, azimuthal index l) in coordinate space, but with a waist $\widetilde{w}_0 = 2/w_0$. The details of this calculation can be found in appendix A. Based on this similarity, one can immediately deduce that, as in coordinate space, the waist of the modes scales with $\sqrt{l+1}$ as compared to Gaussian modes. This leads to

$$f_{max,LG} = \frac{2\pi}{w_0} \sqrt{l_{max} + 1} \, , \tag{3.39}$$

where l_{max} is the highest value of l in the simulation and equal to 5 in this thesis. Combined with Eq. (3.37), this results in a relation for the transmitter plane sampling

$$\delta_{in} \leq \frac{w_0}{4\pi\sqrt{l_{max}+1}} \, . \tag{3.40}$$

This upper bound was chosen for the initial plane sampling, i.e. $\delta_{in} = 0.845$ mm. In Ch. 6, the influence of the beacon waist, denoted by w_b, is investigated. With the chosen parameters and sampling, it is possible to simulate a range of $1/\sqrt{6}w_0 \leq w_b \leq \sqrt{6}w_0$ – the lower bound given by Eq. (3.40) and the upper bound is determined by the aperture size, see Eq. (3.27).

Next, the sampling criteria from Ref. [69] are considered. The sampling for the receiving plane has to fulfill [69] :

$$\delta_{out} \leq \frac{\lambda z - D_2' \delta_{in}}{D_1'} \, , \tag{3.41}$$

where the modified aperture sizes include a beam blurring induced by atmospheric effects

$$D_{1/2}' = D_{1/2} + c\frac{\lambda z}{r_0} \, . \tag{3.42}$$

For the scalar factor c, a value of 2 was chosen (range from 2 and 8). To obtain an integer number of pixels (256) along the aperture diameter of 300 mm, $\delta_{out} = 1.17$ mm was picked which is in accordance with the bound given by Eq. (3.41) of 1.789 mm.

Finally, the total number of sampling points N and thus the size of the entire simulated area needs to be chosen. In particular, it needs to be large enough to avoid wrapping effects which lead to contributions from the outer rim of the computational array to be scattered back into the center of the receiver plane

$$N \geq \frac{D_1'}{2\delta_{in}} + \frac{D_2'}{2\delta_{out}} + \frac{\lambda z}{\delta_{in}\delta_{out}} \, , \tag{3.43}$$

which is equal to 959 with the chosen parameters. For the simulations, the number of sampling points was chosen to be $N = 1024$ which is the next-higher integer power of two. The remaining sampling constraints in Ref. [69] refer to the radius of curvature of the initial wavefront and the maximum step size. Both criteria are fulfilled with the chosen sampling parameters.

Chapter 4

Adaptive optics – theory and simulation

To correct for the turbulence-induced distortions of light beams described in the previous chapter, adaptive optics (AO) can be applied. In the first section of this chapter, the general working principle of AO is explained. This is the last section that is based on the literature. The following sections, 4.2 to 4.6 represent the work performed for this thesis. In particular, the three different simulation models of adaptive optics are introduced which are used to obtain the results of this thesis presented in Chs. 5 and 6. In Sec. 4.2, an idealized AO system is presented. The next section 4.3 describes the simplest AO possible, which corrects for the tip and tilt degrees of freedom. The idealized and tip-tilt AO systems can be seen as the limiting cases for best and worst possible performance. The third AO model is based on an existing setup developed at Fraunhofer IOF in the last few years. The author was part of the team developing this system. Reference [13] is part of the work performed for this thesis and describes the first results obtained with the system in the context of Earth-to-satellite communication. It also contains the details of the setup and its application scenario. In particular, the author derived the requirements for the AO system based on the application scenario such as the number of deformable mirror actuators, actuator stroke, tip-tilt mirror stroke and AO system bandwidth and performed the final data analysis. Section 4.4 details how the system was simulated in this thesis. In the next section 4.5, the efficiency of the three introduced models is compared. Finally, Sec. 4.6 describes the simulation routine which combines the split-step propagation from Ch. 3 and the adaptive optics modeling from this chapter.

4.1 Working principle of adaptive optics

To counter-act the influence of optical turbulence, a technology called adaptive optics (AO) has been developed in the past few decades. The contents of this section is based on Ref. [10]. Since a large variety of technological approaches exist that go beyond the scope of this thesis, only the most common systems are described here. Most AO systems are based on the principle of correcting the phase ϕ of the received light described by u

$$u(\mathbf{r}) = |u(\mathbf{r})|e^{i\phi(\mathbf{r})}\,. \tag{4.1}$$

By applying the complex conjugate phase, e.g. with help of a deformable mirror, the phase can be corrected for

$$u_{\mathrm{corr}}(\mathbf{r}) = u(\mathbf{r})e^{-i\phi(\mathbf{r})}\,. \tag{4.2}$$

In case of weak turbulence, this should suffice to recover a diffraction-limited optical quality. The efficiency is limited in the strong turbulence regime when intensity fluctuations become significant.

A typical phase-correcting AO system – with a wavefront sensor, tip-tilt and deformable mirror which are all connected by a fast control loop – is shown in Fig. 4.1. First, the wavefront sensor measures the turbulence distortion of a reference object such as the light of a nearby star or of a reference laser beam. Next, a corrective element such as a deformable mirror, a tip-tilt mirror or a spatial light modulator is used to correct for the phase distortion. The connection between the wavefront measurement and the corrective elements requires a fast control loop since the characteristic frequency of turbulence is on the order of tens to several hundred Hertz [10, p. 39]. Figure 4.1 depicts a closed-loop system where the light is first reflected by the tip-tilt and the deformable mirror and the wavefront sensor thus measures the residual wavefront distortion.

This very common AO configuration is also known as post-compensation since the beam's wavefront is corrected at the receiver. An alternative approach, which is particularly interesting for Earth-to-satellite compensation, is called pre-compensation. Here, the light beam receives AO correction before it experiences turbulence distortion. The reference object, in optical communication the so-called beacon laser, has to propagate along the same path as the light to be corrected but in opposite direction. The uplink in an Earth-to-satellite link can only be pre-compensated because the turbulence distortion is predominant in lower atmospheric layers. A phase correction is
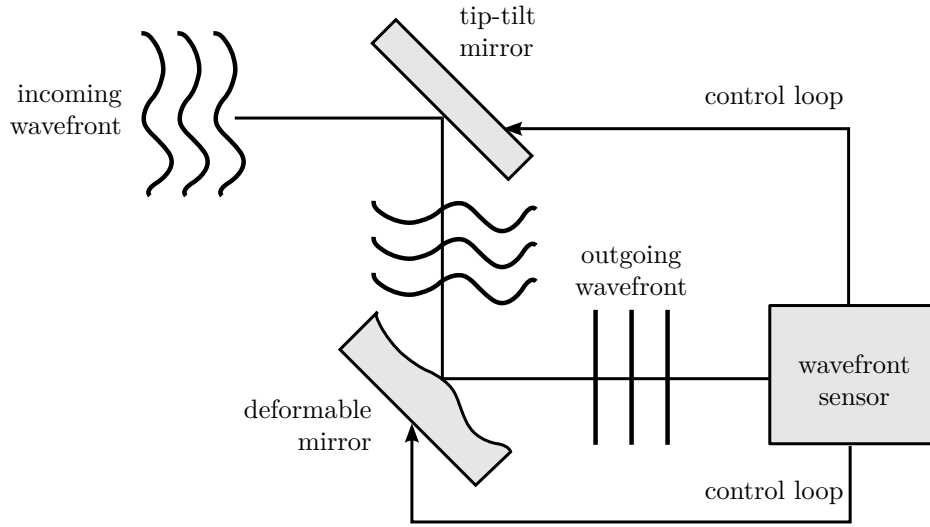
Figure 4.1: Schematic of a typical AO system in closed loop configuration. A wavefront sensor measures the phase distortion and a control loop steers a tip-tilt and deformable mirror.

thus restricted to low altitudes where the phase distortions have not developed into intensity distortions. In Ref. [13], which is part of the work performed for this thesis, an adaptive optics testbed for pre- and post-compensation of the uplink and downlink in the application of Earth-to-satellite optical communication was presented. In this thesis, however, only results obtained with a post-compensation approach are presented. Next, the individual elements of the AO system are discussed in more detail.

As can be understood from the discussion above, the correction of the beam can only be as good as the measurement of the phase. Many different wavefront sensor schemes exist, e.g. the pyramid wavefront sensor, curvature sensor, lateral shear interferometer and Shack-Hartmann sensor, to name but a few. In this thesis, the Shack-Hartmann sensor type is considered which consists of a lenslet array and a camera. To explain its working principle, first consider how a single lens can be used to measure the angle of incidence of light. A plane wave propagating along the optical axis of the lens is transformed into a focal spot on the optical axis. If the propagation direction is tilted with respect to the optical axis, it still produces a spot in the focal plane, but with a certain displacement from the optical axis as shown in Fig. 4.2. The displacement Δ and the tilt angle α are related by:

$$\tan \alpha = \frac{\Delta}{f} \, . \tag{4.3}$$

In connection with a position-sensitive device, a lens can thus be used to determine the
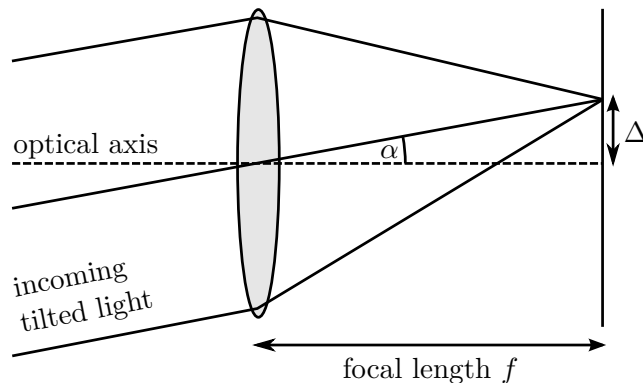
Figure 4.2: Determination of incoming wavefront angle α with an ideal lens: an incoming tilted wavefront produces a focal spot displaced by Δ from the optical axis.

tip and tilt of an incoming beam. This method is simulated in Sec. 4.3 when a tip-tilt correcting AO system is introduced.

To determine the wavefront and not only its tip and tilt, one can use an array of lenses instead of a single lens. It decomposes the incoming light into many subapertures as shown in Fig. 4.3. For a plane incoming wavefront, one observes an array of focal spots aligned with the optical axes of the lenses within the array. For a distorted wavefront, the spot displacement behind each of the lenses can be used to sense the local wavefront slope along the lens. It should be noted that this slope only represents an average slope within the area of the microlens. Consequently, information is lost if the wavefront varies on a smaller scale than the size of the microlens. From evaluating all spot displacements, an array of x- and y-slopes of the incoming wavefront is obtained. By integrating these slopes, one can reconstruct the wavefront $\phi(\mathbf{r})$ with a resolution determined by the properties of the lenslet array, the pixel size and the signal-to-noise ratio of the camera. The Shack-Hartmann sensor is modeled in the simulation of a realistic AO to determine the wavefront correction, as described in Sec. 4.4.

To introduce the required wavefront correction, one can employ deformable and tip-tilt mirrors. Tip-tilt mirrors only have two degrees of freedom – tip and tilt. This low number of actuators allows for a fast control and a large deflection. Deformable mirrors usually correct for a much larger number of degrees of freedom. For instance, unimorph deformable mirrors consist of a mirror substrate with several actuators attached to it. These actuators deform the mirror's surface by applying a signal, e.g. a voltage.

Before operating an adaptive optics system, it is crucial to determine how the corrective elements respond to the applied voltages. To this end, one records a so-called
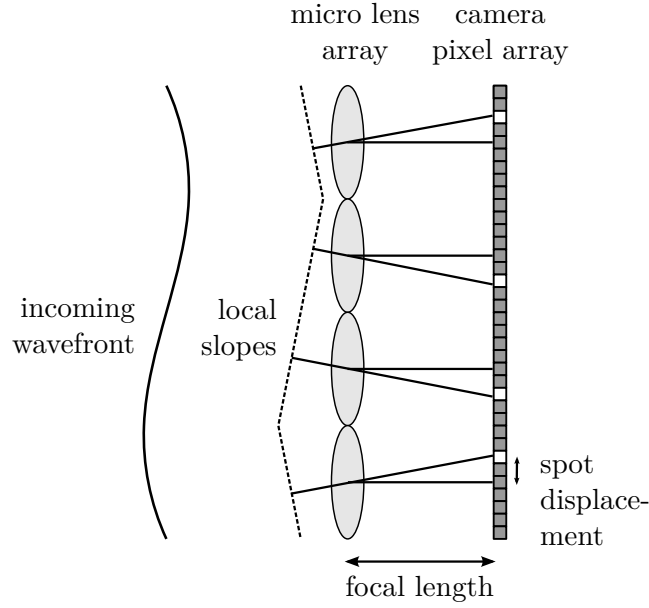
Figure 4.3: Working principle of a Shack-Hartmann sensor: a micro lens array decomposes the incoming field into several subapertures. Behind the micro lens array, an array of focal spots is recorded by a camera. The displacement of the spots is proportional to the local slope of the incoming wavefront.

actuator influence function by subsequently applying a certain reference voltage to the individual actuators and recording the deformation, e.g. with a wavefront sensor. It should be noted that there are two underlying assumptions in the following discussion. First, the deformable mirror deformation is assumed to scale linearly with the voltage. Second, the deformable mirror surface is a linear combination of the single actuator deflections when several actuators are activated at the same time. This linear relationship can be expressed by a matrix relation between the voltages applied to the mirror actuators $\mathbf{v}$ and the according wavefront slopes $\mathbf{s}$ measured by the wavefront sensor

$$\mathbf{s} = A\mathbf{v} \,, \tag{4.4}$$

where A is the actuator influence matrix. In fact, to determine the required voltage signal for the mirror to correct for a wavefront distortion, one needs the reversed relation; namely, which voltages need to be applied to achieve a certain wavefront slope. To this end, one calculates the pseudoinverse of the actuator influence matrix A using a singular value decomposition to obtain the transfer matrix T

$$\mathbf{v} = T\mathbf{s} \,. \tag{4.5}$$

49

correction up to	σ^2
piston	$\sigma_1^2 = 1.03 \left(\frac{D}{r_0} \right)^{5/3}$
tip	$\sigma_2^2 = 0.582 \left(\frac{D}{r_0} \right)^{5/3}$
tilt	$\sigma_3^2 = 0.134 \left(\frac{D}{r_0} \right)^{5/3}$
defocus	$\sigma_4^2 = 0.111 \left(\frac{D}{r_0} \right)^{5/3}$
astigmatism (0°)	$\sigma_5^2 = 0.0880 \left(\frac{D}{r_0} \right)^{5/3}$
astigmatism (45°)	$\sigma_6^2 = 0.0648 \left(\frac{D}{r_0} \right)^{5/3}$
jth order (for large j)	$\sigma_j^2 = 0.2944 j^{\sqrt{3}/2} \left(\frac{D}{r_0} \right)^{5/3}$

Table 4.1: Residual wavefront error σ_j^2 after the first j Zernike polynomials have been corrected for [72].

Noll studied the decomposition of turbulence-induced phase distortions in terms of Zernike polynomials which represent a complete and orthonormal set of functions defined within the unit circle [72]. Because the lowest order polynomials represent the most common aberrations in optical systems such as defocus, astigmatism and coma, they are a popular function set in the optics community. The Zernike decomposition of turbulence distortions is of interest because it helps to estimate the importance of different order modes and roughly the numbers of degrees freedom required for a deformable mirror. In particular, Noll derived the residual wavefront error σ_j^2 after the first j Zernike polynomials are corrected for as listed in Tab. 4.1. In particular, tip and tilt constitute approximately 87% of the wavefront error. In very weak turbulence, it is therefore sufficient to correct for tip and tilt. As turbulence grows stronger, the higher-order contributions become significant and higher-order correction becomes necessary.

4.2   Idealized adaptive optics

As mentioned above, AO systems influence the phase of the received light. Ideally, an AO system would measure the incoming light's phase, with infinite precision, and apply its complex conjugate[1]. The idealized AO simulated for this thesis does exactly

---

[1]There may be cases where it is not beneficial to apply correction with such high resolution, e.g. when the light to be corrected and that to sense the wavefront (e.g. guide star in Astronomy or the beacon in optical communication) are separated by a point-ahead angle or a different beam geometry [82, 83]

that:

$$\phi_{\text{ideal}} = \arg[u_{beacon}(x, y, z = L)] \, . \tag{4.6}$$

The beacon field calculated by the split-step propagation described in Sec. 3.2 is a complex array and its phase is easily computed with the built-in function denoted by arg in Eq. (4.6).

This system is highly idealized and thus neglects many limiting factors of real AO systems, e.g., the deformable mirror fitting error caused by the finite number of actuators and the wavefront sensor fitting error caused by the finite spatial sampling and the sensor noise. In contrast to the idealized system, the realistic system accounts for these effects as will be discussed later. The temporal errors caused by delay times of the system such as sensor readout and deformable mirror response times are neglected throughout this thesis. Additionally, geometric differences between the light used for sensing – in this thesis the beacon and in astronomy the guidestar – and the signal can lead to wavefront errors. This will be partially investigated in an optimization of the beacon beam waist in Ch. 6.

4.3 Tip-tilt compensation

In contrast to the idealized AO, the tip-tilt correction represents the most basic AO system. To sense the angle of arrival of an incoming light beam, the spot displacement in the focal plane of an ideal lens can be measured as described in Sec. 4.1. In the simulation, the light incident on the receiver, obtained by the split-step propagation described in Sec. 3.2, is imaged by an ideal lens which is equivalent to a Fourier transformation with an additional phase factor [68]

$$u_{fp}(x_2, y_2) = \frac{1}{i\lambda f} e^{\frac{ik}{2f}(x_2^2 + y_2^2)} \iint u_b(x_1, y_1) e^{-\frac{2\pi i}{\lambda f}(x_2 x_1 + y_2 y_1)} \mathrm{d}x_1 \mathrm{d}y_1 \, , \tag{4.7}$$

where u_{fp} is the mode function in the focal plane and u_b the received mode function of the beacon at the receiver. Such a Fourier transform can be implemented numerically by a Fast-Fourier-Transform and leads to a fixed sampling of the input and focal plane. For the evaluation of Eq. (4.7), the code provided in Ref. [69] was used.

The displacement of the focal spot is determined by a standard center of mass

calculation

$$\Delta_x = \frac{\sum_{i,j} |u_{i,j}|^2 x_{i,j}}{\sum_{i,j} |u_{i,j}|^2} \, , \tag{4.8}$$

$$\Delta_y = \frac{\sum_{i,j} |u_{i,j}|^2 y_{i,j}}{\sum_{i,j} |u_{i,j}|^2} \, , \tag{4.9}$$

where the summation is performed over all elements of the sampled field u denoted by the indices i and j and the index fp has been dropped for the sake of clarity.

From the displacement of the focal spot and focal length of the lens f, one can calculate the angle of incidence

$$\alpha_{x/y} = \frac{\Delta_{x/y}}{f} \, , \tag{4.10}$$

for the x- and y-direction, respectively. Here, the small angle approximation of the tangent has been used, cf. Eq. (4.3). The reconstructed wavefront is then given by

$$\phi_{\mathrm{TT}}(x,y) = \frac{2\pi}{\lambda} \left(\alpha_x \, x + \alpha_y \, y \right) . \tag{4.11}$$

The scaling by $2\pi/\lambda$ is necessary to convert the tilted wavefront into a phase given as multiples of 2π. The calculation is performed over the entire computation grid which is much larger than the aperture. By that, numerical artifacts are avoided. The focal length is chosen to be ten times larger than the aperture diameter of 300 mm.

4.4 Realistic adaptive optics system

In order to simulate a realistic AO system, the characteristics of an existing AO setup developed at Fraunhofer IOF were adopted. Details of the system's design and performance can be found in Ref. [13] which is part of the work performed for this thesis. The system consists of a fast InGaAs camera combined with a 14 by 14 lenslet array, a 40 actuator deformable mirror and a tip-tilt mirror that are all connected to a real-time control computer. After a partial redesign of the system, a beam with 31 mm diameter illuminates the deformable mirror which has a 45 mm aperture [84]. The actuators are arranged in three concentric circles with eight actuators in the inner circle and 16 in the middle and outer ring. Figure 4.4 overlays the actuator layout, with a cross at the center of the actuator, and the Shack-Hartmann lenslet array denoted by the blue grid. The area of the beam is shown by the red circle. Results obtained with this system for non-OAM communication in simulated and real-world turbulence are described in Refs. [13, 80, 85].
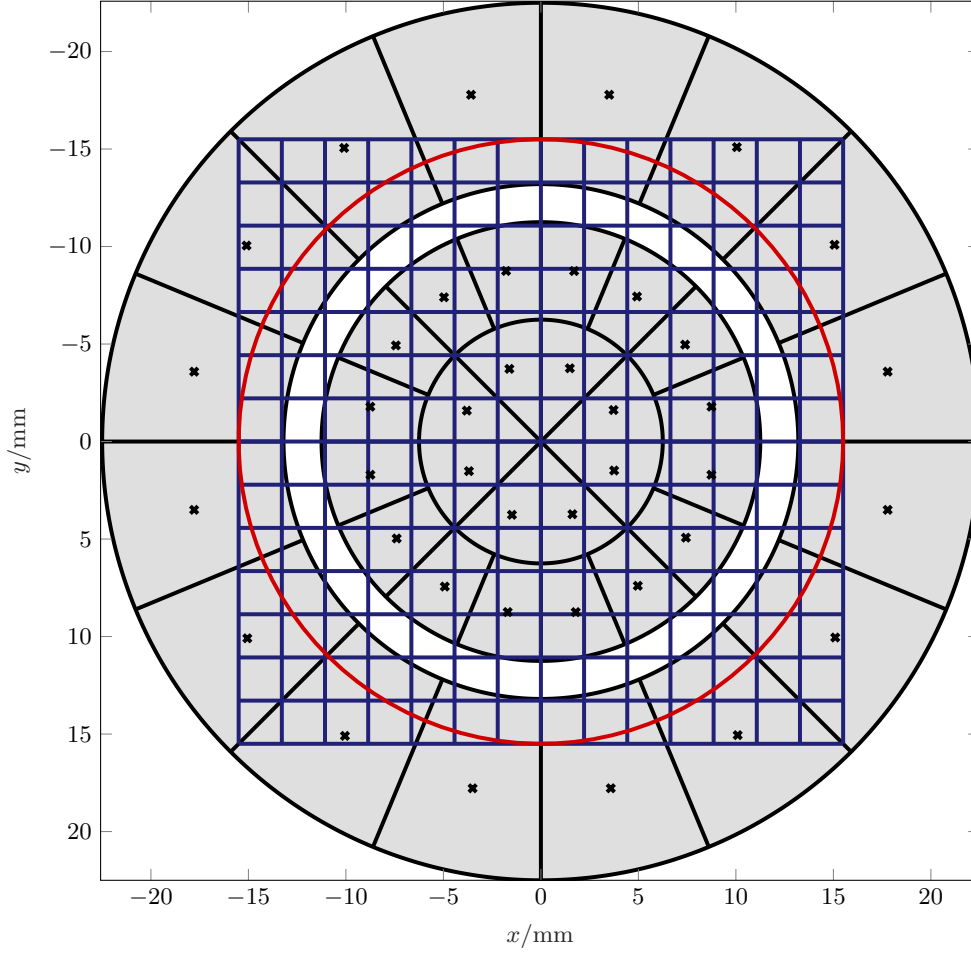
Figure 4.4: Comparison of the deformable mirror actuator pattern and the Shack-Hartmann lens array. The deformable mirror has 40 actuators arranged in three concentric rings with 8 actuators in the inner ring and 16 actuators in the middle and outer ring. The actuator areas are highlighted in gray and their centers are marked by crosses. The blue lines indicate the boundaries of the Shack-Hartmann sensor lenses and the red circle the area of the beam.

In the simulations, both the influence of the Shack-Hartmann sensor, in particular the division of the aperture into 14 by 14 lenslets, and the deformable mirror actuator influence functions are incorporated. Additionally, the lowest-order modes tip and tilt are assumed to be corrected for by the system described in Sec. 4.3.

In the following, the calculation of the realistic AO phase correction ϕ_{realAO} is detailed as schematically shown in Fig. 4.5. It consists of the following steps: wavefront slope calculation based on a Shack-Hartmann sensor, fitting of actuator voltages and calculation of the phase correction based on reconstructed and interpolated actuator influence functions. Afterwards, the tip-tilt correction is determined as in Sec. 4.3.
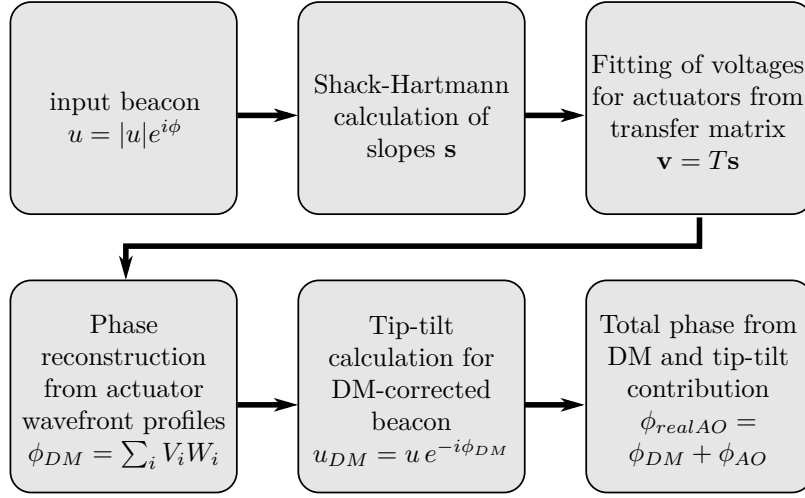
```
┌─────────────────┐   ┌─────────────────┐   ┌─────────────────┐
│                 │   │                 │   │ Fitting of      │
│  input beacon   │──▶│ Shack-Hartmann  │──▶│ voltages        │
│  u = |u|e^{iφ}  │   │ calculation of  │   │ for actuators   │
│                 │   │ slopes s        │   │ from transfer   │
│                 │   │                 │   │ matrix v = Ts   │
└─────────────────┘   └─────────────────┘   └─────────────────┘
         │                                                       
         ▼                                                       
┌─────────────────┐   ┌─────────────────┐   ┌─────────────────┐
│ Phase           │   │ Tip-tilt        │   │ Total phase     │
│ reconstruction  │   │ calculation for │   │ from DM and     │
│ from actuator   │──▶│ DM-corrected    │──▶│ tip-tilt        │
│ wavefront       │   │ beacon          │   │ contribution    │
│ profiles        │   │ u_DM = u e^{-iφ}│   │ φ_realAO =      │
│ φ_DM = Σ_i V_i W_i│ │                 │   │ φ_DM + φ_AO     │
└─────────────────┘   └─────────────────┘   └─────────────────┘
```

Figure 4.5: Overview of the realistic AO simulation routine

The Shack-Hartmann sensor modeling is based on the previous description of an ideal lens to obtain the gradient of a wavefront, see Sec. 4.3. The subapertures given by the lenslets are modeled by decomposing the beacon field into 14 by 14 subsets within the receiving telescope. The ideal lens calculation is performed for each of the subsets individually, see Eq. (4.7), and the position of the generated spots is determined by the center of mass calculation from Eqs. (4.8, 4.9). To avoid wrapping effects, the subarrays are zero-padded to a four times larger array before the calculation. As a result, one finds spot displacements both in x- and y-direction for each of the 196 lenslets which are proportional to the local wavefront slopes $\mathbf{s}$ by Eq. (4.10).

Intuitively, one would expect this calculation to be slow as it is repeated 196 times. Fortunately, it is performed on the area of the subaperture which is 1/14th of the entire aperture. In addition, only those micro lenses which receive enough light are considered in the calculation. To this end, a threshold to the total intensity received within a micro lens aperture is introduced. This step is also performed in experiments to discard spots that receive little light. If the received intensity is too low within one micro lens, the signal-to-noise ratio decreases, leading to large errors on the measured centroids. This could induce instabilities in the AO control loop which is prevented by introducing the threshold. Spots below this threshold are discarded in the calculation – both in the experiment and in the simulations presented here. In particular, a threshold corresponding to 1% of the intensity received at the micro lens with the brightest spot is applied.

In the next step, one needs to connect the wavefront slopes to the deformable mirror deflection which is given by the actuator influence function introduced earlier in Sec. 4.1. To determine the actuator influence function, the deformable mirror actuators are activated one after the other and the wavefront slopes are measured by the Shack-Hartmann sensor. By performing a singular value decomposition, the actuator influence function is decomposed into orthogonal modes. This modal actuator influence function is inverted to obtain the transfer matrix T. The required voltages at the actuators are obtained from a matrix multiplication of the transfer matrix and the slope vector, see also Eq. (4.5). For the simulations, the transfer matrix was constructed from an actuator influence function measured with the existing AO system at Fraunhofer IOF. With this AO system, the slope vector $\mathbf{s}$ has 14 by 14 entries both in x- and y-direction which leads to a total of 392 entries while the voltage is a vector with 40 entries – one for each actuator. Consequently, the transfer matrix is a 40 by 392 matrix. Because of the applied threshold, a certain number of spots is discarded. In the calculation, this is incorporated by selecting those slope and transfer matrix entries associated with lenses receiving an intensity above the threshold.

After the voltages at the actuators have been found, one still needs to calculate the phase correction which is achieved by the according mirror deformation. Remember that the actuator influence function gives the slopes of the wavefront after activating the mirror actuators. The wavefront profiles are reconstructed from the slopes (i.e. the wavefront gradient) by the zonal algorithm from Ref. [86] implemented by Herbert Gross. Since the resulting wavefront is sampled on the 14 by 14 grid of the lenslet array, it was fitted to the numerical grid of the optical fields resulting in a matrix W_i of 256 by 256 for the ith actuator. For this fit, the function `gridfit` from the MATLAB Central File Exchange [87] was used. The correction of the deformable mirror is a linear combination of the applied voltages at each actuator and the respective wavefront profiles:

$$\phi_{\mathrm{DM}} = \sum_{i=1}^{40} v_i W_i \,. \tag{4.12}$$

Next, the tip-tilt phase correction ϕ_{TT} is calculated from the beacon field corrected by the deformable mirror $u_b \exp(-i\phi_{DM})$ as described in Sec. 4.3. This corresponds to a closed-loop system where the tip-tilt sensing device is placed after reflection by the deformable mirror. The final realistic AO correction is a sum of the higher-order DM

and the lower-order tip-tilt correction

$$\phi_{realAO} = \phi_{DM} + \phi_{TT} \, . \tag{4.13}$$

The approach of separating tip and tilt from the higher-order aberrations is applied in many AO systems In fact, tip and tilt are the modes with the highest contribution to the wavefront error in atmospheric turbulence [72], see also Tab. 4.1, meaning that they also require the highest stroke. Since the tip-tilt component would reduce the available deflection of the deformable mirror for the higher-order modes, both a deformable mirror and a tip-tilt mirror are included. This separation is implicitly included in the actuator influence functions by subtracting the average centroid displacement along the aperture beforehand.

Please note that this model of a realistic AO does not include all limitations of such a system. In particular, the pixelation of the Shack-Hartmann sensor camera is not included. This can have a considerable effect which should already be considered in the design of the system, see also Ref. [13]. The camera also experiences noise which leads to variations of the centroid position, in particular at low intensities. This effect is only implicitly considered by the intensity threshold for weakly illuminated micro lenses. Last but not least it should be mentioned that this simulation does not take any temporal effects into account. These arise from limited exposure and readout times of the camera, the computation time to determine the required voltages and the time the deformable mirror needs to adjust to a new position. These delay times need to be smaller than the time scale at which the turbulence distortions change. Such a consideration was performed in the design of the system to, e.g., determine the number of Shack-Hartmann microlenses and the required readout time of the camera.

4.5   Comparison of adaptive optics compensation models

In order to compare the different AO models presented above, an analysis of the point-spread function and the power spectral density with and without correction was performed. In addition, the Strehl ratio was calculated for different turbulence strengths.

To this end, a simplified simulation was performed which includes phase distortions but neglects the intensity distortions developing in longer propagation. With the method described in Sec. 3.2, random phase screens with the size of the receiving aperture of 300 mm were generated. The circular pupil was homogeneously illuminated (1 within the aperture, 0 outside the aperture) and the phase screens were added by multiplying with $\exp(i\phi)$. The three different AO algorithms presented in Secs. 4.2 to 4.4
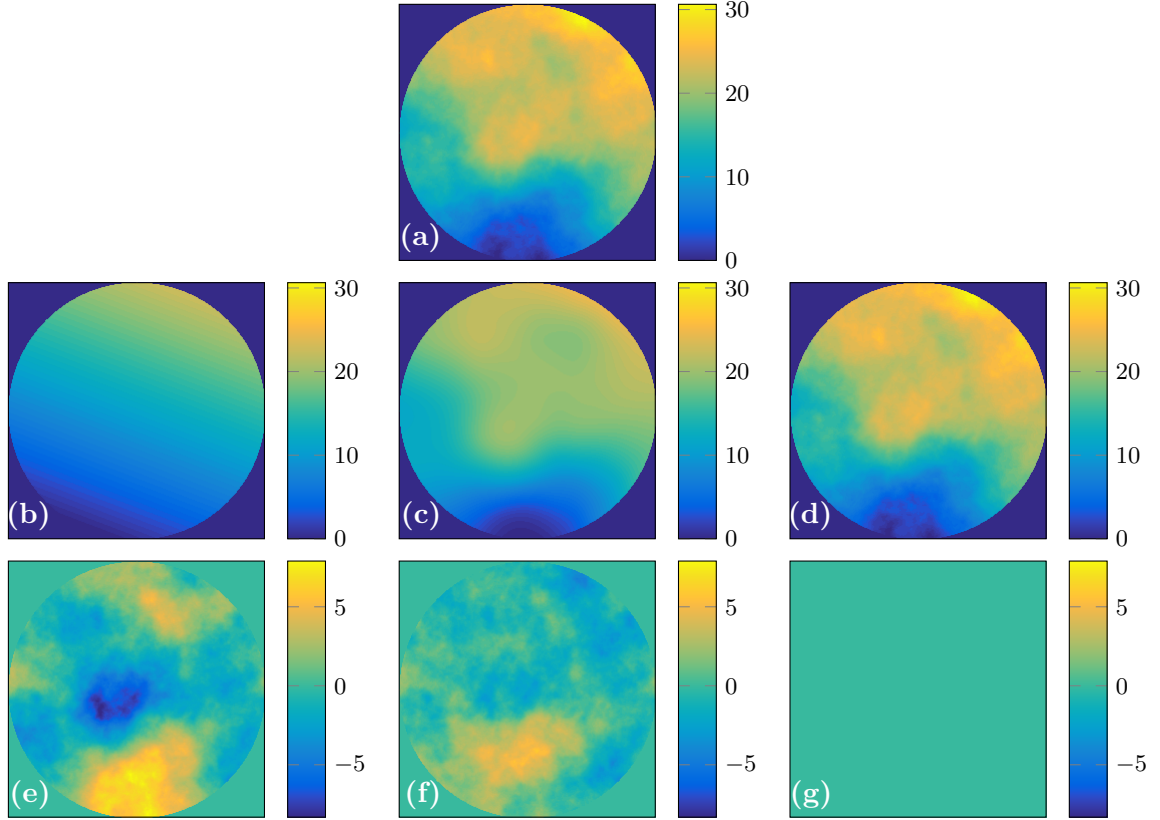
Figure 4.6: Example of adaptive optics fitting of the input random phase screen shown in (a). The false color plots denote the phase in radian. The second row (b-d) depicts the calculated AO correction while the third row (e-g) plots the difference between AO correction and initial distortion for (b,e) tip-tilt, (c,f) realistic, and (d,g) idealized AO.

were applied to this incoming phase-distorted light. As a first visualization, Fig. 4.6 depicts an example of the resulting wavefront profiles and the residual wavefront error. The topmost plot (a) represents the input phase distribution coming from the random phase screen. The second row of plots (b-d) shows the phase profile corrected by the different AO schemes – (b) tip-tilt AO, (c) realistic AO and (d) idealized AO. As expected, the tip-tilt AO only corrects for the general tip and tilt of the incoming wavefront while the realistic AO resembles the input phase much more. However, it is not able to correct for the small scale distortions which lie below the resolution of the 14 by 14 wavefront sensor array and the 40 actuator deformable mirror. The idealized AO, by definition, can completely reconstruct the incoming wavefront. These observations become more evident from the third row of plots (e-g) which show the residual phase distortion after correction, i.e. the difference between AO correction and the input phase distortion – for (e) tip-tilt AO, (f) realistic AO and (g) idealized AO.

After this example, a quantitative evaluation of AO efficiency is performed. To separate the effects of the wavefront sensor and the deformable mirror, the realistic AO scheme is further subdivided. The wavefront sensor scheme uses the calculation of the wavefront slopes of a Shack-Hartmann sensor as described in Sec. 4.4 but does not consider the mirror capabilities. Instead, a zonal algorithm reconstructs the wavefront on the 14×14 grid given by the geometry of the micro lens array [86]. Afterwards, the wavefront is interpolated to the 256×256 calculation grid [87]. A subsequent tip-tilt calculation corrects for the low-frequency distortions. By this procedure, the wavefront sensor capabilities can be assessed individually from the rest of the AO system. The deformable mirror scheme uses the reconstructed wavefront profiles on the 256×256 calculation grid which were obtained from the actuator influence function. To this end, a least-squares fit is performed by a singular value decomposition. Again, the tip-tilt correction is applied subsequently. In total, five different AO schemes can be compared – no correction, tip-tilt, realistic, deformable mirror and wavefront sensor AO.

In the literature, see e.g. Refs. [88–91], an investigation of the system performance is typically performed in the design phase of an adaptive optics system. Then, the local turbulence conditions, telescope parameters and optical quality requirements are analyzed to determine the number of Shack-Hartmann micro lenses and deformable mirror actuators. The required optical quality is often specified by the point-spread function. In the diffraction-limited case, the image of a telescope is a convolution of the object and the point-spread function and thus the point-spread function is closely connected to the resolution of the system. In astronomy, requirements on the point-spread function would be determined from the objects to be investigated. The point-spread function can be calculated from the Fraunhofer diffraction pattern of the pupil function P which is equal to 1 inside the aperture and 0 otherwise [68]. In a turbulence-distorted system, the pupil function needs to be modified by the residual wavefront error [68, 88]

$$\mathcal{P}(x,y) = P(x,y) \exp(i\phi(x,y)), \qquad (4.14)$$

where $P(x,y)$ is the undistorted pupil function and $\phi(x,y)$ is the phase distortion. Hence, the point-spread function h is given by [68]

$$h(x,y) = \mathcal{F}[\mathcal{P}(x,y)]. \qquad (4.15)$$

Typically, the intensity of the point-spread function $|h(x,y)|^2$ is measured in a real system. While one is usually interested in the final point-spread function of the system,

it is hard to derive analytical formulations of the AO compensation models. In fact, it is possible to define such a function for the inverse Fourier transform of the intensity point-spread function $|h(x, y)|^2$, the so-called optical transfer function $\mathcal{H}$ [68]

$$\mathcal{H}(f_x, f_y) = \mathcal{F}^{-1}[|h(x, y)|^2].$$ (4.16)

While in the spatial domain, an image is formed by convolution of the point-spread function and the object, in the frequency domain it is a product of the optical transfer function and the object's spectrum. This assumption also holds for an AO-corrected telescope. While one needs an end-to-end simulation of the AO system and the telescope to determine the point-spread function directly, it is possible to separate the contributions of the AO and the telescope in the optical transfer function [90]

$$\mathcal{H}_{total}(f_x, f_y) = \mathcal{H}_{AO}(f_x, f_y)\mathcal{H}_{tel}(f_x, f_y),$$ (4.17)

which is similar to the result for an incoherent imaging system. The optical transfer function can be determined from the spectra of the residual phase of the individual adaptive optics components [90]. Hence, the point-spread function of the AO system can be estimated by a product of functions in frequency space and a subsequent Fourier transform

$$|h(x, y)|^2 = \mathcal{F}[\mathcal{H}_{total}(f_x, f_y)].$$ (4.18)

In this thesis, the situation is slightly different. The AO system has already been built and its capabilities should be assessed. In addition, it is not possible to separate the effects of the aperture and the AO system since the AO response is only defined within the area of the aperture. Hence, the order of the calculation is reversed as to the descriptions above – first the point-spread function is calculated from the generalized pupil function and then the optical transfer function is calculated. To obtain the generalized pupil function $\mathcal{P}$, multiple realizations of atmospheric turbulence and the AO system's response are calculated. The phase in Eq. (4.14) is the residual phase after the application of the different AO schemes (or no correction), see Fig. 4.6 (e-g). For each realization of turbulence, the intensity point-spread function $|h(x, y)|^2$ is calculated and averaged over 1000 realizations.

The resulting point-spread functions are shown in Fig. 4.7 on a double-logarithmic scale for $D/r_0 = 10$. The black curve represents the diffraction-limited performance of a telescope with a circular aperture diameter of 300 mm. It has a central peak and side lobes for large distances from the center. This curve agrees with the known analytical
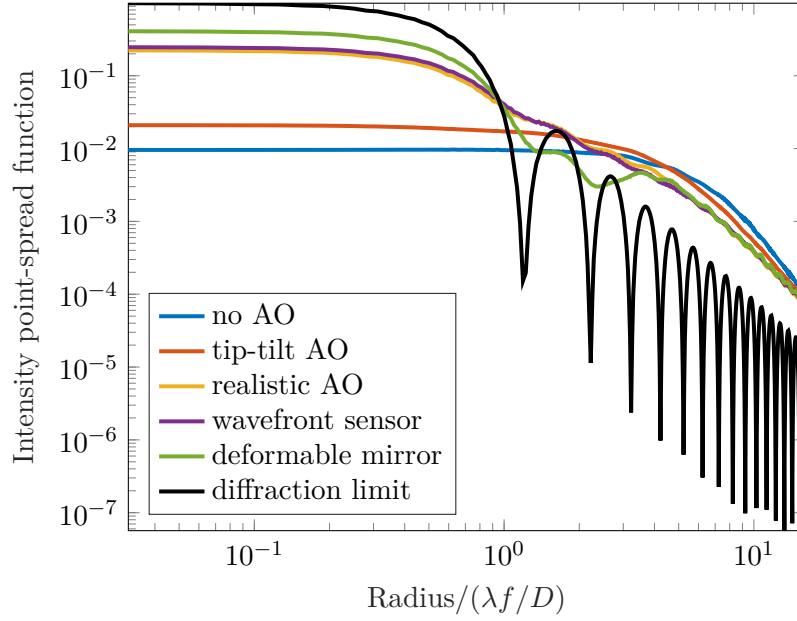
Figure 4.7: Point-spread function for different degrees of correction for $D/r_0 = 10$. Different degrees of AO correction are compared as indicated by the legend. Please note the double-logarithmic scaling of the figure.

result which is an Airy function. The blue curve shows the turbulence-distorted result which is much broader than the diffraction-limited one. When turbulence effects become strong, i.e. $D/r_0 \gg 1$, the minimum achievable spot size is no longer determined by the telescope aperture D but rather by the Fried parameter r_0. This also means that objects cannot be resolved as well as in the diffraction-limited case. By applying AO correction, this effect can be partially reversed. The tip-tilt correction (red line) improves the point-spread function and realistic AO (yellow line) improves it even more. As mentioned above, the wavefront sensor and deformable mirror contributions were simulated separately to provide more details on the systems's limitations. It can be seen that the green deformable mirror curve follows the diffraction-limited curve best. The purple curve of the Shack-Hartmann sensor performs worse indicating that the Shack-Hartmann sensor is the limiting element in the AO system. Similar observations can be made for the optical transfer function which is discussed in App. B.

In order to understand the contributions of certain spatial frequencies to the system performance, the power spectral density Φ of the residual wavefront is analyzed [92]

$$\Phi(\kappa) = |\mathcal{F}[\phi]|^2 . \tag{4.19}$$

Atmospheric turbulence is often described in terms of the power spectral density, re-

call for example the Kolmogorov spectrum introduced in Sec. 3.1. Figure 4.8 displays the power spectral density for the various AO schemes on a double-logarithmic scale calculated for $D/r_0 = 10$. The maximum frequencies that the deformable mirror and the wavefront sensor can correct for, $f_{\mathrm{max,DM}}$ and $f_{\mathrm{max,WFS}}$, respectively, are indicated by the black dashed lines. For the wavefront sensor, the frequency $f_{\mathrm{max,WFS}} = 1/(2D_{\mathrm{ML}}) = 7/D$ is easily calculated from the distance between the microlenses D_{ML} by the Nyquist criterion. For the deformable mirror, this frequency is obtained by calculating the distance between each actuator and its nearest neighbor. An average is performed to obtain the characteristic distance between actuators D_{act} and thus $f_{\mathrm{max,DM}} = 1/(2D_{act}) \approx 3.2/D$. While for the deformable mirror the influence of the limiting frequency can be observed in the curve, it is more subtle for the wavefront sensor where a transition to a power-law behavior begins. As can be seen in Fig. 4.8, the deformable mirror achieves the lowest residual error for frequencies below its characteristic frequency. Between the deformable mirror and wavefront sensor frequencies, the wavefront sensor and the deformable mirror perform equally well. For large frequencies, the deformable mirror, wavefront sensor and realistic AO scheme follow the same power law which appears linear in the double-logarithmic plot. The tip-tilt correction outperforms the case without AO only for small frequencies as expected. The case without AO increases less with increasing frequency as would be expected from the Kolmogorov spectrum. This could be caused by the limitation of the phase screen generation routine which, still, underrepresents low frequencies. Overall, one can conclude that the difference between the deformable mirror and wavefront sensor scheme is mostly caused by the evolution in the frequency range below $f_{\mathrm{max,DM}}$.

A very popular quantity to evaluate AO system performance is the Strehl ratio. It is defined as the ratio of the point-spread function at the energy centroid divided by the diffraction-limited point-spread function at the energy centroid, which coincides with the origin in both cases. Figure 4.9 plots the Strehl ratio versus the turbulence strength given by the telescope diameter D divided by the Fried parameter r_0. As expected, all curves decay with increasing turbulence. Without correction, the decay is fastest. Tip-tilt correction can delay the reduction of the Strehl ratio. The realistic AO system can considerably increase the Strehl ratio. From the decay of its individual components, the wavefront sensor and the deformable mirror, one can see that the Shack-Hartmann sensor limits the performance as has already been noted above.
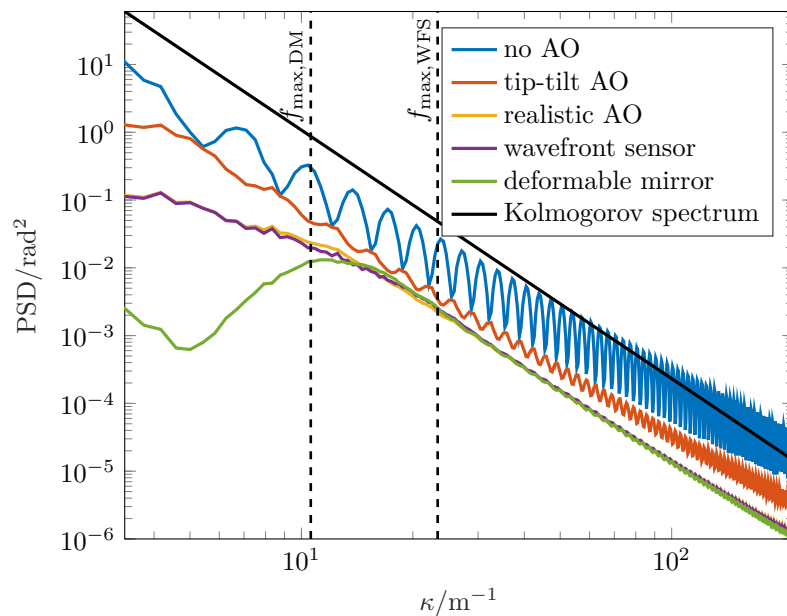
Figure 4.8: Power spectral density (PSD) of AO-corrected turbulence distortions with $D/r_0 = 10$. The higher the degree of AO correction, the lower is the power of turbulence distortions. The black dashed lines indicate the important frequencies of the realistic AO system given by the deformable mirror $f_{\mathrm{max,DM}}$ and the wavefront sensor $f_{\mathrm{max,WFS}}$.
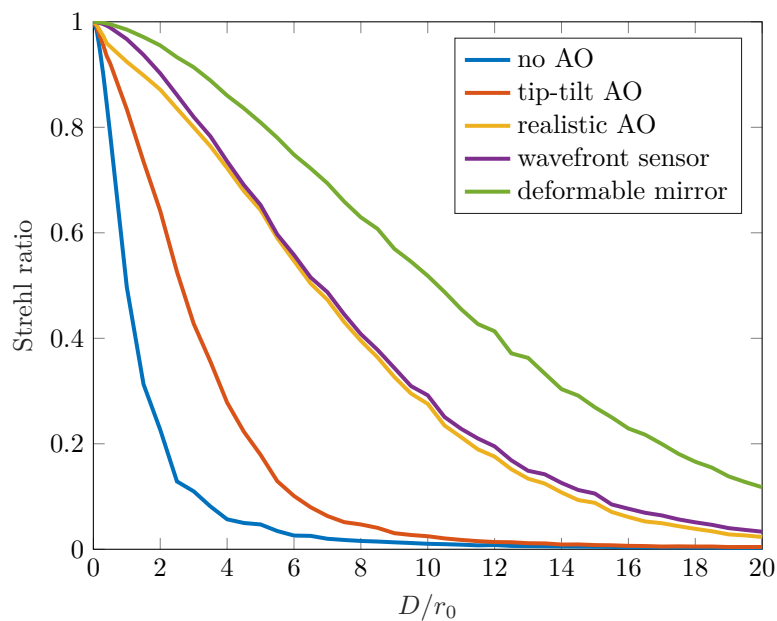

Figure 4.9: Strehl ratio for different values of D/r_0 for different degrees of correction.

4.6 Layout of the simulation routine

The methods described in Sec. 3.2 and Secs. 4.2 to 4.4 were combined into a simulation routine with the parameters from Sec. 3.3. The goal of the simulations performed for this thesis is the evaluation of adaptive optics compensation for light carrying orbital angular momentum. A block diagram of this routine is shown in Fig. 4.10. A Gaussian beacon is used to perform wavefront measurements needed for the AO correction. To this end, the beacon propagates through atmospheric turbulence with the split-step propagation algorithm described in Sec. 3.2. It consists of alternating vacuum propagations and the application of a turbulent phase screen. In total, the beam is distorted by 12 such phase screens. After this split-step propagation, the beacon reaches the receiver plane where a circular aperture of 300 mm is applied to it. From the beacon field, the three AO phase corrections, for tip-tilt, realistic and idealized AO, are calculated as described in Secs. 4.2 to 4.4.

The OAM signal is then propagated through turbulence, with the same phase screens as the beacon experienced. Please note that for each of the simulated modes with $p = 0$ and l running from 1 to 5, the simulation needs to be run separately. All of these modes are Laguerre-Gaussian modes with the same value of the waist equal to w_0. At the receiver, the circular aperture is applied as for the beacon. The phase corrections calculated from the beacon profile are now used to determine the effect of AO on the OAM modes. The figure of merit is the OAM mode content or the overlap between the received light and the undistorted OAM modes

$$g_{l_2,l_1} = \sum_{i,j} u_{v,l_2}^*(i,j) u_{t,l_1}(i,j) \exp(-i\phi_{AO}(i,j)), \qquad (4.20)$$

where u_{t,l_1} is the initial mode with $l = l_1$ propagated through turbulence and u_{v,l_2}^* is the complex conjugate of the vacuum-propagated field with $l = l_2$. This calculation is repeated for different configurations of ϕ_{AO} – the tip-tilt, realistic and idealized AO obtained from the beacon calculation. To compare these results to the uncorrected case, the calculation is also performed once with $\phi_{AO}(i,j) = 0$. It is assumed that both modes are normalized such that $|g_{l_2,l_1}|^2$ returns the probability to measure an OAM with value l_2 when the transmitted mode was l_1. All other quantities considered later in this thesis can be calculated from g_{l_2,l_1}. Finally, it should be stressed that for each value of the turbulence strength w_0/r_0, the simulation is repeated 1000 times to obtain a proper number of ensemble elements of the turbulent medium.
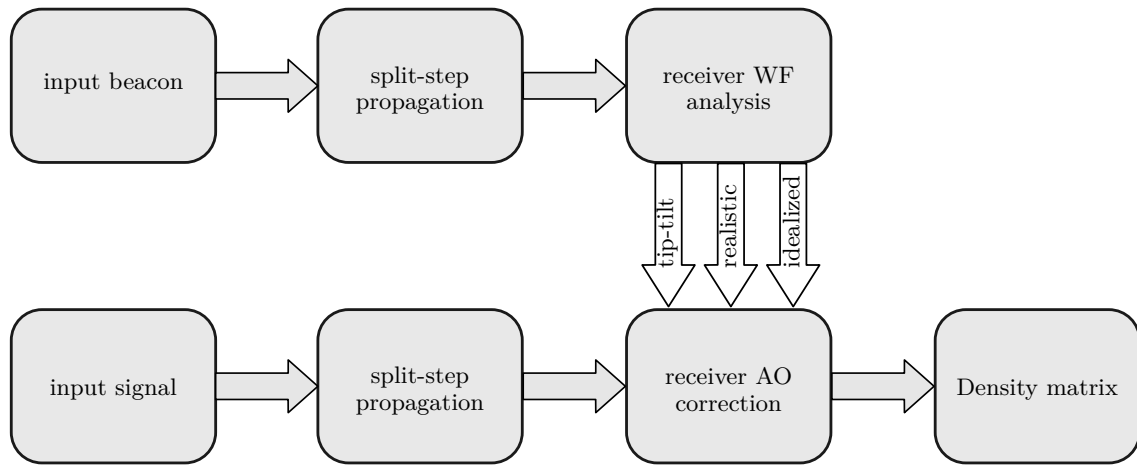
Figure 4.10: Block diagram of the simulation routine

Chapter 5

Adaptive optics restoration of orbital angular momentum photons

While adaptive optics for OAM encoding has been investigated in the context of classical communication [11, 12, 52], Ref. [28], which is part of the work in this thesis, is the first in applying it to quantum communication. This chapter is based on the results found in Ref. [28] and investigates the efficiency of adaptive optics correction on an OAM-encoded quantum key distribution protocol.

In Sec. 5.1, the existing formal description of OAM-entangled photons in turbulence [14] is extended to also account for the effect of the adaptive optics. In addition, the previously described simulation routine for atmospheric propagation, see Sec. 3.2, and the adaptive optics simulation from Secs. 4.2 to 4.4 are connected to the final state density matrix. With that, the concurrence, trace, quantum bit error rate and Bell parameter can be obtained. Section 5.2 compares the effect of different AO schemes on the concurrence and trace of an OAM-entangled state distorted by atmospheric turbulence. In Sec. 5.3, the security of the quantum key distribution protocol is evaluated in terms of the quantum bit error rate and the Bell parameter. Finally, Sec. 5.4 discusses the limitations of a phase-only AO system and Sec. 5.5 compares the obtained theoretical results to experiments from the literature.

5.1 Formal description of entangled two-qubit states

The following theoretical description of both the action of atmospheric turbulence and adaptive optics on a maximally entangled two-photon state is the basis of all results
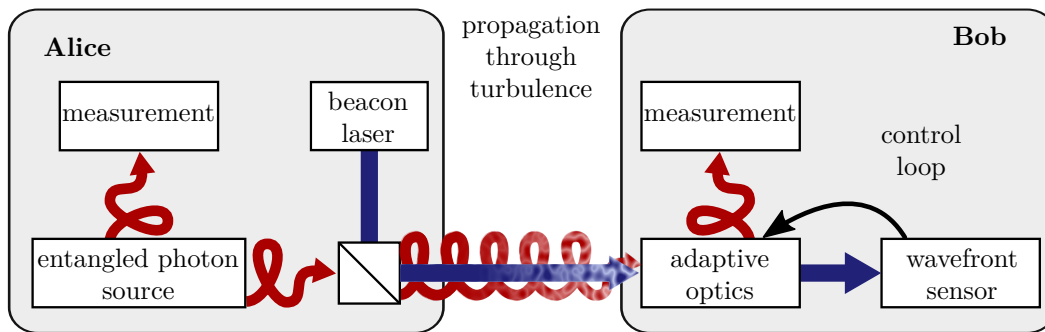
Figure 5.1: Sketch of the considered scenario: Alice and Bob want to create a secret key for secure communication via quantum key distribution. An entangled photon source at Alice's transmitter generates an OAM-entangled photon pair (red curly arrows). The first photon remains in Alice's laboratory. The second photon is sent to Bob through an atmospheric channel which distorts it. The beacon laser beam (blue straight arrow) is sent through the same channel such that an adaptive optics system at Bob's receiver can measure the phase distortions and correct the OAM photon's wavefront. Based on Fig. 1 in Ref. [28].

presented in this and the following chapter. It represents an extended version of Sec. II and Appendix A of Ref. [28] with a slightly adapted notation. The simulated setup is the quantum key distribution between two parties, typically called Alice and Bob, as depicted in Fig. 5.1. This setup is very similar to the E91 protocol which is one but by far not the only possible implementation of quantum key distribution, see also Sec. 2.2. Key to the protocol is the quantum state containing two entangled photonic qubits prepared in Alice's laboratory. One of the photons remains there, henceforth called the first photon, and the second photon is sent to Bob via the atmospheric free-space channel. Distortions within this channel affect only the second photon and lead to crosstalk with other OAM modes. Thus, Bob's received photon is transformed in a way which could impair the communication protocol – either rendering it insecure or reducing the key rate. To counter-act this effect, there is an adaptive optics system at Bob's receiver. It corrects the phase of the received photons based on measurements of an auxiliary classical light beam, the beacon, which is sent in addition to the quantum signal. It should propagate simultaneously and along the same path as the quantum signal and, therefore, needs to be separated from it e.g. by polarization or wavelength. Technical details of this separation procedure and thus influences on the quantum signal are however not considered in this thesis since they depend on the experimental implementation.

The initial state prepared by Alice contains photons in Laguerre-Gauss modes with azimuthal quantum number $+l$ for the first photon and $-l$ for the second photon and

vice versa. In the remainder of this thesis, the radial index is assumed to vanish, i.e. $p = 0$, and thus left out in the notation. The single photon state is denoted by $| \pm l \rangle$. The entangled two-photon state takes the form:

$$|\Psi_0\rangle = \frac{1}{\sqrt{2}} \left(| - l, l \rangle + | l, -l \rangle \right) . \tag{5.1}$$

Such a state could be generated by a spontaneous parametric downconversion process from a pump beam containing no OAM [57].

As already discussed, only Bob's photon undergoes the distortion by atmospheric turbulence. Since atmospheric turbulence conserves the total number of photons, but rather changes the modal decomposition of the photon, it can be described by a unitary operator U_T [93]. Please note that this operator is different for each realization of turbulence and propagation parameters. Assuming that Alice's laboratory setup does not change the first photon's state, the action of atmospheric turbulence is given by a tensor product of the identity operator acting on the first photon and the unitary operator U_T acting on the second photon. The two-photon state after propagation is thus given by

$$|\Psi_T\rangle = (\mathbb{1} \otimes U_T)|\Psi_0\rangle . \tag{5.2}$$

Similar to the action of weak atmospheric turbulence, the adaptive optics system introduces a phase-only modification of the second photon and can be represented by a unitary operator U_{AO}. To be more precise, the turbulence unitary matrix transforms the single mode input OAM state into a superposition of many, if not all, OAM states. Geometrically, this could be interpreted as a rotation of the OAM mode space. The goal of the unitary operator U_{AO} is to reverse this rotation by applying its inverse transform. However, U_{AO} can only perform a transformation of the phase of the photon's mode function. In contrast, U_T introduces not only phase but also intensity transformations while maintaining the total number of photons. Thus, it is expected that AO compensation may not always be able to reverse all effects of the turbulence distortion.

Again, U_{AO} depends on the realization of turbulence and in addition on the AO system itself. The final state after correction of the AO system reads

$$|\Psi_{AO}\rangle = (\mathbb{1} \otimes U_{AO}U_T)|\Psi_0\rangle . \tag{5.3}$$

Please note that local unitary operations cannot influence the entanglement of a quantum state [94, 95]. At this stage of the calculation, the final state is still maximally entangled although it has been transformed.

Next, it is assumed that Alice and Bob only measure the contributions to the initially encoded states $|\pm l\rangle$ but not to any other OAM states. In contrast to many analytical calculations [60, 96], only states with vanishing radial index $p = 0$ are considered. It should be clear that a measurement over the entire infinite-dimensional OAM basis is technically impossible and a restriction of the number of measured states is always necessary. While it may seem drastic to only measure two of those states, this is exactly the same number of states as would be measured in the two-dimensional polarization basis which can also be used for this quantum key distribution protocol. This restriction, or mathematically speaking truncation of the Hilbert space, can be formally described by a projection operator to the $|\pm l\rangle$ subspace acting on the second photon (since the first photon already is in the $|\pm l\rangle$ qubit subspace)

$$\Pi = \mathbb{1} \otimes (|-l\rangle\langle -l| + |+l\rangle\langle +l|) \, . \tag{5.4}$$

The final state after accounting for atmospheric turbulence, adaptive optics correction and the truncation is given by

$$|\Psi\rangle = (\mathbb{1} \otimes \Pi \, U_{AO} U_T)|\Psi_0\rangle \, . \tag{5.5}$$

Due to the projection in Eq. (5.5), the final state can have a different entanglement than the initial state.

Because of the projection defined by Eq. (5.4), only the matrix elements which lead to one of the final states $|\pm l\rangle$ need to be calculated

$$|\Psi\rangle = \sum_{l_1=\pm l} \sum_{l_2=\pm l} |l_1, l_2\rangle\langle l_1, l_2| \mathbb{1} \otimes U_{AO} U_T |\Psi_0\rangle \, . \tag{5.6}$$

To evaluate this final state, one needs to insert the initial state $|\Psi_0\rangle$ from Eq. (5.1)

$$\begin{aligned}
|\Psi\rangle = \frac{1}{\sqrt{2}} \big(&\langle -l|U_{AO}U_T|l\rangle|-l, -l\rangle + \langle l|U_{AO}U_T|l\rangle|-l, l\rangle \\
+ &\langle -l|U_{AO}U_T|-l\rangle|l, -l\rangle + \langle l|U_{AO}U_{turb}|-l\rangle|l, l\rangle \big) \, .
\end{aligned} \tag{5.7}$$

For the sake of clarity, the following short-hand notation for the single-photon matrix elements is introduced

$$g_{-l,-l} := \langle -l|U_{AO}U_T|-l\rangle \, , \tag{5.8}$$

$$g_{l,l} := \langle l|U_{AO}U_T|l\rangle \, , \tag{5.9}$$

$$g_{-l,l} := \langle -l|U_{AO}U_T|l\rangle \, , \tag{5.10}$$

$$g_{l,-l} := \langle l|U_{AO}U_T|-l\rangle \, , \tag{5.11}$$

where the first index corresponds to the final state and the second index to the initial state. Equations (5.8) and (5.9) refer to the coefficients of remaining in the initial state while Eqs. (5.10) and (5.11) describe a change of the state. Consequently, the initial state given in Eq. (5.1) is transformed into the following final state:

$$|\Psi\rangle = \frac{1}{\sqrt{2}} \begin{pmatrix} g_{-l,l} \\ g_{l,l} \\ g_{-l,-l} \\ g_{l,-l} \end{pmatrix}, \tag{5.12}$$

where a vector notation in the basis $\{|-l,-l\rangle, |-l,l\rangle, |l,-l\rangle, |l,l\rangle\}$ has been chosen[1].

Typically, it is not the single realization of the turbulent medium that is of interest but rather the average effect of turbulence and adaptive optics. Therefore, an ensemble average is performed which transforms a pure state like $|\Psi\rangle$ into a mixed state. Thus, a density matrix description of the state becomes necessary:

$$\rho = |\Psi\rangle\langle\Psi| = \frac{1}{2} \begin{pmatrix} |g_{-l,l}|^2 & g_{l,l}^* g_{-l,l} & g_{-l,-l}^* g_{-l,l} & g_{l,-l}^* g_{-l,l} \\ g_{-l,l}^* g_{l,l} & |g_{l,l}|^2 & g_{-l,-l}^* g_{l,l} & g_{l,-l}^* g_{l,l} \\ g_{-l,l}^* g_{-l,-l} & g_{l,l}^* g_{-l,-l} & |g_{-l,-l}|^2 & g_{l,-l}^* g_{-l,-l} \\ g_{-l,l}^* g_{l,-l} & g_{l,l}^* g_{l,-l} & g_{-l,-l}^* g_{l,-l} & |g_{l,-l}|^2 \end{pmatrix}. \tag{5.13}$$

Now, one can perform the ensemble average of the density matrix. In the simulations, the density matrices are calculated for one set of turbulence and propagation parameters as well as AO configurations. Afterwards, an ensemble average over the density matrices given in Eq. (5.13) is performed. To distinguish between the density matrix of one realization and the ensemble-averaged one, a new symbol is introduced:

$$\bar{\rho} = \frac{1}{\mathcal{N}} \big\langle \rho \big\rangle_{\text{Ensemble}}. \tag{5.14}$$

Since the projection onto the two-qubit subspace introduces a loss of the quantum state, a re-normalization with the factor $1/\mathcal{N}$ has been added in Eq. (5.14)

$$\mathcal{N} = \big\langle \text{tr}\, \rho \big\rangle_{\text{Ensemble}}. \tag{5.15}$$

The final form of the density matrix is used in the remainder of this thesis to describe the evolution of the initial state from Eq. (5.1) in atmospheric turbulence and different degrees of adaptive optics compensation. Different quantities can be calculated from this density matrix as e.g. the concurrence which is a measure of the entanglement,

---

[1]The vector in dual space is given by $\langle\Psi| = \frac{1}{\sqrt{2}}(g_{-l,l}^* \quad g_{l,l}^* \quad g_{-l,-l}^* \quad g_{l,-l}^*)$.

the trace i.e. the number of detected photons, as well as the quantum bit error rate and the Bell parameter.

Finally, the matrix elements given in Eq. (5.1) need to be connected to the optical fields that are calculated by the numerical simulations described in Secs. 3.2 and 4.2-4.4. To calculate the involved scalar products, it is most convenient to choose the spatial coordinate representation which, in an analytical calculation, is evaluated by the integral

$$\langle\psi|\phi\rangle = \int_0^\infty \int_0^{2\pi} u_\psi^*(r,\theta,z)u_\phi(r,\theta,z)\,r\mathrm{d}r\mathrm{d}\theta\,, \tag{5.16}$$

where u_ϕ and u_ψ correspond to the classical mode functions associated with the quantum state $|\phi\rangle$ and $|\psi\rangle$, respectively. The mode functions needed to evaluate Eq. (5.1) with help of Eq. (5.16) are obtained from the numerical beam propagation described in Sec. 3.2 and already contain the propagation through atmospheric turbulence and by that U_T. The action of U_{AO} is incorporated in the mode function by multiplication with the phase correction, see Ch. 4. In the numerical calculations, this integral is replaced by a finite sum over the Cartesian computational grid, see Eq. (4.20). In comparison to computations for a classical communication scenario, one would usually only calculate the probability to remain in the initial mode equal to $|g_{l,l}|^2$. In a quantum experiment, the complex phase of the matrix elements also contains important information and is needed to construct the final state.

5.2 Concurrence and trace restoration

Finally, all the numerical tools and the theoretical framework are available and can be used to investigate the abilities of adaptive optics to improve free-space transmission of OAM-entangled two photon states. First, the effect of atmospheric turbulence and subsequent AO correction on the two-photon state is quantified, in particular, the entanglement and the trace of an initially maximally entangled two photonic qubit state. In Ref. [28] the following results and their interpretation have been published. Please note however that the simulations were repeated with adapted parameters and the plots thus correspond to a different set of data than in Ref. [28]. The biggest difference is the propagation distance of 1000 m instead of 500 m in Ref. [28]. Since the range of w_0/r_0 is approximately the same, but the distance is twice as large, scintillation is stronger. The larger scintillation range also required increasing the number of phase screens from 4 to 12, which is discussed in detail in Sec. 3.3. In addition, the realistic AO

system described in Sec. 4.4 was not included in the previous study. The beacon beam waist is chosen to be the same and is equal to $2.45w_0$ where w_0 is the OAM photon's beam waist. The OAM modes have a root-mean-square beam radius of $\sqrt{2p + l + 1}w_0$. Hence, the largest simulated OAM beam ($p = 0, l = 5$) has a radius of $\sqrt{6}w_0 \approx 2.45w_0$. By this choice, the Gaussian beacon has the same beam waist at the transmitter as the largest OAM mode under consideration. In Ch. 6, the influence of the beacon on the compensation efficiency is investigated in more detail.

As a first example, the evolution of an initial state with $l = 2$ is considered. Figure 5.2 compares the final state entanglement measured by the concurrence, see Sec. 2.2, as a function of w_0/r_0 for different degrees of AO correction encoded by the line color. At vanishing turbulence $w_0/r_0 = 0$, all lines take the maximum value of 1 and then decline gradually with increasing turbulence strength. The blue line shows the decline of concurrence in atmospheric turbulence without correction. The loss of entanglement is the fastest and after the concurrence has vanished, it does not recover again. With tip-tilt correction (red line), one observes a strong improvement of the concurrence which still declines to zero albeit at a larger value of w_0/r_0. The realistic AO preserves the concurrence better than the tip-tilt AO. With the chosen simulation parameters, the transition between weak and strong scintillation, ($\sigma_R^2 = 1$) marked by the dashed black line, occurs at $w_0/r_0 = 1.05$. The idealized AO can recover approximately 97% up to this point. For larger turbulence values, its decay increases noticeably. The
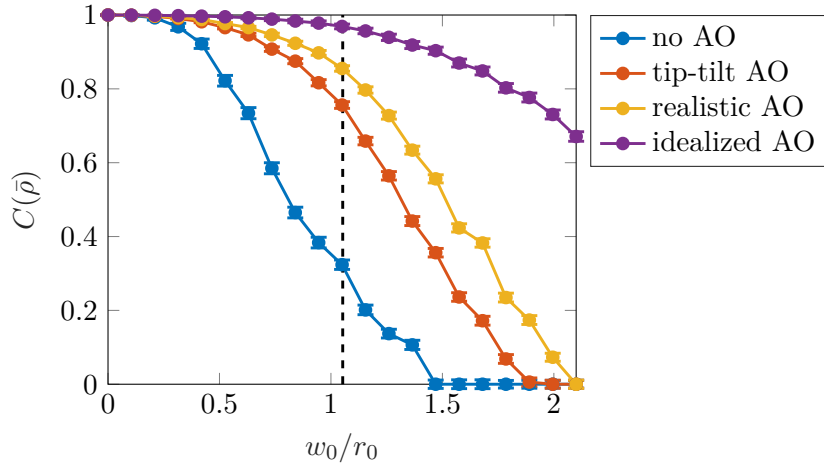

Figure 5.2: Concurrence decay of a maximally entangled two-qubit state with $l = 2$ versus turbulence parameter w_0/r_0. Each curve corresponds to a different degree of AO correction. The black dashed line indicates $\sigma_R^2 = 1$. Without correction, the concurrence is almost lost at this point.

error bars shown in the plot were calculated as described in Sec. 2.2 and represent the standard deviation of the mean, meaning that the standard deviation of the single realization is divided by $\sqrt{N}$ where N is the number of realizations. This calculation was performed in the same way for all the plots in this and the next chapter.

Next, the behavior of states with different initial OAM l is compared in Fig. 5.3. Here, different colors and plot markers encode different values of l. In Fig. 5.3(a), the entanglement decay without compensation is again shown as a function of w_0/r_0. It is known form the literature [15, 96] that in the weak turbulence case, higher-order OAM modes are more stable (without AO) and that a universal decay law of OAM entanglement can be found by the introduction of the so-called phase correlation length [60]. In addition, studies have shown theoretically and experimentally that as scintillation increases, this stability is gradually lost [62]. With the chosen simulation parameters, the stability of higher order modes is almost lost; only the $l = 1$ and $l = 2$ perform slightly worse than the other modes which mostly follow the same evolution. By applying adaptive optics, the concurrence can be increased such that it is maintained in a larger turbulence range. For tip-tilt and realistic AO, the evolution becomes mostly independent of l (although $l = 1$ performs slightly worse than the other values). For idealized compensation, one can even see a reversal of the stability such that lower-order OAM values have a slightly more stable concurrence. This trend was already visible in Ref. [28], however due to the shorter propagation distance it was on the order of the statistical fluctuations – in contrast to the new simulations. A similar observation was previously made in Ref. [77].

The next important figure of merit is the trace of the received state $\mathcal{N}$, see Eq. (5.15). In fact, it can be interpreted as the fraction of detected photons as compared to the number of transmitted photons. The trace is thus connected to the received optical power or the signal-to-noise ratio in classical communication. While the reduction of the trace does not influence the concurrence because of the renormalization in Eq. (5.14), a large fraction of lost photons may be detrimental to the quantum key distribution protocol either because it reduces the secret key rate or because the signal-to-noise ratio becomes too low.

Figure 5.4 depicts the trace for $l = 2$ for different degrees of AO correction denoted by the line color. Again, all curves start at the maximum value of 1 at vanishing turbulence and then decay considerably faster than the concurrence. While AO is not able to prevent the decay of the trace, it significantly delays it. For example at $w_0/r_0 = 1.05$, without correction less than 9% of the initially transmitted photons are
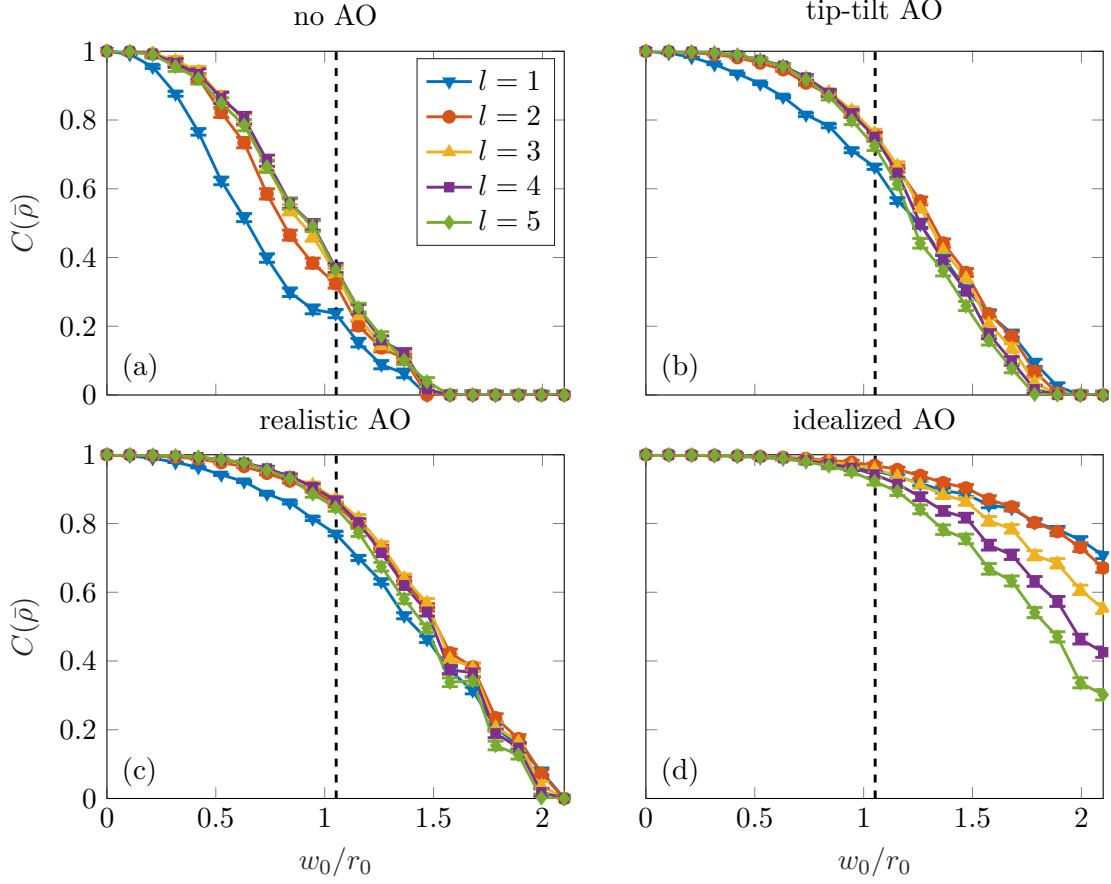
Figure 5.3: Evolution of concurrence for different initial OAM l from 1 to 5 (see legend) – (a) without AO, (b) tip-tilt AO, (c) realistic AO and (d) idealized AO. In all plots, the black dashed line marks the turbulence strength where $\sigma_R^2 = 1$ and by that the transition from weak to strong turbulence. By applying AO, it is possible to delay the loss of concurrence, see (b-d).

detected at Bob's receiver. The simplest correction of tip-tilt achieves approximately 21% and realistic AO 28%. The upper limit given by the idealized AO simulation lies as high as 37%.

Comparing the results for different values of l as shown in Fig. 5.5, one finds that AO correction (b-d) can improve the trace as compared to the case without correction (a) for all values of l. Additionally, as is already known for the case without correction [15, 96, 97], the lower-order OAM modes are less prone to a loss of trace than the higher-order modes. This general behavior is not changed by the action of adaptive optics. Again, idealized AO is more effective than the realistic and tip-tilt AO which have approximately the same performance.
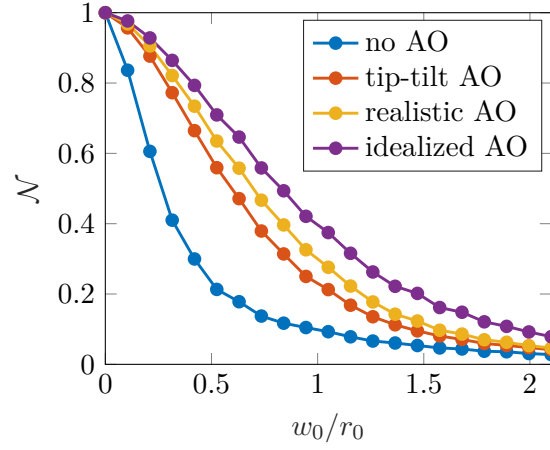
Figure 5.4: Decay of the trace of the received state $\mathcal{N}$ for $l = 2$. Different AO correction schemes can increase the trace and by that reduce the loss of photons to other modes outside of the encoding subspace.
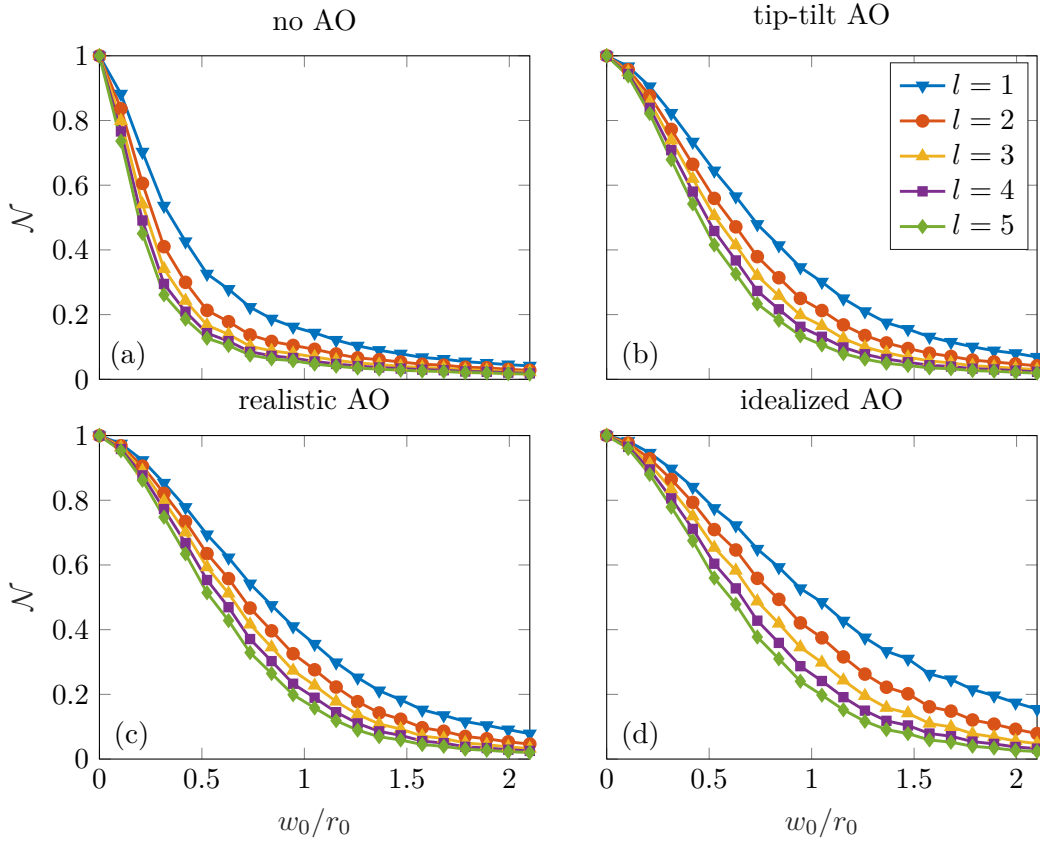

Figure 5.5: Trace for different values of l, (a) without compensation, (b) tip-tilt AO, (c) realistic AO, (d) idealized AO. The error bars of the trace calculated from the standard deviation are too small to be shown.

5.3 Impact on security tests for quantum key distribution

The main advantage of quantum key distribution over the classical transmission of a communication key is its security against eavesdroppers. To verify that an eavesdropper cannot have gained enough information to guess the transmitted key, Alice and Bob can perform tests to determine the number of errors in their transmission which an eavesdropper causes inevitably. Depending on the chosen protocol, one can either perform tests of the quantum bit error rate (e.g. for the BB84 protocol) or, for entanglement-based protocols (e.g. the E91 protocol), evaluate Bell inequalities. From mathematical considerations of the quantum key distribution protocol, one can derive lower bounds of the quantum bit error rate for secure communication. This lower bound depends not only on the quantum key distribution protocol itself but also on the operations assumed to be at the eavesdropper's disposal. For the following considerations, the threshold of 11% which is the commonly accepted threshold for the BB84 protocol is chosen [35]. As already mentioned, the second approach is given by Bell inequalities. With the chosen initial state, the Bell parameter given by Eqs. (2.37) and (2.38) a maximum value of $2\sqrt{2}$ and all values above 2 violate the classical inequality. In the following, both methods are investigated.

Several effects add to the total quantum bit error rate such as detector efficiency and noise statistics which are often setup-dependent. In the considered scenario, the crosstalk between modes in the encoding subspace will have one of the highest contributions. In the following, only the error rate R caused by this crosstalk is considered which is given in terms of the transition matrix elements defined in Eqs. (5.1)

$$R = \frac{1}{\mathcal{N}}\big\langle |g_{-l,l}|^2 + |g_{-l,l}|^2 \big\rangle_{\text{Ensemble}}.$$
(5.17)

It is clear that the total quantum bit error rate has a higher value than R. However, whenever R exceeds the security threshold, so does the quantum bit error rate.

Figure 5.6 shows the crosstalk rate R as a function of w_0/r_0 in the case of $l = 2$. Without compensation (blue line), R rises quickly to a saturation value of 0.5. This corresponds to a case where the number of false measurements equals the number of correct measurements. Only for very weak turbulence does R stay below the security threshold. Tip-tilt compensation improves this situation. With the realistic AO system, the crosstalk rate can be reduced even better. The idealized AO performs best and can achieve a crosstalk rate below the threshold for the largest range of turbulence strengths.
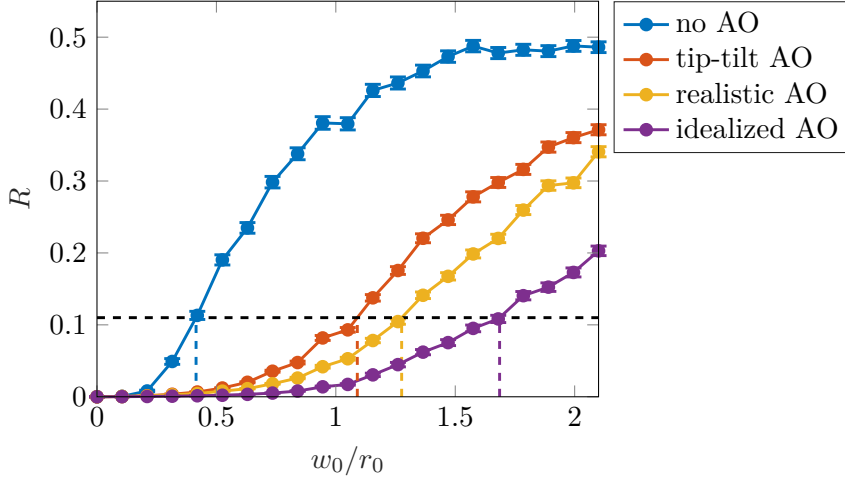
Figure 5.6: Contribution to the quantum bit error rate caused by crosstalk for $l = 2$ versus w_0/r_0 for different AO schemes. The black dashed line indicates the threshold of 11% above which the quantum key transmission may be insecure.

A comparison for values of l between 1 and 5 is shown in Fig. 5.7. It becomes clear that AO can delay the rise of the crosstalk rate above the security threshold. While without AO (a), with tip-tilt AO (b) and with realistic AO (c), the crosstalk rate is higher for lower values of l, the idealized AO compensation (d) leads to an evolution independent of l. The advantage of higher-order OAM modes could be caused by the fact that the larger the value of l, the larger the mode spacing. Since the crosstalk rate only depends on the transition matrix elements which are known to decrease with l, higher-order modes perform better in most cases.

In an entanglement-based protocol such as the E91 protocol, often Bell inequalities are evaluated to check for eavesdroppers and to prove the non-classical nature of the entangled quantum states. The evolution of the Bell parameter in Fig. 5.8 shows that, without correction, a violation of the Bell inequalities is only possible within a limited range of turbulence strengths which is approximately the same for all OAM modes. By applying AO correction, the Bell parameter can be increased. As in all previous plots, the idealized AO is most effective, and the realistic AO performs better than the tip-tilt AO. In the case of idealized AO and for $l = 1$ and $l = 2$, the Bell inequalities are violated within the entire range of simulated turbulence. For all degrees of AO correction, the lower order modes achieve a violation of the Bell inequalities for higher turbulence strengths. An overview of the values at which the Bell parameter approximately intersects with $B = 2$ is given in Tab. 5.1. Since the number of sampling points is limited, a linear evolution was assumed between data points to obtain the
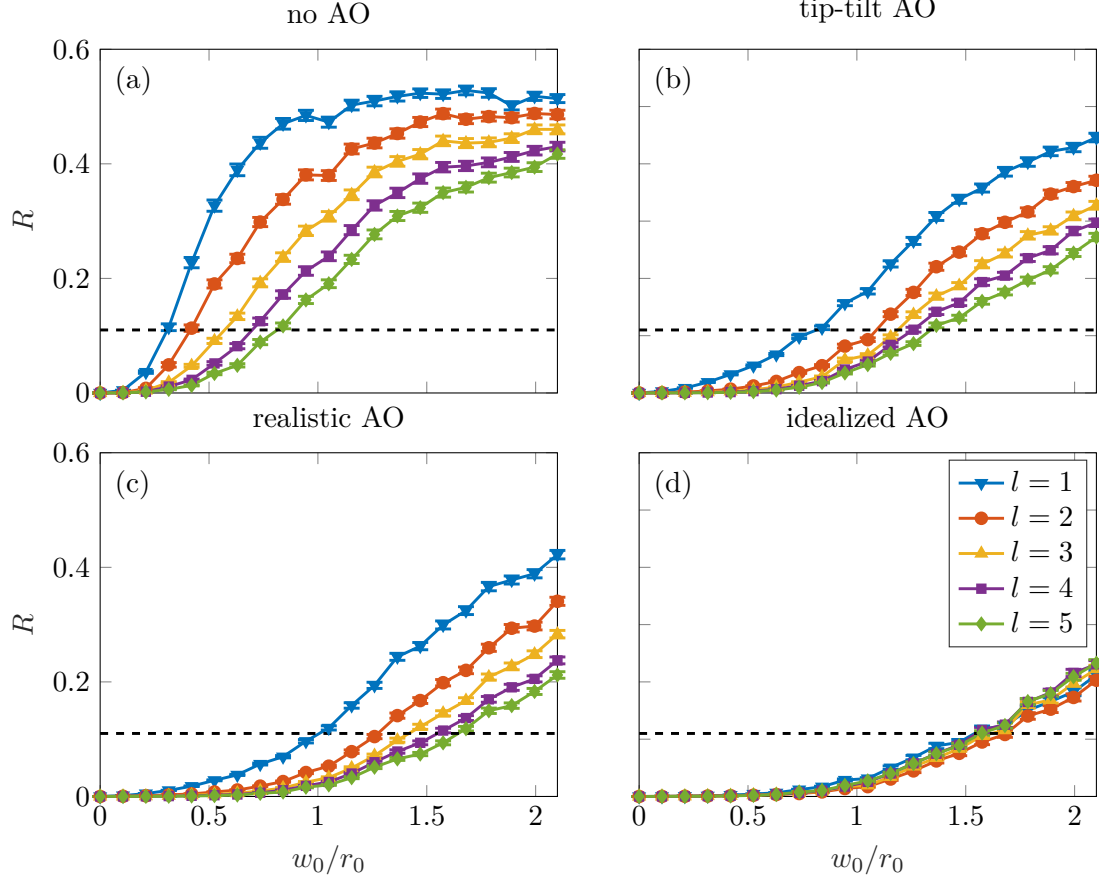
Figure 5.7: Quantum bit error rate caused by crosstalk for different values of l. The dashed black line marks the security threshold of 11%. (a) Without AO, the crosstalk exceeds the security threshold for relatively low turbulence strengths. (b) Tip-tilt AO, (c) realistic AO and (d) idealized AO can increase the turbulence range where communication would be secure significantly.

intersection between the simulation data and the $B = 2$ curve. With AO, the Bell inequality is violated in a smaller turbulence range for larger OAM values. In addition, idealized AO performs best, and realistic AO allows for stronger turbulence strengths than tip-tilt AO.

5.4 Limitations of phase-only adaptive optics compensation

After the description of AO compensation efficiency in the previous sections, the question may arise why the idealized AO cannot completely recover the initial state. To understand this, it is instructive to examine the efficiency of idealized AO as a function of the turbulence strength w_0/r_0. In particular, one can see that below the transition
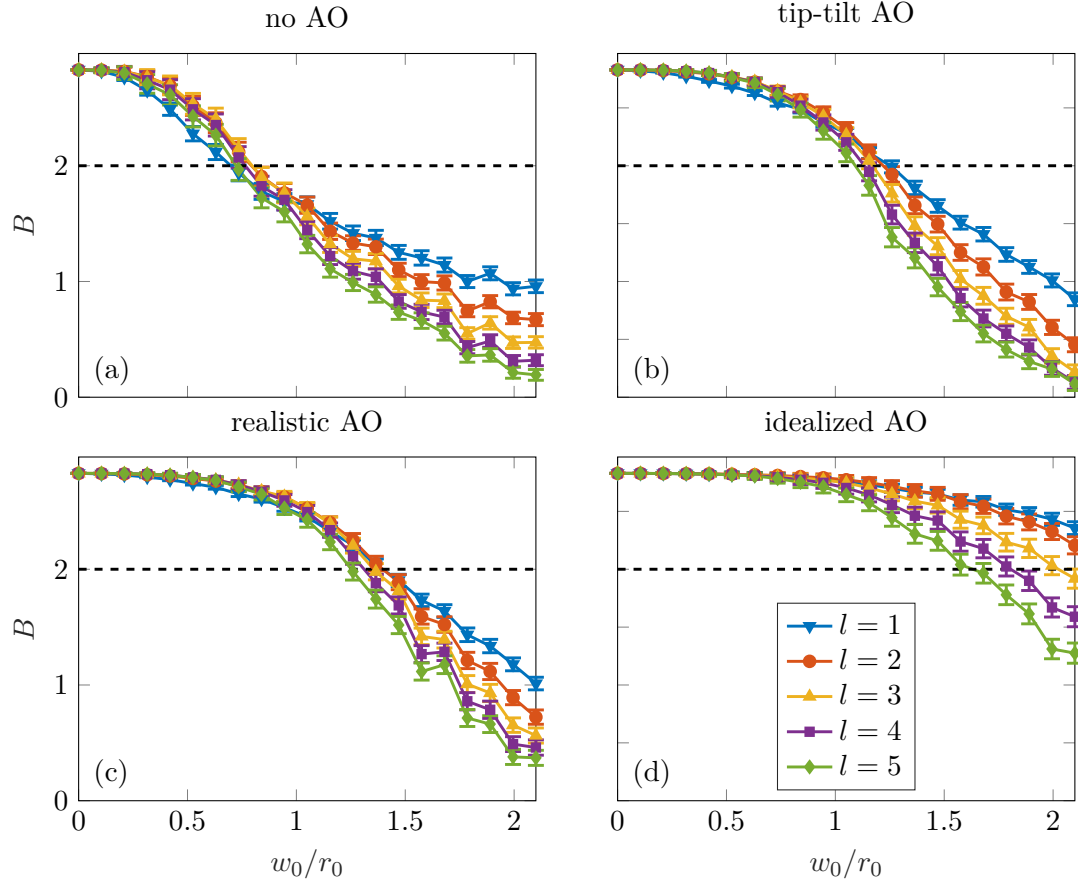
Figure 5.8: Bell parameter versus turbulence strength for OAM between 1 and 5 encoded by the line color. The dashed black line indicates the transition between a violation of the Bell inequality at $B = 2$. The different degrees of AO compensation are compared in the plots – (a) no correction, (b) tip-tilt, (c) realistic and (d) idealized AO. The higher the degree of compensation, the longer can the Bell inequalities be violated.

l	no correction	tip-tilt AO	realistic AO	idealized AO
$l = 1$	0.7	1.3	1.4	2.1*
$l = 2$	0.8	1.2	1.4	2.1*
$l = 3$	0.8	1.2	1.4	2.0
$l = 4$	0.8	1.1	1.3	1.8
$l = 5$	0.7	1.1	1.3	1.6

Table 5.1: Value of w_0/r_0 for which the Bell parameter reaches a value of 2 depending on the initial OAM l and the degree of correction, compare also to Fig. 5.8. For values marked by * $B = 2$ is not reached, but the highest value of w_0/r_0 in the simulation is given.

from weak to strong turbulence (at $w_0/r_0 = 1.05$) the idealized AO has a very high efficiency, see e.g. Fig. 5.3 where $w_0/r_0 = 1.05$ is marked by the black dashed line. However, the idealized AO quickly degrades as the turbulence strength increases beyond this boundary. In fact, this behavior is not so surprising since the transition to stronger scintillation is basically defined by the fact that turbulence distorts not only the phase but also the intensity distribution.

Clearly, a phase-only compensation, regardless of its efficiency, cannot correct for the intensity distortions. It may thus be necessary to take a different design approach. One possibility would be to use pre-compensation, which has been mentioned in Sec. 4.1. In that case, an AO system is implemented at the transmitter. The photon's wavefront is then deliberately distorted before propagation such that after propagation the wavefront is plane. This requires a beacon to be sent in the opposite direction of the light and thus adds complexity both at the transmitter and the receiver. Pre-compensation is often considered in the context of classical Earth-to-satellite communication where it compensates the uplink traveling from the ground station to the satellite. In such a propagation geometry, turbulence distortions occur only on the first few kilometers of the propagation distance such that pre-compensation is the only physically meaningful compensation technique. In the horizontal propagation scenario considered here, the pre-compensation cannot correct for the phase distortions occurring closer to the receiver. Hence, two AO systems would be required. Still, pre-compensation is a relatively new approach and only a few publications on it exist [13, 85, 98, 99].

5.5 Comparison to experimental data from the literature

The goal of this section is to put the presented simulation results into perspective with experimental results from the literature – first for the turbulence model and then for the combination of turbulence and adaptive optics. For a summary of the state of the art of OAM communication, with and without adaptive optics, please refer to Sec. 2.4. The split-step method, which was also used in this thesis to numerically model the propagation of OAM photons through atmospheric turbulence, has been verified in experiments [62]. It was shown that the increased stability of the entanglement of higher-order OAM modes known from weak turbulence theory is gradually reduced as scintillation becomes important until the modes all perform equally [62]. In the presented simulations, many of the OAM modes show the same entanglement decay,

apart from $l = 1$ and $l = 2$ which still have a slightly lower concurrence than the higher-order modes. Since the propagation scenario considered in this thesis corresponds to medium scintillation, the presented theoretical results, without adaptive optics, are in agreement with the experiments presented in Ref. [62].

A comparison to experiments with adaptive optics is unfortunately more difficult. As was already discussed in Sec. 2.4, no free-space experiments with OAM and adaptive optics have been presented. Furthermore, the author is not aware of any quantum experiments with OAM and AO. The results of this thesis agree with the classical experiments in that they show a reduction of the crosstalk between OAM modes. A quantitative comparison to the known laboratory experiments [11, 12, 52, 100] is however limited because of several differences in the considered setup. First, many laboratory experiments use a different kind of OAM modes which consist of a superposition of several radial orders rather than the Laguerre-Gauss modes with $p = 0$ and azimuthal index l considered in this thesis. As was pointed out in Ref. [101], these modes exhibit a much broader beam profile, the width of which is proportional to $|l| + 1$ instead of $\sqrt{|l| + 1}$. For the practical implementation of an OAM link, such broad OAM modes have the disadvantage of fitting fewer modes into the same receiving aperture as the pure Laguerre-Gauss modes. Second, the laboratory experiments either used a single phase screen approach and could thus only model weak turbulence [12, 52, 100] or they used two phase screens to model moderate turbulence [11]. For example, Ref. [12] finds a reduction of the crosstalk rate to adjacent modes of 12 dB with adaptive optics. The experiment used a single phase screen thus modeling weak turbulence and a static AO system with a very high resolution most similar to the idealized AO setup in this thesis. In the presented simulations, a comparable improvement of 11.2 dB of the crosstalk rate to adjacent modes with OAM $\pm(|l| - 1)$ can be achieved for the weakest simulated value of turbulence ($w_0/r_0 = 0.105$). For moderate turbulence ($w_0/r_0 = 1.05$), the crosstalk rate is only reduced by a factor between 3.3 and 6.8 dB. This is however not surprising because of the differences between the simulation scenario and the experiments discussed above.

Clearly, a free-space experiment with OAM photons including adaptive optics remains to be demonstrated. The results presented in this chapter give a clear motivation to perform such an experiment. The next chapter investigates the influence of the beacon beam waist on the compensation efficiency which points out the importance of choosing the proper beacon. Overall, the results of this thesis are expected to give new impulses to experimental studies on OAM communication in free space.

Chapter 6

Influence of beacon beam waist on compensation efficiency

In this chapter, the suitability of the Gaussian beacon beam to measure the phase distortions of the OAM photons is evaluated. It is known that Laguerre-Gauss modes have a broader beam profile than the fundamental Gaussian mode which can be seen from the formula for the root-mean-square radius given by [65]:

$$\sqrt{\langle r^2 \rangle} = \sqrt{2p + l + 1}\, w_0\,. \tag{6.1}$$

Hence, the Gaussian beacon and the Laguerre-Gauss signal have a different footprint as they pass through the phase distortions caused by atmospheric turbulence. This could lead to different turbulence distortions which consist not only of the phase fluctuations but evolve into intensity fluctuations upon propagation. In addition, the Laguerre-Gauss signal and the Gaussian beacon have a different beam width at the receiver which has an impact on the wavefront measurement in the tip-tilt and the realistic AO model. In previous studies of classical OAM communication with adaptive optics, it was mentioned that the beacon is chosen larger than the OAM beam to ensure an increased overlap of their beam profiles [11]. A detailed investigation of the beacon beam waist as presented in the following chapter has not been published elsewhere, to the best of the author's knowledge.

To investigate its influence, simulations similar to those presented in the previous chapter, Ch. 5, were performed where the beacon beam waist was varied in a certain range. Section 6.1 details the adaption of the simulation routine and gives an overview of the obtained results. The different quantities relevant for quantum key distribution,

concurrence, trace, crosstalk rate and the Bell parameter, which are already known from the last chapter, are evaluated, in particular with respect to the beacon beam waist. Based on the results, the Bell parameter is chosen as the figure of merit for the optimization. In Sec. 6.2, the optimal beacon beam waist is derived as a function of the initial OAM l and the AO compensation scheme. Finally, the improvement that can be achieved by this optimization is evaluated in Sec. 6.3.

6.1 Overview of simulations with different beacon beam waists

To investigate the influence of the beacon beam waist on AO compensation of OAM modes, in particular in the context of quantum key distribution, the simulations from the previous chapter were extended. Instead of using a fixed value as in Ch. 5, the beacon beam waist was iterated within the range of $0.4w_0 \leq w_b \leq 2.45w_0$, where w_0 corresponds to the Laguerre-Gauss beam waist. This range was predetermined by the sampling criteria for the chosen simulation parameters, see Sec. 3.3. But, these upper and lower bounds are also meaningful from an experimental point of view. The sending telescope aperture was chosen to be $w_0 = \frac{D}{\pi 2.45}$. According to Eq. (3.27), the loss of optical power is below 1% for the largest OAM mode with $p = 0, l = 5$. By rewriting Eq. (3.27), one can find an inequality for the beacon beam waist $w_b \leq D/\pi = 2.45w_0$. Accordingly, a Gaussian with a beam waist larger than $2.45w_0$ would indeed require a larger sending telescope aperture which increases the cost of the system and is thus unfeasible in most cases. Furthermore, the use of a much smaller beacon may cause other experimental problems. Generating a very small beacon could be difficult within a telescope with a large aperture and could thus require an auxiliary telescope. In that case, the alignment of the signal and beacon telescope is crucial for the efficiency of the experiment. In addition, there would be a displacement between the two optical axes which would lead to differences in the experienced atmospheric turbulence and thus reduce the AO correction efficiency. Last but not least, small beacon beam waists increase the beam broadening due to diffraction. While this facilitates establishing the optical link, the overall power of the beam needs to be increased to be able to measure the signal which can also become an issue of eye-safety.

For all simulations, the Laguerre Gaussian beam waist w_0 is constant, see Tab. 3.1, for all values of l. For each value of w_b, the beacon field is propagated through atmospheric turbulence as described earlier. Since AO compensation is applied to the Laguerre-Gauss modes after propagation, the signal field is propagated only once for

all values of w_b. As in Ch. 5, the simulations for each set of parameters is averaged over 1000 realizations of turbulence.

In the following, the same quantities as in the last chapter are evaluated – the concurrence C, see Eq. (2.29), and the trace $\mathcal{N}$ of the final state density matrix, see Eq. (5.15), the crosstalk rate R contributing to the quantum bit error rate, see Eq. (5.17), and, in addition, the Bell parameter B. Figures 6.1, 6.2, 6.4 and 6.5 give an overview over the simulation results and are all arranged in the same way. The individual plots show the given quantity as a function of the initial beacon waist w_b. Each curve corresponds to one value of w_0/r_0 which is encoded in the color of the lines. The columns encode the different degrees of AO compensation – (left) tip-tilt, (middle) realistic and (right) idealized AO. The rows represent different values of OAM running from 1 to 5 arranged from top to bottom, respectively.

First, the quantities that are also connected to *classical* communication are considered, the trace $\mathcal{N}$ and the crosstalk rate R. The trace is proportional to the received signal in classical communication; it gives the ratio between the received and the transmitted optical power. The crosstalk rate is proportional to the channel crosstalk. The trace shown in Fig. 6.1 saturates for larger values of w_b. The higher the initial OAM l, the larger w_b needs to be. For the higher values of l, one can see that also a small initial beacon waist could be feasible. The starting point of this saturation also depends on the type of AO compensation. For the realistic AO it needs to be larger than for the idealized AO. The influence of the beacon waist is strongest for the realistic AO. For example in the case of $l = 5$, there is a deep dip in the curve. For the trace, the tip-tilt AO is least influenced by the beacon waist. The crosstalk rate R depicted in Fig. 6.2 behaves similar to the trace. For low values of w_b, there is a region of larger crosstalk in the realistic AO scenario. For the other scenarios the performance is mostly independent of the beacon beam waist as long as it is larger than approximately w_0.

Now the question arises why the realistic AO is more susceptible to the beacon waist than tip-tilt and idealized AO. One can understand this from the fact that the realistic AO has a threshold for the Shack-Hartmann sensor as discussed in Sec. 4.4. It discards those micro lenses that receive less than 1% of the irradiation received at the micro lens with the highest irradiation. For a narrow beam, which has an intensity profile that drops rapidly, only the micro lenses in the center receive enough irradiation. With just a few data points available, the wavefront fitting error is thus higher than for a broader beam illuminating many micro lenses. While it is possible to use the results from these micro lenses, experimentally the calculated results could not be trusted.
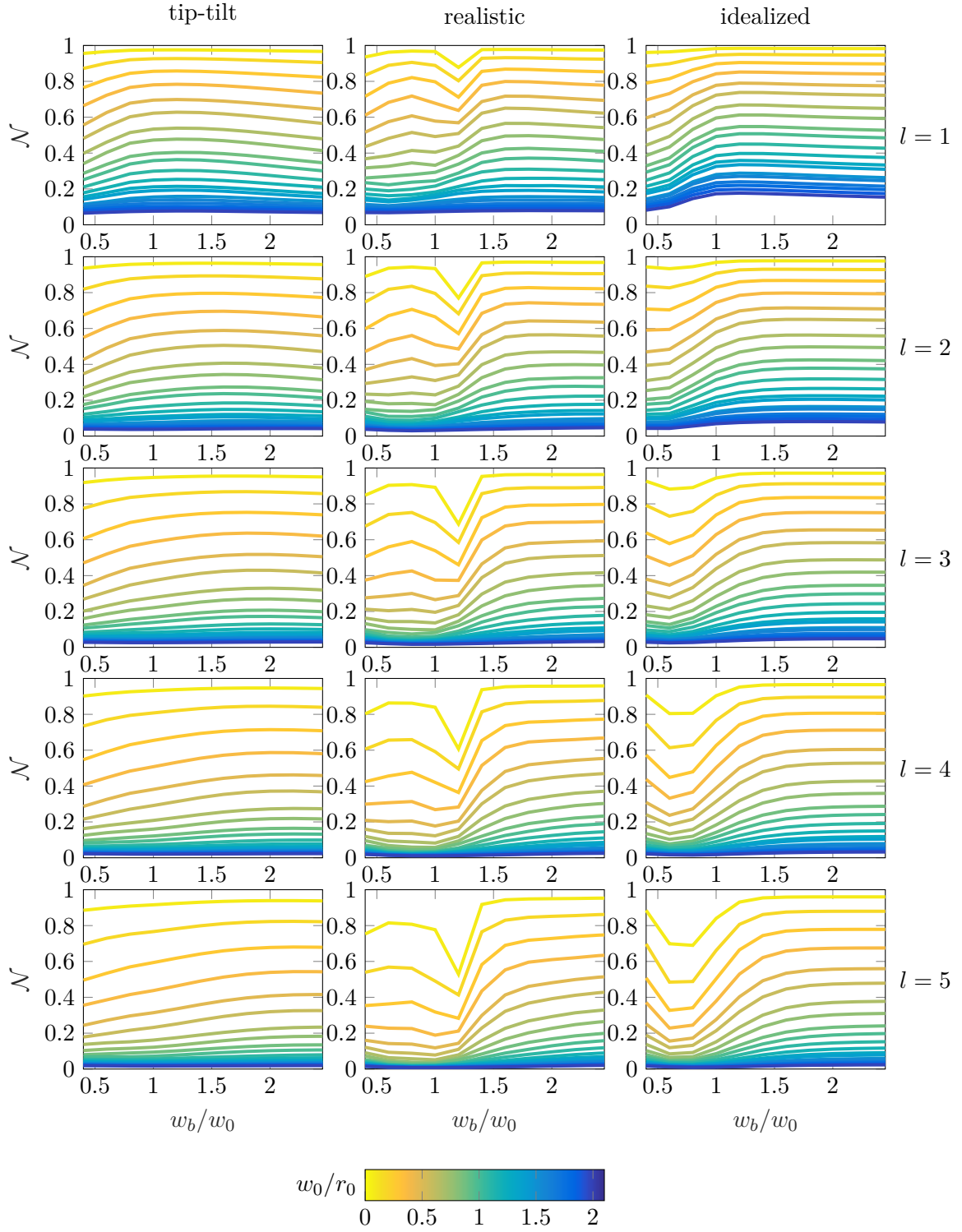
Figure 6.1: Trace of the received state for w_0/r_0 as encoded by the color of each line versus the initial beacon beam waist. Each column corresponds to one AO correction scheme, with tip-tilt, realistic and idealized AO from left to right, respectively. The rows stand for different values of OAM between 1 and 5.
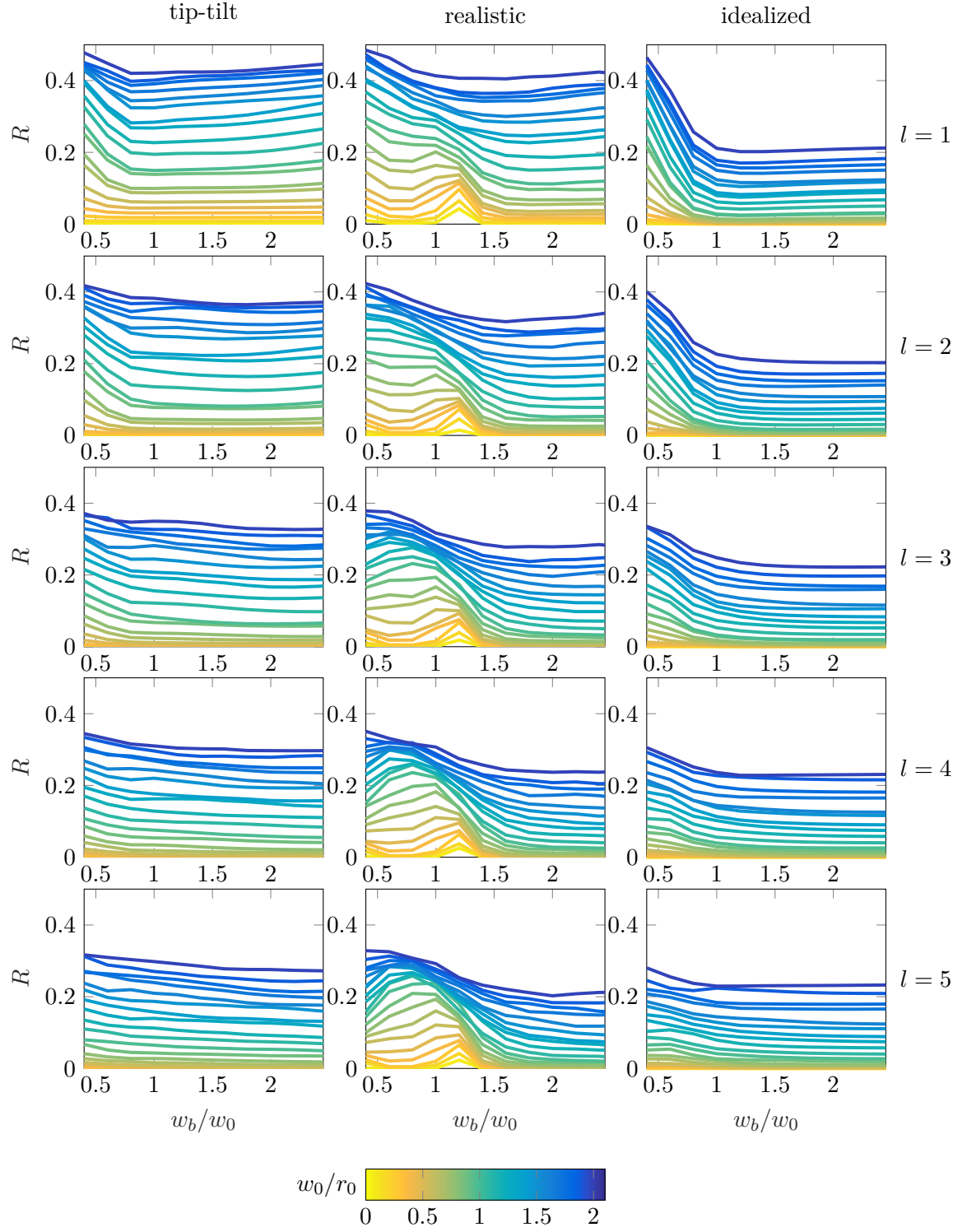
Figure 6.2: Crosstalk rate for different turbulence strengths w_0/r_0 encoded by the color of the curves, AO correction schemes denoted by the column of the plot and initial OAM given by the row of the plot.
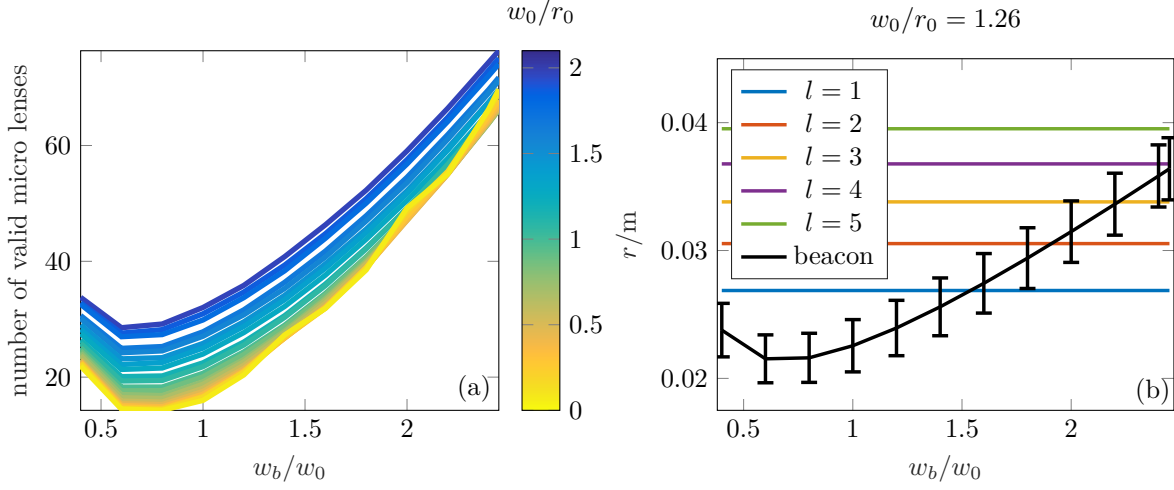
Figure 6.3: Influence of beacon beam waist on realistic AO compensation. (a) Number of valid micro lenses plotted against beacon beam waist. The color encoding of the curves indicates their respective turbulence strength. (b) Short-term beam radius of the beacon at the receiver (black) versus the initial beacon beam waist w_b for $w_0/r_0 = 1.26$. The beam radii of the Laguerre-Gauss modes are indicated by the colored lines. The error bars for the beacon indicate the large fluctuation of the received beam radius and are omitted for the Laguerre-Gauss modes for clarity.

For a camera pixel receiving too little illumination, the shot noise becomes comparable or even equal to the signal. The resulting errors of the centroids and the associated wavefront fitting errors are not included in the calculation, but are instead included implicitly by the threshold.

To visualize the dependence of the initial beacon beam waist on the wavefront measurement, Fig. 6.3(a) shows the number of valid micro lenses against the initial beacon waist w_b. In addition, Fig. 6.3(b) plots the beacon radius at the receiver versus the initial beam waist w_b for one value of w_0/r_0. This quantity was calculated from the optical field by the root-mean-square of the radius weighted by the beacon irradiance

$$r = \sqrt{\frac{\sum |u|^2[(x - x_c)^2 + (y - y_c)^2]}{\sum |u|^2}} \,, \tag{6.2}$$

where the centroids x_c and y_c are calculated by

$$x_c = \frac{\sum_{i,j} |u_{i,j}|^2 x_{i,j}}{\sum_{i,j} |u_{i,j}|^2} \,, \qquad y_c = \frac{\sum_{i,j} |u_{i,j}|^2 y_{i,j}}{\sum_{i,j} |u_{i,j}|^2} \,, \tag{6.3}$$

see also Eqs. (4.8,4.9). As can be seen in Fig. 6.3(b), the beacon radius at the receiver has a minimum around $w_b = 0.7w_0$ and the curve has a similar evolution as that for

the number of detected micro lenses shown in Fig. 6.3(a). For a large initial beam waist, it increases slowly. For small initial beam waist, the curve increases rapidly. The figure additionally shows the calculated beam radii for the Laguerre-Gauss modes. As expected, the resulting values increase with increasing mode index l. This also makes clear why, especially for high values of l, also the lower values of w_b lead to a good AO correction where beacon and signal are again of similar size.

As can be seen in Figs. 6.4 and 6.5, the concurrence and the Bell expectation value B show a slightly different behavior than the trace and the crosstalk rate. While the idealized AO saturates for larger beacon radii, the realistic and tip-tilt AO show a decline for large values, indicating that there is an optimum beacon radius. This is particularly interesting because classical communication protocols as well as the single photon BB84 protocol are evaluated by only considering the trace and the quantum bit error rate while an entanglement-based protocol such as the E91 works only if the Bell inequalities are violated; the BB84 and E91 protocols were both introduced in Sec. 2.3. To understand the difference between these quantities, one can reexamine their calculation. The trace and the crosstalk rate only take the average absolute value of the transition matrix elements into account. In contrast, the concurrence and Bell inequality depend on the average value of the transition matrix elements. Since the transition matrix elements are complex numbers, the results can be highly different. The complex phase can produce an interference-like reduction of the sum. To summarize, the parameters important for quantum protocols seem to be more sensitive to the beacon beam waist than those for classical protocols. This could also explain why the beacon waist has not been investigated in detail in previous studies but has rather been chosen considerably larger than the OAM beam waist. Based on this finding, the following discussions will be restricted to the concurrence C and the Bell parameter B. Furthermore, the Bell parameter provides a strict criterion – if it has a value above 2, a Bell inequality is violated, otherwise it is not.

6.2 Performed optimization

As detailed in the previous section, the Bell parameter has been chosen as the figure of merit to optimize the beacon beam waist since its value is most sensitive to the beacon beam waist and provides a strict criterion for the suitability for quantum key distribution. The parameter B was calculated for each value of turbulence strength w_0/r_0, OAM l between 1 and 5, AO compensation scheme and, most importantly,
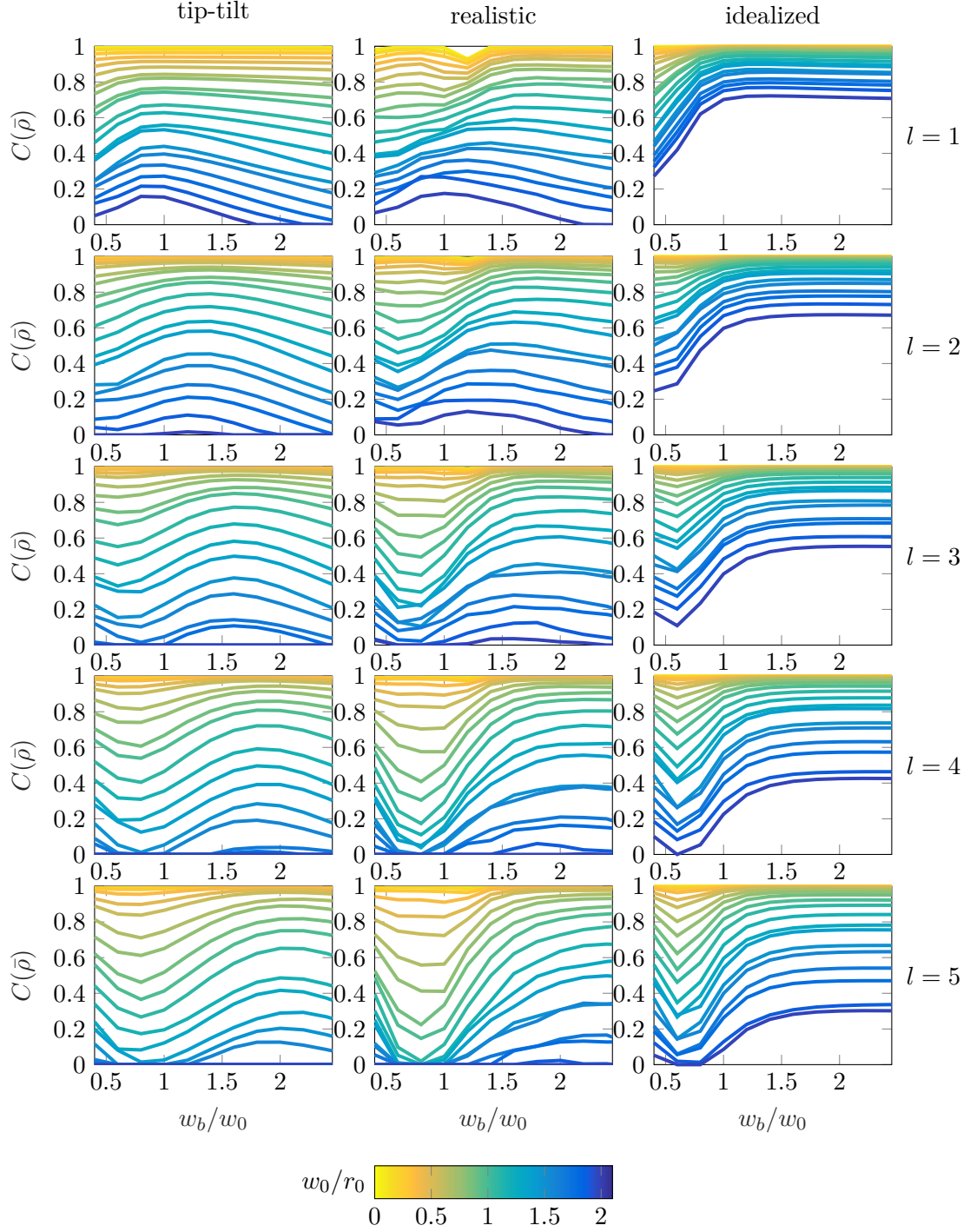
Figure 6.4: Concurrence in dependence of the beacon beam waist w_b: (left column) tip-tilt, (middle column) realistic and (right column) idealized AO are compared for different OAM values between 1 and 5 in the rows from top to bottom, respectively. Each curve has a color that encodes the turbulence strength w_0/r_0 as indicated by the colorbar below.

Figure 6.5: Bell parameter in dependence of the beacon beam waist w_b: (left column) tip-tilt, (middle column) realistic and (right column) idealized AO are compared for different OAM values between 1 and 5 in the rows from top to bottom, respectively. Each curve has a color that encodes the turbulence strength $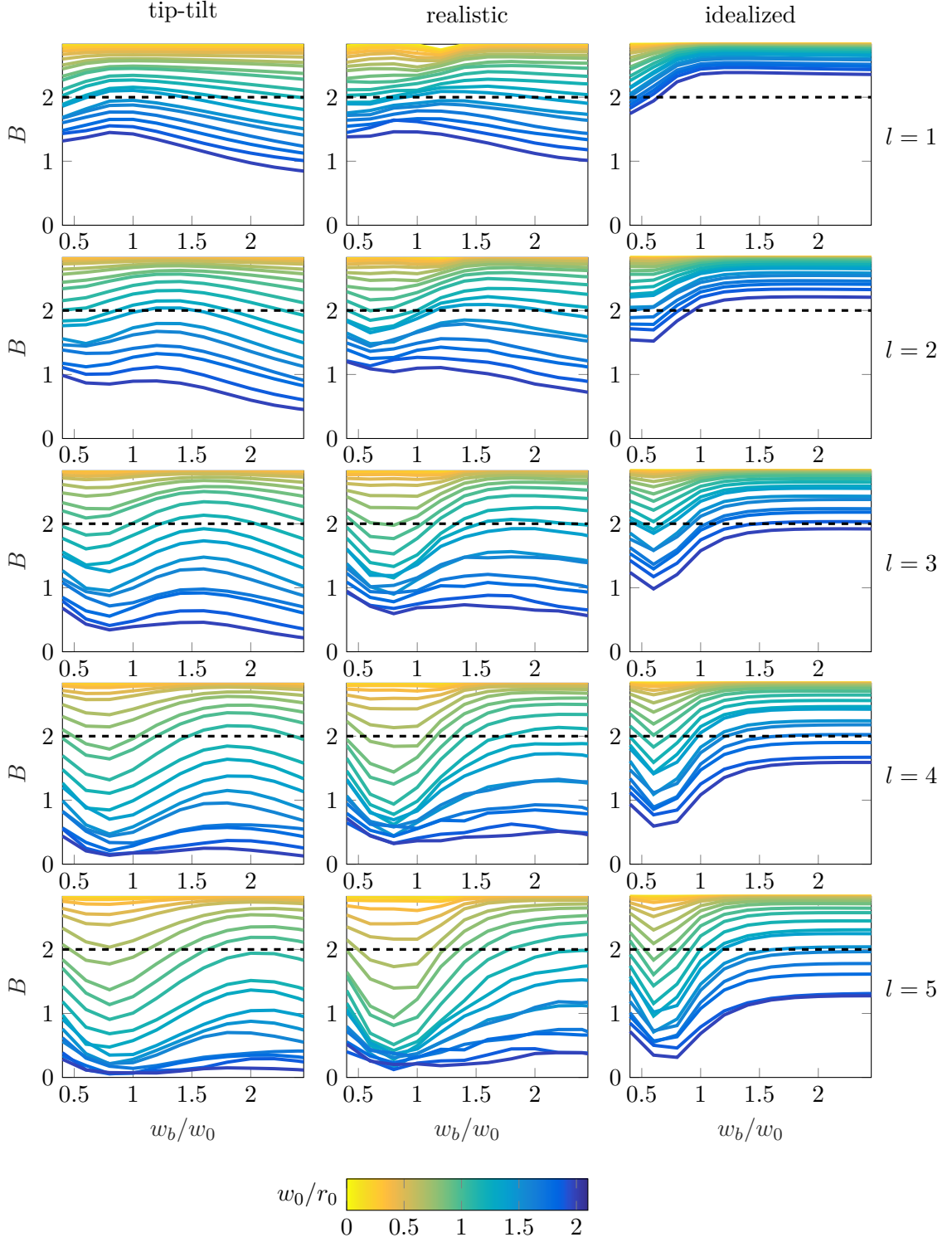w_0/r_0$ as indicated by the colorbar below. The black dashed line indicates the value of 2 above which a Bell inequality is violated.

initial beacon beam waist w_b between $0.4w_0$ and $2.45w_0$. The goal of the following calculation is to find the optimum beacon beam waist which may depend on the OAM value and the compensation scheme. However, the optimum beacon beam waist should not depend on the turbulence strength since atmospheric conditions may change on a short time scale during an experiment and a real-time optimization of the beacon beam waist is hardly feasible.

To find suitable values of w_b, the simulation data were scanned for violations of the Bell inequality that are at least 90% of the maximum violation for that data set and value of w_0/r_0

$$B(w_b) - 2 \overset{!}{\geq} 0.9 \max\{B(w_b) - 2\} . \tag{6.4}$$

By this definition, the overall decay of S with increasing turbulence strength is not part of the optimization. The values of w_b for which Eq. (6.4) is fulfilled are depicted by the error bars in Fig. 6.6 and plotted against the turbulence strength w_0/r_0. At the points marked by circles, S takes its maximum value for the respective set of parameters. For all degrees of AO compensation (denoted by different columns) and values of OAM (running from 1 to 5, denoted by the rows), one can observe that the number of acceptable beacon beam waists spans the entire simulated interval for weak turbulence and narrows as the turbulence strength increases. It should be noted that for the strongest values of turbulence, the Bell inequalities are not violated and thus there are no more points in the plot. In accordance with the earlier discussion in Sec. 6.1, one can see that the intervals of acceptable w_b are largest for the idealized AO (right column), indicating that it is least influenced by the beacon beam waist. The plots also show the optimum beacon beam waist w_b (red and black line) which was obtained from the calculation described in the following.

As can be seen in Fig. 6.6, for low values of w_0/r_0, there exist many beacon beam waists such that the Bell inequality is violated. This number decreases as the turbulence strength increases. For large turbulence strength, the choice of the proper beacon beam waist can thus be essential in violating the Bell inequality. To account for this effect, a weighted average was chosen which stresses the importance of the values with a small range of acceptable w_b values. This is achieved by the following standard formula to obtain a weighted average from measurement data with different uncertainties [102, p. 50]

$$w_{b,opt} = \frac{\sum_j w_j/\Delta_j^2}{\sum_j 1/\Delta_j^2} , \tag{6.5}$$
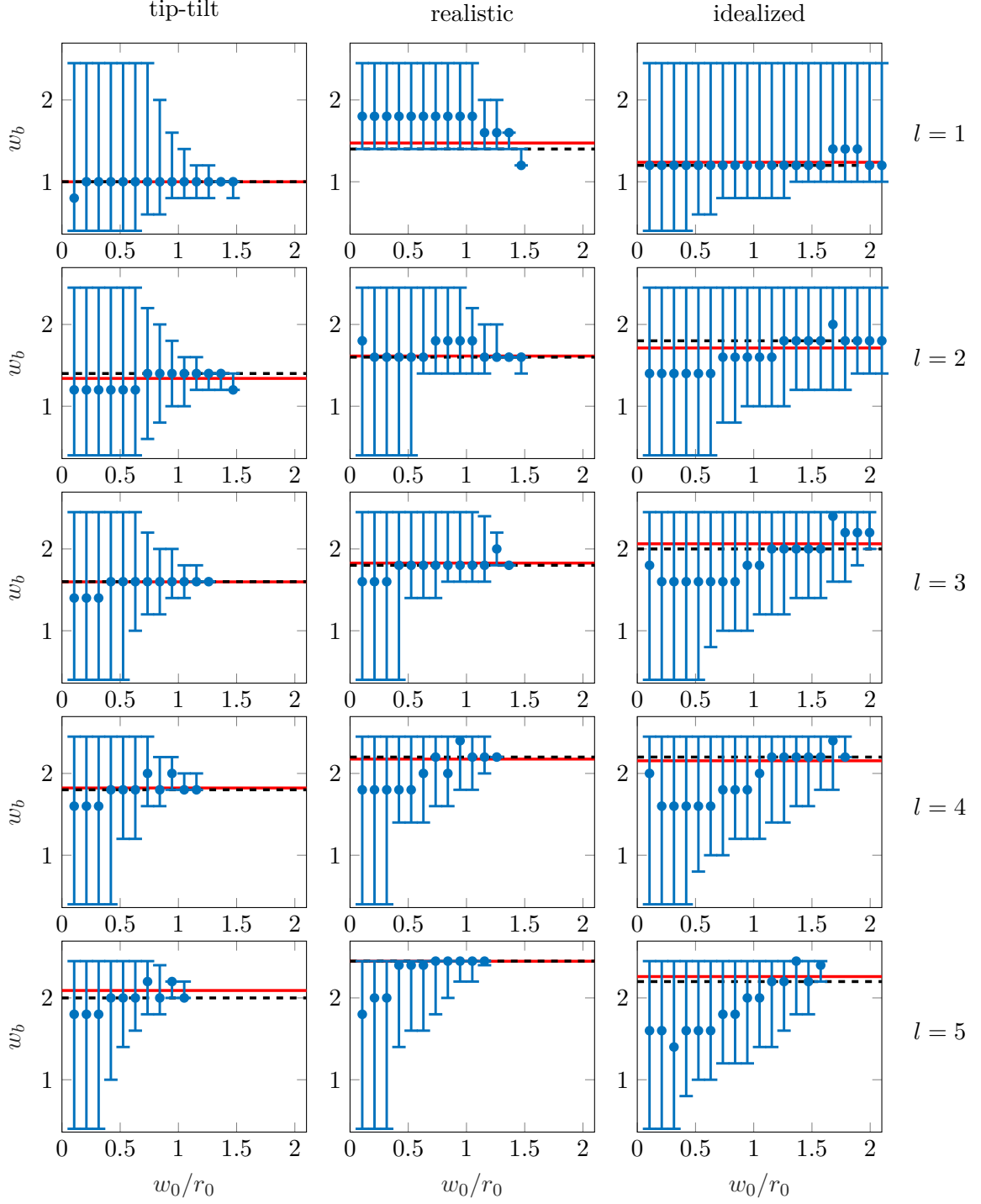
Figure 6.6: Beacon beam waists w_b for which $B(w_b) = 0.9 \max\{B(w_b)\}$ is fulfilled plotted versus the turbulence strength w_0/r_0 (blue error bars). The blue circles show where S takes its maximum value. The three AO schemes are compared – (left row) tip-tilt AO, (middle row) realistic AO and (right row) idealized AO. The values of OAM are denoted at the end of the column. The red lines indicate the optimum beacon waist calculated by a weighted average. The black line marks the value of w_b closest to this optimum which is included in the set of simulated values.

	tip-tilt		realistic		idealized AO	
	calculated	chosen	calculated	chosen	calculated	chosen
$l = 1$	1.00 ± 0.06	1.00	1.47 ± 0.06	1.40	1.24 ± 0.18	1.20
$l = 2$	1.34 ± 0.05	1.40	1.61 ± 0.06	1.60	1.71 ± 0.16	1.80
$l = 3$	1.60 ± 0.06	1.60	1.83 ± 0.08	1.80	2.06 ± 0.12	2.00
$l = 4$	1.82 ± 0.06	1.80	2.18 ± 0.08	2.20	2.15 ± 0.09	2.20
$l = 5$	2.09 ± 0.07	2.00	2.45 ± 0.02	2.45	2.26 ± 0.09	2.20

Table 6.1: Optimum beacon beam waists w_b calculated from Eqs. (6.5) and (6.6) for tip-tilt, realistic and idealized AO. The approximated values chosen closest to the calculated values and from the set of simulated values of w_b listed in the right columns are used in Sec. 6.3 to evaluate the improvement achieved by the optimization.

where the sum is performed over the different values of turbulence strengths w_0/r_0 for each set of OAM and compensation efficiency individually. The value of w_j is the value of w_b for which B takes its maximum value and Δ_j is half of the interval denoted by the error bars in Fig. 6.6. One can see in Fig. 6.6 that the error bars are not distributed symmetrically around the maximum value (denoted by the circle) which is not taken into account. Turbulence strengths are not included in the calculation if Bell inequalities are not violated for any of the beacon beam waists. If there is only one data point that violates the inequality, Δ_j is set to half the distance to the next data point to avoid division by 0. By this calculation, the red lines in Fig. 6.6 are obtained. Since the simulations were only performed for a certain number of w_b values, the calculated optimum was rounded to the next closest value for which simulations were performed. The results are shown by the black dashed line in Fig. 6.6. To estimate the sensitivity to the beacon beam waist, also the width of this interval is calculated,

$$\Delta_{opt} = \frac{1}{\sqrt{\sum_j 1/\Delta_j^2}} \,, \tag{6.6}$$

in the same way as the uncertainty of a weighted average. If Δ_{opt} is small, only few values of w_b are suitable, meaning that finding the best beacon beam waist has a larger impact. Table 6.1 lists the resulting values for the three AO compensation schemes and values of OAM between 1 and 5. These values are used in the next section to investigate the improvement achieved by this optimization.

6.3 Improvement achieved by beacon optimization

From the optimum beacon beam waist, the quantities investigated in Ch. 5 can be reevaluated. As discussed in Sec. 6.1, the trace and quantum bit error rate only depend very weakly on the beacon beam waist. Therefore, these plots will not be repeated here, but are included in the Appendix C for completeness. Instead, this section focuses on the concurrence and Bell inequality violation. First, consider the concurrence shown in Fig. 6.7. The topmost plot shows the evolution of the concurrence without adaptive optics and is repeated here for convenience. The second row of plots shows the results with tip-tilt correction, (left) with the initial fixed value of $w_b = 2.45w_0$ and (right) with the optimized value given in Tab. 6.1. One can see that the concurrence is preserved longer after the optimization. The improvement is especially noticeable for $l = 1$ which is not well-corrected for a large beacon beam waist. For the realistic AO system, the improvement is slightly less pronounced, which could be due to the fact that the optimized beacon was higher for this case and the initial value of $w_b = 2.45w_0$ thus closer to the optimum. For $l = 1$, as compared to the tip-tilt case, there is hardly an improvement by using the realistic AO. However, the higher values of l perform better with realistic AO than in the tip-tilt case. In the idealized AO case, the optimization of the beacon does not influence the correction efficiency.

To get a more detailed impression of the improvements caused by the beacon optimization, the value of B is shown in Fig. 6.8. It is arranged in the same way as the previous figure, Fig. 6.7, with the uncorrected case on top and the results with a fixed beacon in the left column and those for the optimized beacon in the right column. The lines with plot markers indicate the values of B while the dashed colored lines indicate the turbulence strength where $B = 2$ indicating the transition from violation to non-violation of the Bell inequality. For tip-tilt and realistic AO, B remains higher for stronger values of turbulence with the optimized beacon beam waist. It should be noted that the realistic AO is more successful in securing a violation of the Bell inequality, in particular for $l > 2$.
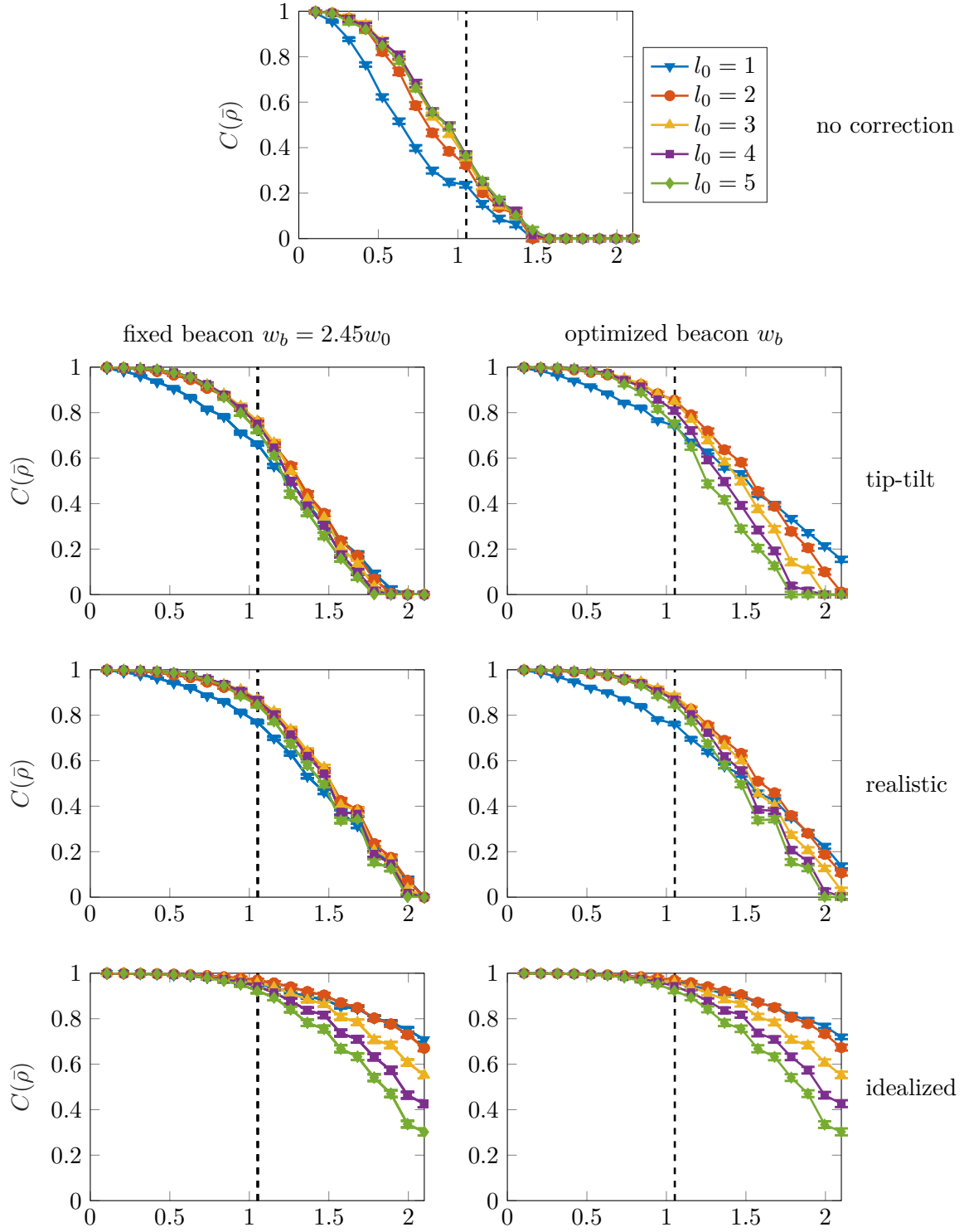
Figure 6.7: Concurrence evolution before (left column) and after (right column) optimization of the beacon beam waist. The topmost plot shows the evolution without AO correction. The second to fourth row compare the different degrees of AO correction – tip-tilt, realistic and idealized AO.
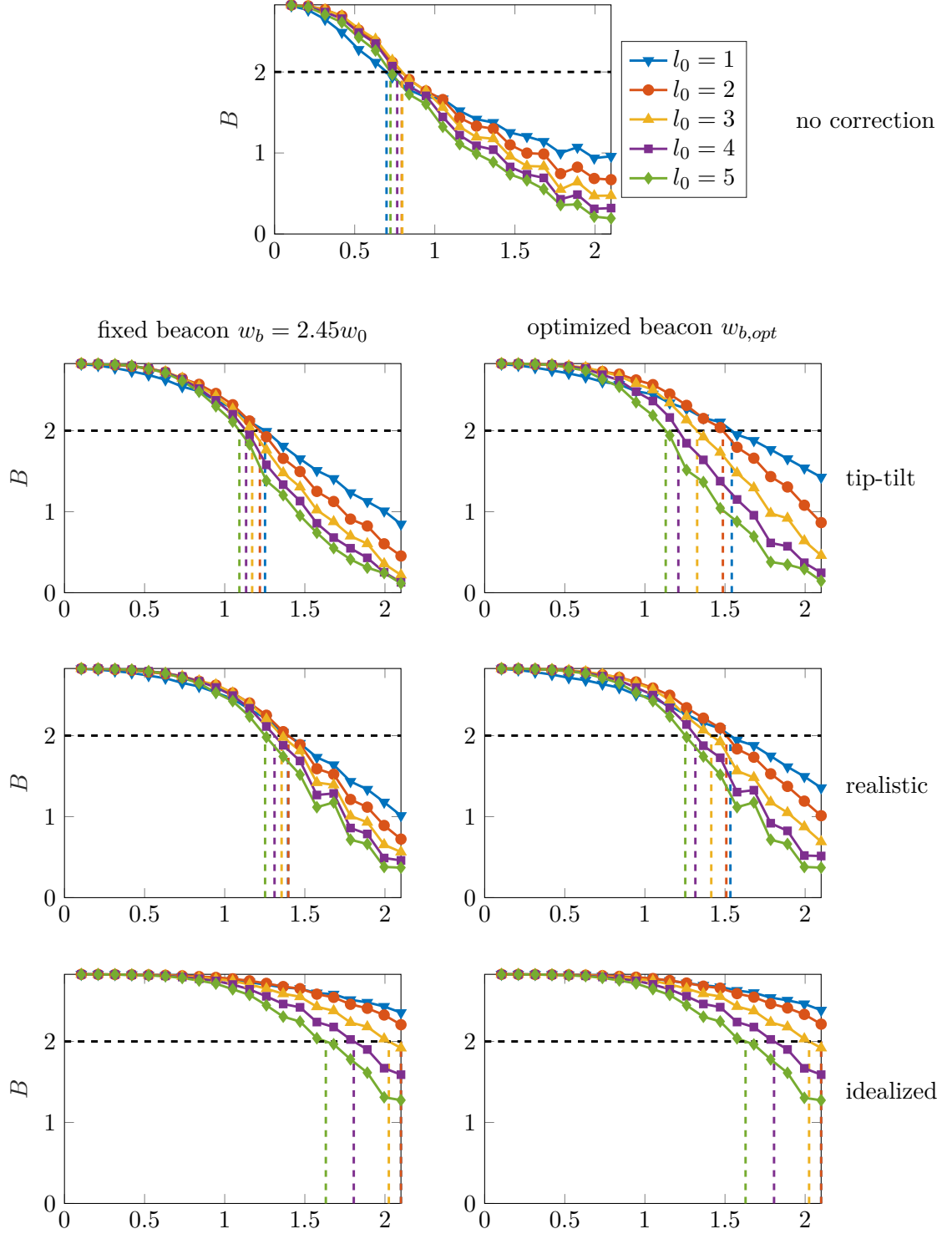
Figure 6.8: Improvement of the Bell parameter evolution achieved by the beacon beam waist optimization. On the top, the evolution without AO is shown. The colors encode different values of OAM l. The left and right column compare the Bell parameter before and after the optimization, respectively. In the second to fourth row, the tip-tilt, realistic and idealized AO results are shown. To highlight the transition at $B = 2$ above which a Bell inequality is violated, the dashed lines indicate the value of w_0/r_0 where the curves cross.

To summarize, this chapter has shown that the beacon beam waist has an effect on the compensation efficiency of the AO system. The quantities associated with the entanglement of the photons, the concurrence and the Bell parameter, can particularly profit from an optimization of the beam beam waist, while the trace and error rate also applicable to classical communication are less sensitive to it. Hence, quantum key distribution systems can benefit from the right choice of the beacon beam waist. Moreover, it could be shown that the optimum beacon beam waist depends on the AO system configuration, for tip-tilt compensation the value is in general lower than for the realistic AO system. The idealized AO system hardly depends on the beacon beam waist, as long as it is chosen larger than the OAM signal beam waist. Furthermore, it should be mentioned that in Figs. 6.7 and 6.8 the beacon beam waist is chosen individually for the OAM modes. In an experiment transmitting several OAM modes simultaneously, this may not be feasible because the beacon beam waist should only have one value. In that case, the beacon beam waist should be chosen depending on the particular choice of OAM modes to provide the overall best performance. Hence, a more detailed optimization may be required.

Chapter 7

Conclusion and outlook

High-dimensional systems have been a promising candidate to further improve quantum key distribution in terms of security and robustness to noise. One example of such high-dimensional systems are orbital angular momentum (OAM) photons which, however, face a great obstacle in their free-space transmission, namely atmospheric turbulence. Turbulence distorts the phase of photons, which is the defining property of OAM, and is thus detrimental to the communication protocol. In this thesis, it was demonstrated that adaptive optics can mitigate turbulence distortions for the application of quantum key distribution. With help of the developed simulation routine, the action of three adaptive optics systems is explored. The most simplistic tip-tilt system and the idealized system with maximum resolution serve as the lower and upper bound for the performance. A key element of the simulation routine is the model of an existing adaptive optics system developed for classical optical communication. By applying a phase correction based on measurements performed on a beacon, adaptive optics can reduce the crosstalk between different OAM modes. Security criteria for quantum key distribution protocols, in particular the quantum bit error rate and the violation of a Bell inequality, are used to verify that, with adaptive optics, the applicability of OAM can be extended to a stronger turbulence regime.

With this work it was demonstrated for the first time that adaptive optics bears great potential for OAM-based quantum key distribution. The application scenario is the transmission of one photon of an OAM-entangled two-qubit state through atmospheric turbulence. To provide the required control loop signals for an adaptive optics system, a Gaussian beacon co-propagates with the signal photons. Adaptive optics can indeed improve the crosstalk both between modes used to encode the information and

also to modes outside the encoding subspace. The entanglement which is lost through the crosstalk and subsequent projection to the encoding subspace can be recovered by applying adaptive optics to a certain degree. Because of the projection to a restricted number of modes, the trace of the final state's density matrix decreases with the turbulence strength. Adaptive optics can counter-act this effect which, in an experiment, would improve the signal-to-noise-ratio. Most importantly, adaptive optics can ensure that security tests of the quantum key distribution protocol are positive for two to three times stronger turbulence in terms of the Fried parameter. By that, adaptive optics can considerably extend the applicability of OAM-based quantum key distribution.

The Gaussian beacon plays an important role in the adaptive optics system since its measured wavefront determines the correction applied to the OAM photons. The different geometries of a Gaussian beacon and the OAM photons with a Laguerre-Gaussian mode profile were the motivation to optimize the beacon's beam waist in Chapter 6. The key finding is that the quantum-mechanical properties such as the entanglement measured by concurrence and the Bell parameter benefit most from this optimization. Consequently, the choice of the beacon beam waist can have an impact on the design of a quantum experiment with OAM and adaptive optics. Because the optimal beacon beam waist varies with the type of adaptive optics compensation and the involved OAM modes, one could include a similar optimization as performed in this thesis in the design of an experiment to achieve best performance.

For future work, the obvious and most urgent next step is the experimental implementation of a real-time AO system for OAM communication to go beyond the static systems known in the literature. The results of this thesis provide a strong motivation to implement such a system which could then be tested in a free-space link. Since adaptive optics is a well-developed technology with several commercial suppliers on the market, there is no technological obstacle that prevents the deployment of such a system. For a quantum key distribution application, care should be taken in the optical design to avoid that the classical beacon, which has a comparatively high intensity, enters the quantum signal path. Depending on the propagation geometry, it could be worthwile to include an additional pre-compensation adaptive optics system at the transmitter to further improve the OAM transmission.

In the context of future experiments with higher-dimensional OAM states, the results of this thesis can be useful, although the work focused on qubit systems. To date, free-space experiments have been performed either for qubits or hybrid OAM and polarization states because turbulence distortions and the associated crosstalk limited

the OAM transmission. As a result, the potential of OAM communication and the associated high dimensionality has not been fully exploited. A reduction of crosstalk as demonstrated in this thesis, however, suggest that with adaptive optics new free-space experiments involving higher-dimensional OAM states become possible. One example would be the transmission of higher-dimensional entanglement which can already be generated in the laboratory. Another possibility would be the transmission of several qubits distinguished by their OAM to generate several simultaneous quantum channels, similar to multiplexing in classical communication. In the long run, adaptive optics could become an enabling technology to allow for a commercialization of OAM-based both classical and quantum communication.

For OAM communication in quantum cryptography, this thesis has shown that adaptive optics can help overcome the limitations of state-of-the-art systems. The main result is that adaptive optics can recover OAM entanglement and allow for secure quantum communication when it would not be possible due to turbulence distortions. While some further optimizations of the adaptive optics configuration may be carried out in the near future, the next important step is the experimental demonstration of an adaptive optics system for OAM communication. Based on such results, the true potential of the infinite-dimensional state space of OAM can be reached in the future.

Bibliography

[1] R. Ursin et al., "Entanglement-based quantum communication over 144 km", Nature Phys. **3**, 481–486 (2007).

[2] S.-K. Liao et al., "Satellite-to-ground quantum key distribution", Nature **549**, 43–47 (2017).

[3] H. Bechmann-Pasquinucci and A. Peres, "Quantum cryptography with 3-state systems", Phys Rev Lett **85**, 3313–3316 (2000).

[4] M. Bourennane, A. Karlsson, and G. Björk, "Quantum key distribution using multilevel encoding", Phys Rev A **64**, 012306 (2001).

[5] D. Kaszlikowski, P. Gnaci ski, M. ukowski, W. Miklaszewski, and A. Zeilinger, "Violations of local realism by two entangled n-dimensional systems are stronger than for two qubits", Phys. Rev. Lett. **85**, 4418–4421 (2000).

[6] D. Collins, N. Gisin, N. Linden, S. Massar, and S. Popescu, "Bell inequalities for arbitrarily high-dimensional systems", Phys. Rev. Lett. **88**, 040404 (2002).

[7] J. Wang et al., "Terabit free-space data transmission employing orbital angular momentum multiplexing", Nat Photonics **6**, 488–496 (2012).

[8] M. Krenn, J. Handsteiner, M. Fink, R. Fickler, and A. Zeilinger, "Twisted photon entanglement through turbulent air across vienna", PNAS **112**, 14197–14201 (2015).

[9] A. Sit et al., "High-dimensional intracity quantum cryptography with structured photons", Optica **4**, 1006–1010 (2017).

[10] R. Tyson, *Principles of Adaptive Optics*, 3rd (CRC Press, Boca Raton, 2011).

[11] B. Rodenburg, M. Mirhosseini, M. Malik, O. S. Magaña-Loaiza, M. Yanakas, L. Maher, N. K. Steinhoff, G. A. Tyler, and R. W. Boyd, "Simulating thick atmospheric turbulence in the lab with application to orbital angular momentum communication", New J Phys **16**, 033020 (2014).

[12] Y. Ren et al., "Adaptive-optics-based simultaneous pre- and post-turbulence compensation of multiple orbital-angular-momentum beams in a bidirectional free-space optical link", Optica **1**, 376–382 (2014).

[13] N. Leonhard, R. Berlich, S. Minardi, A. Barth, S. Mauch, J. Mocci, M. Goy, M. Appelfelder, E. Beckert, and C. Reinlein, "Real-time adaptive optics testbed to investigate point-ahead angle in pre-compensation of earth-to-geo optical communication", Opt Express **24**, 13157–13172 (2016).

[14] C. Paterson, "Atmospheric turbulence and orbital angular momentum of single photons for optical communication", Phys Rev Lett **94**, 153901 (2005).

[15] B. J. Smith and M. G. Raymer, "Two-photon wave mechanics", Phys Rev A **74**, 062104 (2006).

[16] J. Poynting, "The wave motion of a revolving shaft, and a suggestion as to the angular momentum in a beam of circularly polarised light", Proceedings of the Royal Society of London A: Mathematical, Physical and Engineering Sciences **82**, 560–567 (1909).

[17] R. A. Beth, "Mechanical detection and measurement of the angular momentum of light", Phys Rev **50**, 115–125 (1936).

[18] L. Allen, M. W. Beijersbergen, R. J. C. Spreeuw, and J. P. Woerdman, "Orbital angular momentum of light and the transformation of Laguerre-Gaussian laser modes", Phys Rev A **45**, 8185–8189 (1992).

[19] G. Grynberg, A. Aspect, C. Fabre, and C. Cohen-Tannoudji, *Introduction to quantum optics: from the semi-classical approach to quantized light* (Cambridge University Press, 2010).

[20] L. Mandel and E. Wolf, *Optical coherence and quantum optics* (Cambridge University Press, 1995).

[21] D. L. Andrews and M. Babiker, eds., *The Angular Momentum of Light* (Cambridge University Press, 2012).

[22] J. D. Jackson, *Classical electrodynamics* (Wiley, 1998).

[23] P. Milonni and J. Eberly, *Laser physics* (Wiley, 2010).

[24] J. J. Sakurai, *Modern quantum mechanics*, edited by S. F. Tuan (Addison-Wesley Publishing, C., 1994).

[25] T. Knott, *Das Stern-Gerlach-Experiment, schematisch*, Wikimedia Commons, published under a BY-SA-Creative-Commons-Lizenz 3.0 in 2006. `https://de.wikipedia.org/wiki/Stern-Gerlach-Versuch#/media/File:Stern-Gerlach_Experiment_de.png`.

[26] M. Nielsen and I. Chuang, *Quantum computation and quantum information: 10th anniversary edition* (Cambridge University Press, 2010).

[27] W. K. Wootters, "Entanglement of formation of an arbitrary state of two qubits", Phys Rev Lett **80**, 2245–2248 (1998).

[28] N. Leonhard, G. Sorelli, V. N. Shatokhin, C. Reinlein, and A. Buchleitner, "Protecting the entanglement of twisted photons by adaptive optics", Phys Rev A **97**, 012321 (2018).

[29] N. Gisin and R. Thew, "Quantum communication", Nat Photonics **1**, 165–171 (2007).

[30] N. Gisin, G. Ribordy, W. Tittel, and H. Zbinden, "Quantum cryptography", Rev Mod Phys **74**, 145–195 (2002).

[31] C. E. Shannon, "Communication theory of secrecy systems", Bell System Technical Journal **28**, 656–715 (1949).

[32] C. H. Bennett and G. Brassard, "Quantum cryptography: public key distribution and coin tossing", in 1984 International Conference on Computers, Systems & Signal Processing, Bangalore, India (1984), pp. 175–179.

[33] A. K. Ekert, "Quantum cryptography based on bell's theorem", Phys Rev Lett **67**, 661–663 (1991).

[34] W. K. Wootters and W. H. Zurek, "A single quantum cannot be cloned", Nature **299**, 802– (1982).

[35] P. W. Shor and J. Preskill, "Simple proof of security of the BB84 quantum key distribution protocol", Phys Rev Lett **85**, 441–444 (2000).

[36] J. F. Clauser, M. A. Horne, A. Shimony, and R. A. Holt, "Proposed experiment to test local hidden-variable theories", Phys. Rev. Lett. **23**, 880–884 (1969).

[37] A. C. Dada, J. Leach, G. S. Buller, M. J. Padgett, and E. Andersson, "Experimental high-dimensional two-photon entanglement and violations of generalized bell inequalities", Nature Physics **7**, 677–680 (2011).

[38] A. E. Willner, Y. Ren, G. Xie, Y. Yan, L. Li, Z. Zhao, J. Wang, M. Tur, A. F. Molisch, and S. Ashrafi, "Recent advances in high-capacity free-space optical and radio-frequency communications using orbital angular momentum multiplexing", Philosophical Transactions of the Royal Society of London A: Mathematical, Physical and Engineering Sciences **375** (2017).

[39] S. Li, S. Chen, C. Gao, A. E. Willner, and J. Wang, "Atmospheric turbulence compensation in orbital angular momentum communications: advances and perspectives", Optics Communications **408**, Optical Communications Exploiting the Space Domain, 68–81 (2018).

[40] M. Erhard, R. Fickler, M. Krenn, and A. Zeilinger, "Twisted photons: new quantum perspectives in high dimensions", Light: Science & Applications **7**, 17146 (2018).

[41] G. Gibson, J. Courtial, M. Padgett, M. Vasnetsov, V. Pas'ko, S. Barnett, and S. Franke-Arnold, "Free-space information transfer using light beams carrying orbital angular momentum", Opt Express **12**, 5448–5456 (2004).

[42] S. Franke-Arnold, S. M. Barnett, E. Yao, J. Leach, J. Courtial, and M. Padgett, "Uncertainty principle for angular position and angular momentum", New J Phys **6**, 103 (2004).

[43] H. Huang et al., "100 tbit/s free-space data link enabled by three-dimensional multiplexing of orbital angular momentum, polarization, and wavelength", Opt. Lett. **39**, 197–200 (2014).

[44] Y. Ren et al., "Experimental characterization of a 400 Gbit/s orbital angular momentum multiplexed free-space optical link over 120 m", Opt. Lett. **41**, 622–625 (2016).

[45] M. P. J. Lavery, C. Peuntinger, K. Günthner, P. Banzer, D. Elser, R. W. Boyd, M. J. Padgett, C. Marquardt, and G. Leuchs, "Free-space propagation of high-dimensional structured optical fields in an urban environment", Science Advances **3**, e1700552 (2017).

[46] M. Krenn, R. Fickler, M. Fink, J. Handsteiner, M. Malik, T. Scheidl, R. Ursin, and A. Zeilinger, "Communication with spatially modulated light through turbulent air across vienna", New J Phys **16**, 113028 (2014).

[47] M. Krenn, J. Handsteiner, M. Fink, R. Fickler, R. Ursin, M. Malik, and A. Zeilinger, "Twisted light transmission over 143 km", PNAS **113**, 13648–13653 (2016).

[48] G. A. Tyler and R. W. Boyd, "Influence of atmospheric turbulence on the propagation of quantum states of light carrying orbital angular momentum", Opt. Lett. **34**, 142–144 (2009).

[49] J. A. Anguita, M. A. Neifeld, and B. V. Vasic, "Turbulence-induced channel crosstalk in an orbital angular momentum-multiplexed free-space optical link", Appl Opt **47**, 2414–2429 (2008).

[50] B. Rodenburg, M. P. J. Lavery, M. Malik, M. N. O'Sullivan, M. Mirhosseini, D. J. Robertson, M. Padgett, and R. W. Boyd, "Influence of atmospheric turbulence on states of light carrying orbital angular momentum", Opt. Lett. **37**, 3735–3737 (2012).

[51] M. Malik, M. O'Sullivan, B. Rodenburg, M. Mirhosseini, J. Leach, M. P. J. Lavery, M. J. Padgett, and R. W. Boyd, "Influence of atmospheric turbulence on optical communications using orbital angular momentum for encoding", Opt. Express **20**, 13195–13200 (2012).

[52] Y. Ren et al., "Adaptive optics compensation of multiple orbital angular momentum beams propagating through emulated atmospheric turbulence", Opt Lett **39**, 2845–2848 (2014).

[53] S. Li and J. Wang, "Compensation of a distorted n-fold orbital angular momentum multicasting link using adaptive optics", Opt. Lett. **41**, 1482–1485 (2016).

[54] S. Fu, S. Zhang, T. Wang, and C. Gao, "Pre-turbulence compensation of orbital angular momentum beams based on a probe and the gerchberg–saxton algorithm", Opt. Lett. **41**, 3185–3188 (2016).

[55] G. Xie et al., "Performance metrics and design considerations for a free-space optical orbital-angular-momentum-multiplexed communication link", Optica **2**, 357–365 (2015).

[56] L. Li et al., "Experimental demonstration of beaconless beam displacement tracking for an orbital angular momentum multiplexed free-space optical link", Opt Lett **43**, 2392–2395 (2018).

[57] A. Mair, A. Vaziri, G. Weihs, and A. Zeilinger, "Entanglement of the orbital angular momentum states of photons", Nature **412**, 313–316 (2001).

[58] R. Fickler, R. Lapkiewicz, W. N. Plick, M. Krenn, C. Schaeff, S. Ramelow, and A. Zeilinger, "Quantum entanglement of high angular momenta", Science **338**, 640–643 (2012).

[59] S. Gröblacher, T. Jennewein, A. Vaziri, G. Weihs, and A. Zeilinger, "Experimental quantum cryptography with qutrits", New J Phys **8**, 75 (2006).

[60] N. Leonhard, V. N. Shatokhin, and A. Buchleitner, "Universal entanglement decay of photonic-orbital-angular-momentum qubit states in atmospheric turbulence", Phys Rev A **91**, 012345 (2015).

[61] A. H. Ibrahim, F. S. Roux, and T. Konrad, "Parameter dependence in the atmospheric decoherence of modally entangled photon pairs", Phys. Rev. A **90**, 052115 (2014).

[62] A. Hamadou Ibrahim, F. S. Roux, M. McLaren, T. Konrad, and A. Forbes, "Orbital-angular-momentum entanglement in turbulence", Phys Rev A **88**, 012312 (2013).

[63] B.-J. Pors, C. H. Monken, E. R. Eliel, and J. P. Woerdman, "Transport of orbital-angular-momentum entanglement through a turbulent atmosphere", Opt Express **19**, 6671–6683 (2011).

[64] G. Vallone, V. D'Ambrosio, A. Sponselli, S. Slussarenko, L. Marrucci, F. Sciarrino, and P. Villoresi, "Free-space quantum key distribution by rotation-invariant twisted photons", Phys Rev Lett **113**, 060503 (2014).

[65] L. C. Andrews and R. L. Phillips, *Laser beam propagation through random media*, Second (SPIE Press, Bellingham, 2005).

[66] V. Tatarski, *Wave propagation in a turbulent medium*, Dover Books on Physics, Reprint of the 1967 Dover edition. The English translation was originally published by McGraw-Hill in 1961. (Dover Publications, 2016).

[67] D. L. Fried, "Optical resolution through a randomly inhomogeneous medium for very long and very short exposures", J Opt Soc Am **56**, 1372–1379 (1966).

[68] J. W. Goodman, *Introduction to fourier optics* (McGraw-Hill, 1996).

[69] J. D. Schmidt, *Numerical Simulation of Optical Wave Propagation with examples in MATLAB* (SPIE Press, Bellingham, 2010).

[70] R. G. Lane, A. Glindemann, and J. C. Dainty, "Simulation of a kolmogorov phase screen", Waves in Random Media **2**, 209–224 (1992).

[71] B. M. Welsh, "Fourier-series-based atmospheric phase screen generator for simulating anisoplanatic geometries and temporal evolution", Proc. SPIE **3125**, 327–338 (1997).

[72] R. J. Noll, "Zernike polynomials and atmospheric turbulence", J Opt Soc Am **66**, 207–211 (1976).

[73] M. Krenn, M. Huber, R. Fickler, R. Lapkiewicz, S. Ramelow, and A. Zeilinger, "Generation and confirmation of a (100 by 100)-dimensional entangled quantum system", PNAS **111**, 6243–6247 (2014).

[74] S. Magnitskiy, D. Frolovtsev, V. Firsov, P. Gostev, I. Protsenko, and M. Saygin, "A spdc-based source of entangled photons and its characterization", J. Russian Laser Res. **36**, 618–629 (2015).

[75] P. Trojek and H. Weinfurter, "Collinear source of polarization-entangled photon pairs at nondegenerate wavelengths", Applied Physics Letters **92**, 211103 (2008).

[76] X. Li, P. L. Voss, J. E. Sharping, and P. Kumar, "Optical-fiber source of polarization-entangled photons in the 1550 nm telecom band", Phys. Rev. Lett. **94**, 053601 (2005).

[77] G. Sorelli, N. Leonhard, V. N. Shatokhin, C. Reinlein, and A. Buchleitner, "Entanglement protection of high-dimensional states by adaptive optics", New Journal of Physics **21**, 023003 (2019).

[78] F. E. S. Vetelino and R. J. Morgan, "Propagation of higher-order annular laguerre-gauss beams in atmospheric turbulence", Proc. SPIE **7685**, 768503 (2010).

[79] V. P. Lukin, P. A. Konyaev, and V. A. Sennikov, "Beam spreading of vortex beams propagating in turbulent atmosphere", Appl. Opt. **51**, C84–C87 (2012).

[80] A. Brady, C. Rössler, N. Leonhard, M. Gier, R. Eberhardt, and C. Reinlein, "Validation of point ahead angle on pre-compensation in a 1km free-space propagation experiment", in preparation.

[81] C. Shannon, "Communication in the presence of noise", Proceedings of the IRE **37**, 10–21 (1949).

[82] F. Chassat, "Theoretical evaluation of the isoplanatic patch of an adaptive optics system working through the atmospheric turbulence", J Opt **20**, 13 (1989).

[83] C. Roessler, "Simulationen zur Vorkompensation atmosphärischer Turbulenzen für Boden-Satelliten-Kommunikation", Master thesis (Friedrich-Schiller-Universität Jena, July 31, 2018).

[84] R. Berlich, T. Kopf, A. Brady, N. Leonhard, A. Kamm, and C. Reinlein, "Transportable system for in-field testing of adaptive optical pre-compensation for optical feeder links", Proc. SPIE International Conference on Space Optics (ICSO) 2016 **10562**, 105625V (2017).

[85] A. Brady, R. Berlich, N. Leonhard, T. Kopf, P. Böttner, R. Eberhardt, and C. Reinlein, "Experimental validation of phase-only pre-compensation over 494 m free-space propagation", Opt Lett **42**, 2679–2682 (2017).

[86] A. Talmi and E. N. Ribak, "Wavefront reconstruction from its gradients", J. Opt. Soc. Am. A **23**, 288–297 (2006).

[87] J. D'Errico, *Surface fitting using gridfit, version 2.0*, (May 23, 2006) `https://de.mathworks.com/matlabcentral/fileexchange/8998-surface-fitting-using-gridfit?s%5C_cid=ME%5C_prod%5C_FX`.

[88] M. C. Roggemann and C. L. Matson, "Power spectrum and Fourier phase spectrum estimation by using fully and partially compensating adaptive optics and bispectrum postprocessing", J. Opt. Soc. Am. A **9**, 1525–1535 (1992).

[89] B. L. Ellerbroek, "Linear systems modeling of adaptive optics in the spatial-frequency domain", J. Opt. Soc. Am. A **22**, 310–322 (2005).

[90] L. Jolissaint, J.-P. Véran, and R. Conan, "Analytical modeling of adaptive optics: foundations of the phase spatial power spectrum approach", J. Opt. Soc. Am. A **23**, 382–394 (2006).

[91] L. Jolissaint, "Synthetic modeling of astronomical closed loop adaptive optics", Journal of the European Optical Society - Rapid publications **5** (2010).

[92] T. Pertermann, J. Hartung, M. Beier, M. Trost, S. Schröder, S. Risse, R. Eberhardt, A. Tünnermann, and H. Gross, "Angular resolved power spectral density analysis for improving mirror manufacturing", Appl. Opt. **57**, 8692–8698 (2018).

[93] F. S. Roux, "The Lindblad equation for the decay of entanglement due to atmospheric scintillation", J Phys A: Math Theor **47**, 195302 (2014).

[94] V. Vedral, M. B. Plenio, M. A. Rippin, and P. L. Knight, "Quantifying entanglement", Phys. Rev. Lett. **78**, 2275–2279 (1997).

[95] G. Vidal, "Entanglement monotones", Journal of Modern Optics **47**, 355–376 (2000).

[96] F. S. Roux, "Infinitesimal-propagation equation for decoherence of an orbital-angular-momentum-entangled biphoton state in atmospheric turbulence", Phys Rev A **83**, 053822 (2011).

[97] C. Gopaul and R. Andrews, "The effect of atmospheric turbulence on entangled orbital angular momentum states", New J Phys **9**, 94 (2007).

[98] A. Montmerle Bonnefois et al., "Adaptive optics pre-compensation for geo feeder links: the feedelio experiment", in International Conference on Space Optics, 9-12 October 2018, Chania, Greece (2018).

[99] R. Saathof et al., "Adaptive optics pre-correction for optical feeder links - breadboard performance", in International Conference on Space Optics, 9-12 October 2018, Chania, Greece (2018).

[100] Y. Ren et al., "Turbulence compensation of an orbital angular momentum and polarization-multiplexed link using a data-carrying beacon on a separate wavelength", Opt. Lett. **40**, 2249–2252 (2015).

[101] M. J. Padgett, F. M. Miatto, M. P. J. Lavery, A. Zeilinger, and R. W. Boyd, "Divergence of an orbital-angular-momentum-carrying beam upon propagation", New Journal of Physics **17**, 023011 (2015).

[102] I. Hughes and T. Hase, *Measurements and their uncertainties: a practical guide to modern error analysis* (OUP Oxford, 2010).

[103] E. W. Weisstein, *Bessel function of the first kind, from mathworld–a wolfram web resource*, (Feb. 8, 2019) `http://mathworld.wolfram.com/BesselFunctionoftheFirstKind.html`.

[104] M. Abramowitz and I. Stegun, *Handbook of mathematical functions: with formulas, graphs, and mathematical tables*, Applied mathematics series (Dover Publications, 1965).

Appendix

A Derivation of Laguerre-Gauss mode size in Fourier space

In this section, the Fourier transform of Laguerre-Gauss modes is calculate which is used in Sec. 3.3 to determine the sampling of the modes. For convenience, the mode function of Laguerre-Gauss modes is repeated here, see Eq. (2.8)

$$u_{p,l}(r, \theta, z) = N_{p,l} \left(\frac{\sqrt{2}r}{w(z)} \right)^{|l|} L_p^{|l|} \left(\frac{2r^2}{w^2(z)} \right) e^{-\frac{r^2}{w(z)^2}} e^{-\frac{ikr^2 z}{2(z^2+z_R^2)}} e^{i(2p+|l|+1)\Phi(z)} e^{il\theta} . \tag{1}$$

Since the radial index is not investigated in this thesis, i.e. $p = 0$, the mode function is simplified thanks to $L_0^l(x) = 1$. In addition, the calculation is performed at $z = 0$

$$u_{0,l}(r, \theta, z = 0) = N_{0,l} \left(\frac{\sqrt{2}r}{w_0} \right)^{|l|} e^{-\frac{r^2}{w_0}} e^{il\theta} . \tag{2}$$

Now, the two-dimensional Fourier transform of this mode function $\tilde{u}_{0,l}$ can be calculated

$$\tilde{u}_{0,l}(\mathbf{k}) = \iint u_{0,l}(\mathbf{r}) e^{i\mathbf{k}\cdot\mathbf{r}} d\mathbf{r} , \tag{3}$$

where $\mathbf{r}$ is the vector in the transverse plane. The calculation is performed in polar coordinates, in real space (r, θ) and in reciprocal space (k, ϕ). The scalar product in Eq. (3), can be expressed as $\mathbf{k} \cdot \mathbf{r} = kr \cos(\theta - \phi)$

$$\tilde{u}_{0,l}(k, \phi) = N_{0,l} e^{il\phi} \int_0^\infty \left(\frac{\sqrt{2}r}{w_0} \right)^{|l|} e^{-\frac{r^2}{w_0}} \int_0^{2\pi} e^{il(\theta-\phi)} e^{ikr\cos(\theta-\phi)} d\theta \, r dr . \tag{4}$$

The angular integral returns the lth Bessel function of first kind [103]

$$J_l(x) = \frac{1}{2\pi i^n} \int_0^{2\pi} \exp(ix \cos \phi' + il\phi') d\phi' . \tag{5}$$

Accordingly, one obtains

$$\tilde{u}_{0,l}(k,\phi) = N_{0,l}e^{il\phi}2\pi i^l \int_0^\infty \left(\frac{\sqrt{2}r}{w_0}\right)^{|l|} e^{-\frac{r^2}{w_0}} J_l(kr)\, r\mathrm{d}r\,. \tag{6}$$

Next, the solution of the radial integral is known [104, Eq. 11.4.29]

$$\int_0^\infty e^{-a^2t^2} t^{\nu+1} J_\nu(bt)\mathrm{d}t = \frac{b^\nu}{(2a^2)^{\nu+1}} e^{-\frac{b^2}{4a^2}} \quad \text{if } Re(\nu) > -1, Re(a^2) > 0\,. \tag{7}$$

The final result has thus the same form as the initial Laguerre-Gauss mode

$$\tilde{u}_{0,l}(k,\phi) = \tilde{N}_{0,l}e^{il\phi}k^{|l|}e^{-k^2w_0^2/4}\,, \tag{8}$$

with a beam waist in reciprocal space of $\tilde{w}_0 = \frac{2}{w_0}$ and a new normalization constant $\tilde{N}_{0,l}$. Completely analogous to the calculation of the root-mean-square beam radius in real space, one can find it in reciprocal space

$$\langle k^2 \rangle = \frac{2}{w_0}\sqrt{|l|+1}\,. \tag{9}$$

With the result from Eq. (9), the sampling criterion for the Laguerre-Gauss modes can be derived leading to Eq. (3.39).

B   Optical transfer function for different adaptive optics models

In typical AO design studies, the optical transfer function is obtained by a product of analytical estimates of the individual AO subsystems. The quantity of interest, the point spread function, is then determined by an inverse Fourier transform of the optical transfer function. In this thesis, an end-to-end AO simulation is performed such that the point-spread function can be immediately computed without the optical transfer function. For completeness, this section discusses the results obtained for the optical transfer function of the different AO correction schemes. The optical transfer function can be interpreted as a measure how well an optical system transmits certain frequency components. For diffraction-limited systems, the optical transfer function decreases from its initial value of 1 as the spatial frequency increases and reaches a value of 0 at the cut-off frequency $f_0 = D/(\lambda f)$ determined by the telescope aperture. Figure B.1 plots the absolute value of the optical transfer function which is also known as the modulation transfer function. The turbulence strength was set to $D/r_0 = 10$. The
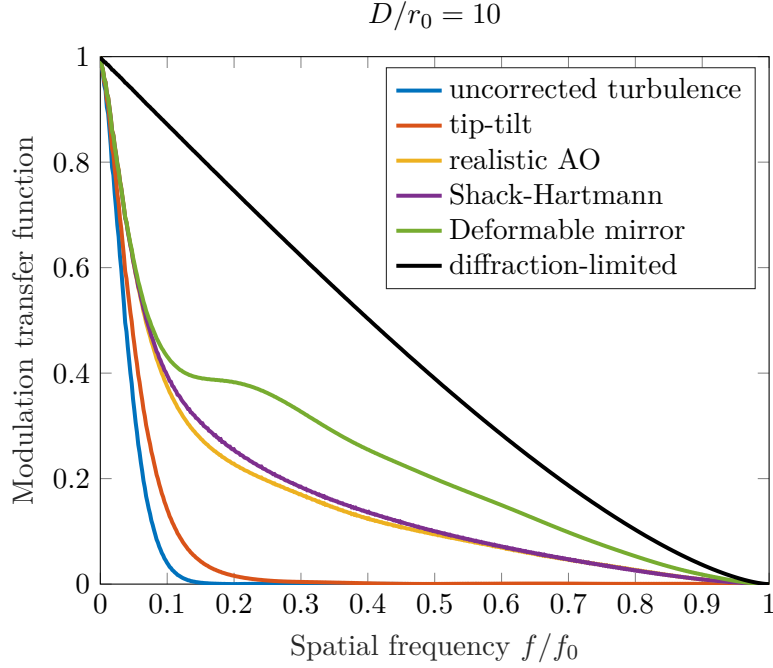
$$D/r_0 = 10$$

Figure B.1: Modulation transfer function for different degrees of correction for $D/r_0 = 10$. The curve without correction decays fastest while different degrees of AO correction can increase the optical transfer function. With the deformable mirror scheme, the evolution is closest to the diffraction-limited case.

diffraction-limited black curve decays from 1 at $f = 0$ to 0 at $f = f_0$ as expected. The blue curve shows that the turbulence-distorted optical transfer function decays fastest and high frequencies are strongly suppressed. The tip-tilt correction in the red curve can achieve a small increase. The realistic AO curve shown in yellow lies between the turbulence-distorted and diffraction-limited curves. It transmits also the higher frequencies but not as well as in the diffraction-limited case. The green curve showing only the deformable mirror contribution performs best. One can see a small plateau in the frequency range from $0.12f_0$ to $0.2f_0$. This behavior is in agreement with the better performance also for the point-spread function. However, it may be a bit surprising that the deformable mirror with only 40 actuators should have a better performance than the Shack-Hartmann sensor with 196 subapertures. This impression is further supported when considering the actuator shapes compared to the Shack-Hartmann lenslets shown in Fig. 4.4. The analysis of the power spectral density performed in Sec. 4.5 indicates that mostly the better performance at low frequencies causes this effect. Finally, it can be noted that the realistic AO has a similar evolution as the Shack-Hartmann sensor.

C   Trace and quantum bit error rate after beacon optimization

The following figures compare the trace, Fig. C.1, and the crosstalk rate R, Fig. C.2, before the optimization of the beacon diameter as described in Ch. 6 in the left column and after the optimization in the right. The topmost subplot gives the evolution without AO correction and is thus independent of the beacon beam waist. The second to fourth column give the results with tip-tilt, realistic and idealized AO, respectively. In contrast to the concurrence and Bell inequality violation, the trace and the crosstalk rate do not improve noticeably and are therefore only shown in this appendix for completeness.
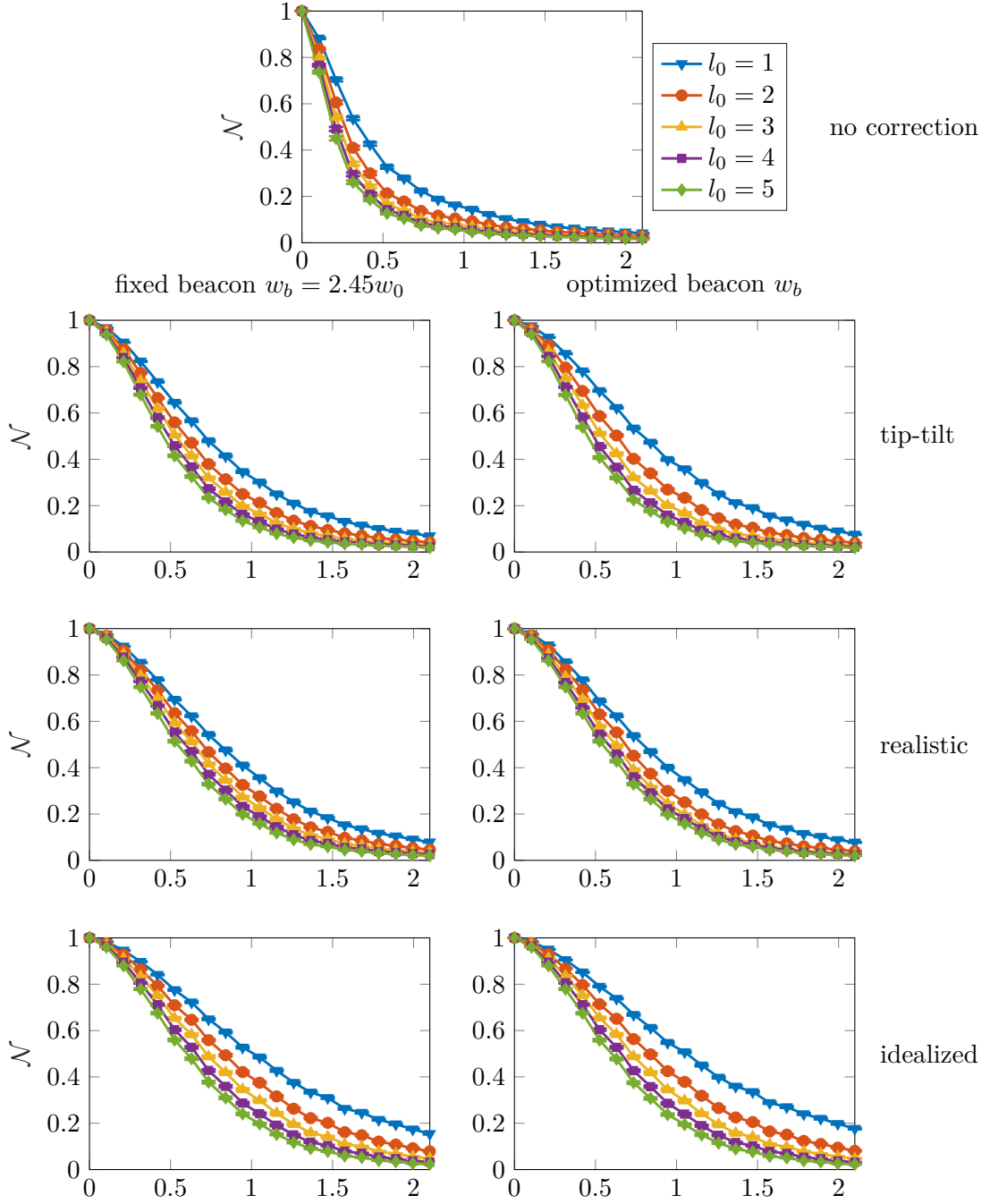
Figure C.1: Evolution of the trace as a function of the turbulence strength w_0/r_0: comparison before (left column) and after (right column) the beacon optimization described in Ch. 6. The different rows correspond to different degrees of AO correction as denoted by the label next to the plots. There is no significant improvement by the optimization for the trace, in contrast to the concurrence and Bell parameter shown in Figs. 6.7 and 6.8
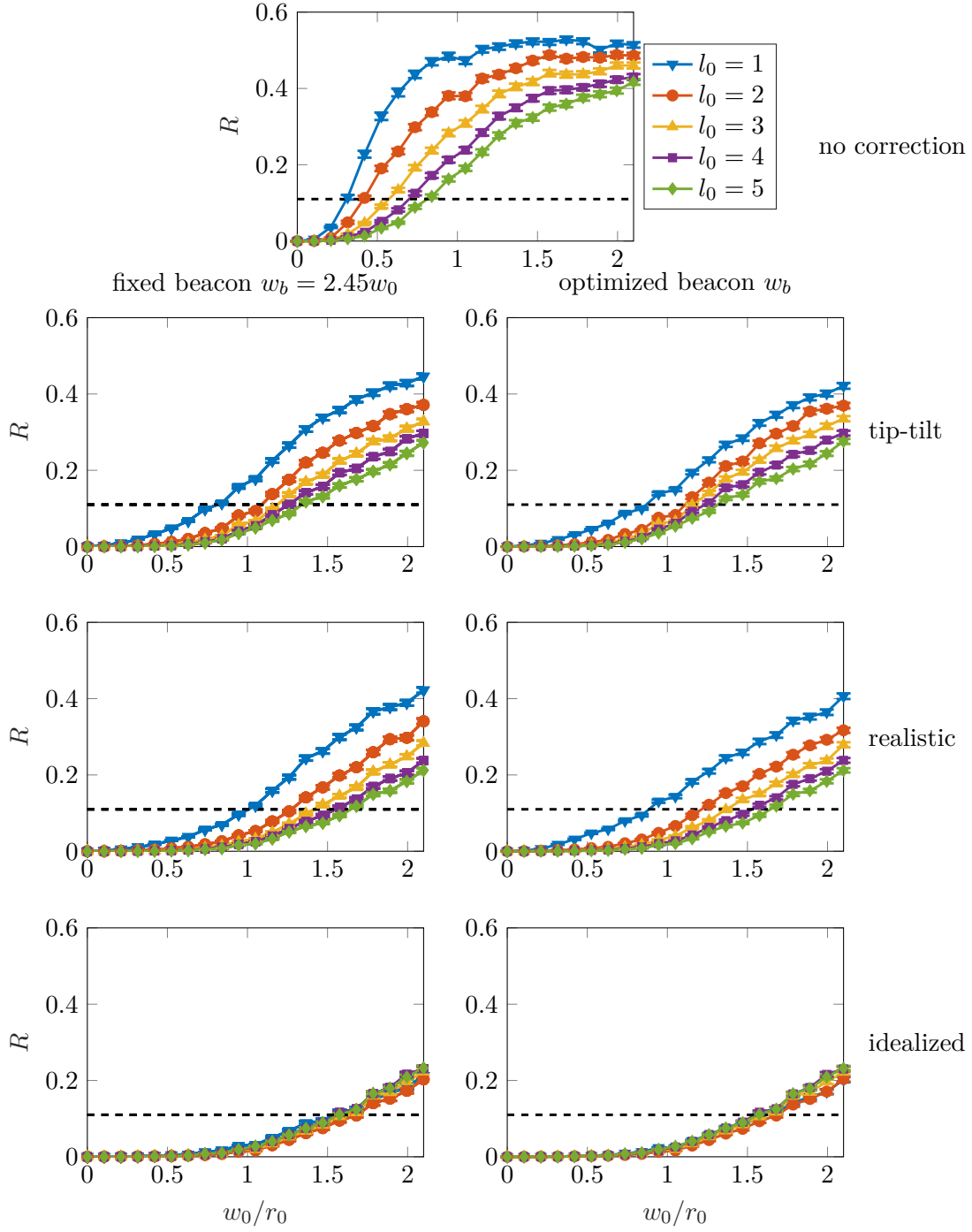
Figure C.2: Crosstalk rate for different turbulence strengths w_0/r_0 and varying AO compensation encoded by the rows. The left column depicts results before the beacon optimization and the right column after the optimization. The beacon optimization has almost no effect on the crosstalk rate.

Zusammenfassung

Mit der fortschreitenden Entwicklung von Quantencomputern werden neue Verschlüsselungsmethoden notwendig, die auch in Zukunft eine abhörsichere Übertragung von Nachrichten gewährleisten. Eine solche Methode repräsentiert der sogenannte Quantenschlüsselaustausch, dessen Sicherheit auf grundlegenden physikalischen Prinzipien der Quantenmechanik beruht und mit Hilfe von Messungen verifiziert werden kann. Die Anwendbarkeit des Quantenschlüsselaustauschs wurde bereits in vielen Experimenten demonstriert. Kürzlich wurde sogar ein Quantenschlüssel zwischen zwei entfernten Bodenstationen mit Hilfe einer Photonenquelle auf einem Satelliten erzeugt. Mit Hilfe von höherdimensional Zuständen wie beispielsweise Bahndrehimpulsphotonen könnten die Sicherheit und die Beständigkeit gegen Rauschen weiter erhöht werden. Der Bahndrehimpuls entsteht durch die besonderen Phasenfronten dieser Photonen, die aus ineinander verschlungenen Schraubenbahnen bestehen, und eröffnet einen theoretisch abzählbar unendlichen Zustandsraum. Eine starke Limitierung der Anwendbarkeit für Freistrahlexperimente stellen jedoch atmosphärische Turbulenzen dar, da sie Phasenstörungen erzeugen. Durch die Enkodierung der Information in den Bahndrehimpuls und damit der Phase der Photonen hat Turbulenz einen besonders starken Einfluss auf die Kommunikation mit Bahndrehimpulsphotonen. Zur Korrektur solcher Phasenstörungen wurde eine Technologie in der Astronomie entwickelt – die adaptive Optik. Während adaptive Optik im Zusammenhang mit klassischer Kommunikation mit Bahndrehimpuls bereits untersucht wurde, wird adaptive Optik in der vorliegenden Dissertation erstmals für Quantenkommunikation mit Bahndrehimpulsphotonen untersucht.

Im Rahmen der Promotion wurde eine Simulationsroutine entwickelt, mit der die Ausbreitung von Bahndrehimpulsphotonen durch atmosphärische Turbulenz sowie die anschließende Korrektur durch ein adaptiv-optisches System beschrieben werden kann. Die bereits existierende formelle Beschreibung des Photonenzustands in atmosphäri-

scher Turbulenz wurde durch die Wirkung der adaptiven Optik ergänzt. Als Szenario wurde die Übertragung eines Photons aus einem verschränkten Zwei-Qubit-Zustand untersucht. Das zentrale Ergebnis der Arbeit ist die Erkenntnis, dass adaptive Optik die Freistrahlübertragung für den Bahndrehimpuls-gestützen Quantenschlüsselaustausch auf vielfache Weise verbessern kann. Mit Hilfe von adaptiver Optik kann die Verschränkung und die Spur der Dichtematrix deutlich erhöht werden. Als Sicherheitskriterien für die Quantenschlüsselübertragung wurden die Quantenfehlerrate und die Verletzung von Bell-Ungleichungen ausgewählt. Dank adaptiver Optik konnte so eine sichere Übertragungen in doppelt bis dreimal so starker Turbulenz gemessen am Fried-Parameter nachgewiesen werden. Damit die adaptive Optik zwischen der Phasenstörung und der Information in der Phase der Photonen unterscheiden kann, wird ein klassicher Laserstrahl mit bekanntem Phasenprofil zum Messen der turbulenten Störungen benutzt. Aufgrund der unterschiedlichen Strahlgeometrien von Hilfsstrahl und Bahndrehimpulsphotonen wurde der Einfluss des Strahlradius dieses Hilfstrahls auf die Kompensationseffizienz untersucht. In Abhängigkeit vom Bahndrehimpuls der Photonen und der Art der adaptiv-optischen Korrektur konnte so ein optimaler Strahlradius gefunden werden. Es wurde weiterhin gezeigt, dass insbesondere die für den Quantenschlüsselaustausch wichtigen Gütekriterien von einer solchen Optimierung profitieren können.

Die Ergebnisse dieser Arbeit zeigen das große Potential von adaptiver Optik für Bahndrehimpuls-basierten Quantenschlüsselaustausch auf. Durch die Reduktion des Übersprechens zwischen den Bahndrehimpuls-Zuständen mit Hilfe von adaptiver Optik könnten neuartige Experimente erst ermöglicht werden. Die präsentierten theoretischen Ergebnisse setzen deshalb neue Impulse für die zukünfige experimentelle Umsetzung und Rahmenbedingungen von adaptiver Optik für Quantenschlüsselaustausch mit Bahndrehimpulsphotonen.

List of own publications

[1] N. Leonhard, G. Sorelli, V. N. Shatokhin, C. Reinlein, and A. Buchleitner, "Protecting the entanglement of twisted photons by adaptive optics", Phys. Rev. A **97**, 012321 (2018).

[2] N. Leonhard, R. Berlich, S. Minardi, A. Barth, S. Mauch, J. Mocci, M. Goy, M. Appelfelder, E. Beckert, and C. Reinlein, "Real-time adaptive optics testbed to investigate point-ahead angle in pre-compensation of Earth-to-GEO optical communication", Opt. Express **24** (12), 13157–13172 (2016).

[3] N. Leonhard, V. N. Shatokhin, and A. Buchleitner, "Universal entanglement decay of photonic-orbital-angular-momentum qubit states in atmospheric turbulence", Phys. Rev. A **91**,012345 (2015).

[4] G. Sorelli, N. Leonhard, V. N. Shatokhin, C. Reinlein, and A. Buchleitner, "Entanglement protection of high-dimensional states by adaptive optics", New Journal of Physics **21** (2), 023003 (2019).

[5] A. Brady, R. Berlich, N. Leonhard, T. Kopf, P. Böttner, R. Eberhardt, and C. Reinlein, "Experimental validation of phase-only pre-compensation over 494 m free-space propagation", Opt. Lett. **42** (14), 2679–2682 (2017).

[6] C. Reinlein, C. Damm, N. Lange, A. Kamm, M. Mohaupt, A. Brady, M. Goy, N. Leonhard, R. Eberhardt, U. Zeitner, and A. Tünnermann, "Temporally-stable active precision mount for large optics", Opt. Express **24** (12), 13527–13541 (2016).

Conference contributions

- N. Leonhard, R. Berlich, S. Minardi, A. Barth, C. Reinlein, "Adaptive optics testbed for pre- and post-compensation of Earth-to-GEO optical communication – downlink results", International Conference on Space Optics (ICSO), Biarritz, France (2016).

- N. Leonhard, C. Reinlein, "Adaptive optics system design for optical communication with higher- order laser modes", Deutsche Physikerinnentagung, Hamburg, Germany (2016).

- N. Leonhard, V. Shatokhin, A.Buchleitner, "Universal entanglement decay of photonic orbital angular momentum qubit states in atmospheric turbulence", International Conference on Quantum Physics of Nature (QuPoN), Vienna, Austria, *Poster* (2015).

- N. Leonhard, V. Shatokhin, A.Buchleitner "Propagation of Orbital Angular Momentum Photons through Atmospheric Turbulence", Frühjahrstagung der Deutschen Physikalischen Gesellschaft, Berlin, Germany (2014).

- N. Leonhard, V. Shatokhin, A.Buchleitner "Entanglement evolution of two entangled OAM photons under the effect of atmospheric turbulence", Frühjahrstagung der Deutschen Physikalischen Gesellschaft, Hannover, Germany (2013).

- N. Leonhard, V. Shatokhin, A.Buchleitner "Entanglement evolution of two entangled OAM photons under the effect of atmospheric turbulence", Conference on Extreme Atomic Systems, Riezlern, Austria (2013).

Acknowledgements

Finally, I would like to take the opportunity to thank a number of great people who have supported me during this thesis. First, I would like to thank my supervisor Herbert Gross for his constant support and encouragement. Each of our meetings has given new impulses to my work. By asking the right questions, he helped me resolve issues in my research while at the same time keeping the big picture in mind.

Next, I would like to thank Andreas Tünnermann for giving me the opportunity to perform my research at Fraunhofer IOF. I am also grateful to Ramona Eberhardt for her guidance and encouragement. A big thanks goes to Claudia Reinlein for her support throughout the past few years. It has been a pleasure working together. The same holds for my colleagues in the group of Active and Adaptive Optics, Teresa Kopf, Aoife Brady, Matthias Goy and Paul Böttner. Because of the great team spirit even working outside in freezing temperatures on a measurement campaign can be fun. Furthermore, I would like to thank Andreas Buchleitner, Vyacheslav Shatokhin and Giacomo Sorelli at University of Freiburg for the great cooperation.

I cannot thank my family enough for their love and support. My parents and my brother always have my back and I could not be happier to have them in my life. Finishing this thesis would not have been possible without the continuous love and support by my husband Markus. I am deeply grateful for this amazing relationship and all that we have accomplished in the past few years.

Ehrenwörtliche Erklärung

Ich erkläre hiermit ehrenwörtlich, dass ich die vorliegende Arbeit selbständig, ohne unzulässige Hilfe Dritter und ohne Benutzung anderer als der angegebenen Hilfsmittel und Literatur angefertigt habe. Die aus anderen Quellen direkt oder indirekt übernommenen Daten und Konzepte sind unter Angabe der Quelle gekennzeichnet.

Bei der Auswahl und Auswertung folgenden Materials haben mir die nachstehend aufgeführten Personen in der jeweils beschriebenen Weise entgeltlich/unentgeltlich geholfen:

- Die Formel sowie die Matlab-Funktion zur Berechnung der Concurrence und ihres Fehlers wurde von Giacomo Sorelli, Albert-Ludwigs-Universität Freiburg, unentgeltlich bereitgestellt.

Weitere Personen waren an der inhaltlich-materiellen Erstellung der vorliegenden Arbeit nicht beteiligt. Insbesondere habe ich hierfür nicht die entgeltliche Hilfe von Vermittlungs- bzw. Beratungsdiensten (Promotionsberater oder andere Personen) in Anspruch genommen. Niemand hat von mir unmittelbar oder mittelbar geldwerte Leistungen für Arbeiten erhalten, die im Zusammenhang mit dem Inhalt der vorgelegten Dissertation stehen.

Die Arbeit wurde bisher weder im In- noch im Ausland in gleicher oder ähnlicher Form einer anderen Prüfungsbehörde vorgelegt.

Die geltende Promotionsordnung der Physikalisch-Astronomischen Fakultät ist mir bekannt.

Ich versichere ehrenwörtlich, dass ich nach bestem Wissen die reine Wahrheit gesagt und nichts verschwiegen habe.

Jena, den 28.03.2019

Nina Leonhard